UNIVERSITY OF SOUTHAMPTON

FACULTY OF ENGINEERING, SCIENCE AND MATHEMATICS

Optoelectronics Research Centre

Development of Non-Linear Waveguide Devices for Optical Signal Processing

by

Costantino Corbari

Thesis submitted for the degree of Doctor of Philosophy

June 2005

UNIVERSITY OF SOUTHAMPTON

ABSTRACT

FACULTY OF ENGINEERING, SCIENCE AND MATHEMATICS
OPTOELECTRONICS RESEARCH CENTRE

Doctor of Philosophy

Development of Non-Linear Waveguide Devices for Optical Signal Processing

by Costantino Corbari

Reported in this thesis are advances in glass poling, a technique which produces second-order optical nonlinearity in glass. Poling of glass has drawn much attention because frequency conversion and electro-optic modulation, operations which are typically restricted to crystals, becomes feasible in glass fibres and waveguides which are widely spread media in photonics thanks to their excellent optical properties and mature manufacturing technology. Poled silica glass, despite showing about 10 times lower second-order nonlinearity than nonlinear crystals, can be competitive with them because longer interaction lengths are possible in glass fibres, owing to the lower chromatic dispersion.

In this thesis fundamental research about poling techniques, glass composition and characterization methods has been carried out in order to investigate possibilities for enhancing the second-order nonlinearity ($\chi^{(2)}$) induced by poling. A new poling method has been discovered whereby second-order nonlinearity was produced in undoped silica glass by two-photon absorption of femtosecond UV pulses in the presence of an applied static electric field. Silica pre-treatment by exposure to IR-femtosecond pulses, which are believed to introduce non-bridging oxygen hole centre defects in the glass, was also proven to enhance the induced second-order nonlinearity. From the point of view of the characterization of bulk poled glass, a non-destructive technique has been developed which enables accurate determination of the $\chi^{(2)}$ by overcoming the limitations of the Maker's fringe technique. The issue of the stability of the second-order nonlinearity in poled glass, which is fundamental for the development of devices, has been addressed in a variety of glass compositions: poled fused silica glass was found to be stable for over 30 years but a much longer stability was shown for a poled alkali free glass.

In parallel to the aforementioned investigations, technologies for the fabrication of $\chi^{(2)}$-gratings for quasi-phase matching in optical fibres have been developed. The continuous UV-erasure technique, introduced in this thesis, is compatible with the fabrication of 1 meter long $\chi^{(2)}$-gratings in fibres. This technology led to the first demonstration of an all-fibre frequency doubler of a fibre laser. Milliwatts of red light in the fundamental mode were produced by frequency doubling in a quasi-phase matched periodically poled silica fibre which was directly spliced to the output of the laser source. Efficiency up to 2.5% has been demonstrated in 11.5 cm long device with only about 100 W of pump power, which means that 50% conversion efficiency is expected for a 2 kW input power.

Contents

List of Figures

List of Tables

Nomenclature

Abbreviations:

AOM	Acousto-Optic Modulator
CCD	Charge Coupled Device
EDFA	Erbium Doped Fibre Amplifier
EYDFA	Erbium/Ytterbium Doped Fibre Amplifier
FBG	Fibre Bragg-Grating
FOM	Figure of Merit
FWHM	Full Width Half Maximum
GVM	Group Velocity Mismatch
IR	Infrared
ITO	Indium Tin Oxide
LIPP	Laser Induced Pulse Pressure
MCVD	Modified Chemical Vapour Deposition
MFT	Maker's Fringe Technique
NA	Numerical Aperture
NBOHC	Non Bridging Oxygen Hole Centre
OSA	Optical Spectrum Analyzer
PL	Photoluminescence
PMT	Photomultiplier Tube
PPSF	Periodically Poled Silica Fibre
QC	Quantum Cryptography
QPM	Quasi-Phase Matching
SHG	Second Harmonic Generation
SH	Second Harmonic
SI	International Unit System
SMF	Single Mode Fibre
SMFT	Stack Maker's Fringe Technique
SON	Second Order Nonlinearity
SVEA	Slowly Varying Envelope Approximation
TIR	Total Internal Reflection
TLS	Tunable Laser Seed

UV	Ultraviolet
WDM	Wavelength Division Multiplexing

Mathematical symbols:

$\mathbf{E}$	Electric field vector
$\mathbf{H}$	Magnetic field vector
$\mathbf{D}$	Electric displacement vector
$\mathbf{B}$	Magnetic induction field vector
$\mathbf{J}$	Total-volume current density vector
$\mathbf{M}$	Magnetization vector
$\mathbf{P}$	Polarization vector
t	Time
ω	Frequency
c	Speed of light in vacuum
μ_0	Free space permeability
ε_0	Dielectric constant of vacuum
$\mathbf{P}^L$	Linear term of the polarization vector
$\mathbf{P}^{NL}$	Non-linear term of the polarization vector
$\boldsymbol{\chi}^{(1)}$	Linear electric susceptibility tensor
n	Refractive index
$\boldsymbol{\varepsilon_r}$	Linear dielectric tensor
$\mathbf{1}$	Identity matrix
$\mathbf{P}_{\omega}^{(2)}$	Power at the ω frequency
$\mathbf{P}_{2\omega}^{(2)}$	Power at the 2ω frequency
$\boldsymbol{\chi}^{(2)}$	Second-order electric susceptibility tensor
$\mathbf{E}_{\omega}$	Component of the electric field at frequency ω
$\mathbf{E}_{\omega}^{*}$	Complex coniugate of the electric field at frequency ω
$\mathbf{A}$	Complex amplitude of the electric field
$\mathbf{A}_{\omega}$	Component of the electric field complex amplitude at frequency ω
g	Degeneracy factor
$\mathbf{k}$	Wave-vector
$\hat{\mathbf{e}}$	Electric field versor

Acknowledgements

The research carried out during a PhD would have not been possible without the help and support of many. I would like to acknowledge Pirelli Cavi e Sistemi for the sponsorship I received and particularly Dr. M. Romagnoli who gave me the opportunity to be here. I wish to express my gratitude to my supervisor, Prof. Peter Kazansky, for the trust he put in me and for his continuous technical and moral support. Sincere thanks to Dr. Eleanor Tarbox who welcomed me here and supported me throughout the whole time spent at ORC. I am indebted to everybody that has been directly involved with my research. I am truly grateful to Dr. B. Klappauf, firstly for his friendship and also for the fruitful discussions and the many suggestions. Dr. J. Mills is acknowledged for providing the glass plates irradiated with the femtosecond laser. I wish to thank Prof. K. Tanaka, for providing the samples doped with CuCl nanocrystals, but most of all for sharing hours with me in the lab. I am thankful to Dr. A. Paleari, Dr. N. Chiodini and E. Franchina who provided the tin-doped glass samples. A special thank goes to Prof. D. Nikogosyan, S. Slattery and Dr. A. Dragomir. I had the pleasure to work with them for the UV femtosecond poling work. Besides the exciting work done together, I truly appreciate their friendship and their kind and warm hospitality. I am grateful to everybody that has been involved in the GLAMOROUS project starting from its coordinator Prof. W. Margulis. Thanks for the encouragement and the many enlightening discussions. It has been an invaluable experience for me to be part of this research project. I am grateful to Dr. J. K. Sahu and A. Webb for fabricating the special fibres required for this work, to Dr. M. Ibsen and A. Canagasabey without whom the periodically poled fibres would have not been made, to Dr. J. Nilsson and especially to C. Codemard who built the laser source used for characterizing the periodically poled fibres and devoted much of his time and effort to make these experiments run quickly and successfully. I am indebted to Dr. A. Fotiadi whose immediate support has been crucial in the final stage of the GLAMOROUS project. I am especially thankful to everybody I interact with at the ORC and most of all to my research group for the fruitful discussions and support. My sincere thank to Dr. B. Klappauf, Prof. I.C.S. Carvalho, Dr. O. Deparis, and of course to Erica, Francesco, Albert and Steve who shared with me the ups and downs of the PhD life. I owe a special mention to Dr. Christos Grivas. Without him this thesis would have not been submitted on time. This thesis is dedicated to my family, for their continued moral support and patience, and to my friends, too many to be mentioned here. Their encouragement and support has been priceless and endless.

To my Family
and dearest Friends

Chapter 1

General introduction

1.1 Motivation and aims

Glass fibres are a key element for photonics applications and optical telecommunications. Silica has a dominant position because of its superior optical properties such as low loss, large transparency spectral range, high optical damage threshold and because of its low fabrication cost. Optical amplifiers can be fabricated by doping fibres with erbium, and also fibre lasers, whereby the gain is provided by doping with erbium, ytterbium or neodymium, are now commercially available. Moreover important passive optical elements such as fibre Bragg gratings mirrors and filters are straightforwardly integrated in fibres. However glass has intrinsically a very low optical nonlinearity [4], and because of its inversion symmetry on a macroscopic scale, it is not naturally a second-order nonlinear (SON) material which enables for frequency conversion and electro-optic modulation [5, 6].

Therefore, for frequency doubling of lasers, crystalline materials with second-order nonlinear properties such as lithium triborate (LBO), potassium titanyl phosphate (KTP) or beta barium borate (BBO) have to be used. Lithium niobate ($LiNbO_3$) is especially used for electro-optic modulation, although, the coupling of fibre to crystals is not ideal due to the refractive index mismatch. III-V semiconductor materials, on the other hand are attractive for frequency conversion because of the high second-order nonlinearity. However, III-V semiconductors exhibit various disadvantages, such as to having high refractive index that leads to coupling losses and to require complicated processing during manufacturing. A technology that could integrate into fibres active functionalities based on second-order nonlinear effects, would be highly desirable, but the glass inversion symmetry prevents this option.

New perspectives were opened by the technique of glass poling, that proved to induce second-order nonlinearity in silica [7], in a variety of glass compositions [8, 9, 10, 11] and in germanosilicate fibres and waveguides [12, 13]. Second-order nonlinear optical effects

can be induced in glass by applying a high electric field while simultaneously heating it at elevated temperatures. This treatment is known as thermal poling. This observation has excited considerable interest because it suggests that efficient all-glass linear electro-optic modulators and frequency converters are imminent [12, 14, 15, 16]. Considering that interaction lengths tens of cm long are feasible in optical fibers (compared to few cm in ferroelectric crystals), nonlinearities of 1 pm/V place silica glass in the position of a serious potential rival to the aforementioned nonlinear crystals which have second-order nonlinearity of the order of 10 pm/V.

For frequency conversion, the potentialities of poled fibres against nonlinear crystals, can be quantified by defining a figure of merit for the process. The efficiency is higher for higher second order optical nonlinearity $\chi^{(2)}$, for longer interaction length L and for higher intensity of the pump I. Conversely, the efficiency is reduced by the propagation losses α and it is also reduced in material having higher index of refraction. Overall, as will be derived in section 2.3, the figure of merit (FOM) can be expressed by the following equation

$$FOM = \frac{\left|\chi^{(2)}\right|^2 \cdot L^2 \cdot I}{\alpha \cdot n^3},$$

from which the advantages of using silica with respect to nonlinear crystals appear evident:

1. Silica has higher damage threshold ($\sim \ 10^5\,\mathrm{MW/cm^2}$ for nanosecond or even higher for femtosecond pulses)as compared to $LiNbO_3$ or other nonlinear crystals ($\sim \ 10^2 - 10^3\,\mathrm{MW/cm^2}$). This means that higher intensities can be used before the material undergoes damage.

2. Silica can also be made into very low loss ($\alpha = 0.2\,\mathrm{dB/km}$) waveguiding structures, optical fibres.

3. The chromatic dispersion of silica around 1.5 μm is much lower than for crystals allowing the use of longer interaction lengths for the same bandwidth. In this way, even if the nonlinearity is smaller, the previously defined figure of merit attains similar values for both materials. The comparison becomes even more favorable considering the frequency doubling of ultrashort pulses, where LBO or KDP (for high power levels), having a wider bandwidth and $\chi^{(2)} \sim \ 1\,\mathrm{pm/V}$ are commonly used.

4. Finally silica is relatively cheap and easy to fabricate.

All these characteristics make a glass optical fibre, possessing second-order nonlinearity, particularly attractive for the frequency doubling of high peak power, short-pulsed, mode-locked or Q-switched fibre lasers. Fibre lasers doped with rare-earth such as

erbium ($\lambda = 1525 - 1570\,\text{nm}$), ytterbium ($975 - 1150\,\text{nm}$) or neodymium ($890 - 940$) are protagonists of a rapid development and can now be considered as a serious alternative to diode pumped solid state lasers [17]. Frequency doubling of these sources would expand the range of available wavelengths into the visible [18].

In the past, there have been several attempts to demonstrate efficient frequency doubling of high peak-power picosecond [19], femtosecond [20] and nanosecond sources [12]. Since nonlinear crystals have typically ten times the nonlinearity of a poled fibre, the length of a poled fibre must be ten times longer than in crystals to compensate. From the technological point of view the major difficulty is to maintain the phase coherence between the driving frequency and the wavelets of the second harmonic for the whole length of the device. The two waves travel, in fact, with different velocities, owing to dispersion. The most effective solution is offered by *Quasi-phase matching* (QPM), in which a steady phase slippage between the SH and pump wave is introduced by periodically modulating the nonlinearity in order to compensate for the dispersion [21].

So far QPM has been successfully implemented in poled silica fibres by using both periodic comb electrodes [20] and periodic UV erasure [22]. In 1999 frequency doubling in quasi-phase matched germanosilicate optical fibre was reported [12]. Up to 75 mm long $\chi^{(2)}$-gratings were fabricated by thermal poling in vacuum and periodic electrodes defined by standard photolithography on the flat surface of a D-shape fibre. Average conversion efficiency of 21%, defined as the ratio of the second harmonic (SH) power over the pump power, was demonstrated for pump peak powers as high as 4 kW corresponding to a normalized conversion efficiency of $5 \times 10^{-3}\%/\text{W}$. However, the photolithographic process limits the device length to about 10 cm thus preventing scalability to longer devices and hence to higher conversion efficiency.

One of the aims of this thesis has been the development of a novel technology that would allow fabrication of $\chi^{(2)}$-gratings up to one meter long. A *continuous periodic UV erasure* technique has been developed, and experimentally demonstrated. For the first time, the periodic nonlinearity was created step by step, by focusing the output from a frequency doubled Ar^{+}-laser on the core of the poled fibre and translating along it. During the movement, the UV light was flashed intermittently in synchronization with the translation stage. Up to $\simeq 25$ cm long QPM gratings in poled silica fibres were fabricated, limited only by the travel range of the translation stage.

The periodic UV erasure technique is at the basis of the demonstration of the truly all-fibre frequency doubling of a fibre-laser. 3.6 mW of red light in the fundamental mode was obtained by frequency doubling from 1554.8 nm to 777.4 nm in quasi-phase matched periodically poled silica fibre. An average conversion efficiency of 2.4% was achieved in a 11.5 cm long device with pump peak power of only 108 W compared to 4 kW used in the previous works [12]. The corresponding conversion efficiency, normalized for the pump power, is $\eta = 2.2 \times 10^{-2}\%/\text{W}$ and is the highest ever reported for poled

fibres. As will be outlined in section 9.3 these values are already high enough to achieve efficiencies of practical interest in frequency doubling of commercial fibre laser sources.

Besides the work on periodically poled fibres, there has been in this thesis a considerable amount of research effort focused on gaining a deeper knowledge about fundamental aspects of poling. Poling of novel glass systems and new poling methods for higher second-order nonlinearity have been tested. The stability of poling, which is an important issue for practical applications, has been investigated in bulk glasses. These studies have benefited from the development of a new characterization technique.

The reason for this work finds its foundation in the aforementioned figure of merit which would be even more advantageous if one could enhance the $\chi^{(2)}$ induced in the glass. Researchers have been trying poling methods other than thermal poling to increase the second-order nonlinearity. Corona poling [23], electron beam poling [24], CO_2 laser assisted poling [25] and UV poling [26] have been demonstrated. The latter produced in Ge-doped silica, SON about 10 times higher than in thermally poled silica [27]. The claim was made that orientation of bonds in the germano-silica matrix or the nucleation of micro-crystals were responsible for the increased $\chi^{(2)}$. Nonetheless such high nonlinearities have never been reproduced by independent groups.

This thesis led to the discovery of a new poling method [28]: UV-femtosecond poling, where two-photon absorption of femtosecond UV pulses, inn the presence of an applied electric field, creates a permanent space-charge in silica glass. In contrast to the traditional UV poling, this technique is not restricted to germano-silicate glasses, rather, it has been demonstrated in pure silica glass. The maximum value of the induced second-order nonlinearity was about 0.02 pm/V with the nonlinearity extending over the whole sample thickness. A rectification model [5, 7], $\chi^{(2)} = 3\chi^{(3)}E_{\mathrm{dc}}$ with $\chi^{(3)}$, being the third-order nonlinear susceptibility, equal to $2 \times 10^{-22}\,\mathrm{m^2V^{-2}}$ for silica [29] and the applied electric field E_{dc} equal to 200 kV/cm, gives a predicted $\chi^{(2)}$ of 0.01 pm/V in remarkable agreement with the measured value. If the same experiment is performed in a twin-hole fibre where the electrodes are separated by only $\simeq 10\,\mu$m and surrounded by a glass insulator, the applied field can be much higher being only limited by the dielectric strength of silica at room temperature (2×10^9 V/m [30, 31]). We can tentatively predict a $\chi^{(2)}$ exceeding 1 pm/V.

Modification of silica by doping or special pre-treatment, is another route followed by researchers for enhancing the value of the induced second-order nonlinearity of silica whilst keeping its excellent optical properties. From this point of view, probably, the most exciting result was the enhancement, by approximately a factor of ten, in the $\chi^{(2)}$ induced by thermal poling in synthetic silica after annealing at elevated temperatures and exposure to UV pulses from a KrF excimer laser [32]. Both the annealing and the UV exposure were believed to introduce point defects in the silica matrix, in particular non bridging oxygen hole centres (NBOHC), that would make the glass more prone to

poling. As a result of the process, synthetic silica, a grade of silica in which thermal poling proved to be inefficient, showed the same level of second-order nonlinearity as fused silica ($\simeq 1\,\mathrm{pm/V}$). Inspired by this work we studied the effect of irradiation, by a focused IR femtosecond laser, on fused silica samples. It is known that femtosecond irradiation, by a multiphoton absorption process, violently breaks the Si-O covalent bonds and defects, such as oxygen deficiency centers, E' centers and NBOHC, are created inside the silica as well as densification [33]. For the first time during this thesis work, silica pre-treatment by exposure to femtosecond pulses was proved to enhance the ability of the glass to freeze the electrostatic field induced by thermal poling, leading to higher nonlinearity [34]. This novel technique, which make it possible to achieve structural modification in the glass with micro-scale resolution, was used for the fabrication of a $\chi^{(2)}$ grating with $20\,\mu$m period in bulk glass.

Our work covered also poling of nano-composite silicate glasses aiming at higher $\chi^{(2)}$ through a resonant enhancement of $\chi^{(3)}$ close to the surface plasmon resonance of gold nanocluster dispersed in the silica matrix [35]. The work was motivated by the observed resonant enhancement of $\chi^{(2)}$ at the surface plasmon resonance in silver doped silica glass [36]. In our experiment, though, we did not observe any significant improvement [35]. Poling of tin-doped silica glass fabricated by sol-gel technique produced a very interesting photosensitive second-order nonlinear glass having the same nonlinearity as fused silica. The issue of the stability of the nonlinearity in poled glass has been addressed and we demonstrated that engineering of the glass composition can lead to stable second-order nonlinearity in NA35 glass, a commercial alkali-free silicate glass produced by Nippon Sheet Glass [37]. Isothermal annealing experiments revealed that poled fused silica glass is stable for over 30 years.

A further contribution of this thesis to the field of poling is the development of a new, all-optical, characterization technique which enables accurate determination of the $\chi^{(2)}$ in poled glasses [38]. For accurate estimates of the second-order nonlinearity, it is necessary to measure the thickness of the nonlinear optical layer, which is not straightforward in thin nonlinear samples like in thermally poled glasses. Although it is a destructive technique, etching in hydrofluoric acid is typically used for the purpose of measuring the thickness of the nonlinear region [39]. Our method introduced the use of a stack of identical poled glasses during tests for second-harmonic generation. For the first time we suggested that the information about the thickness of the nonlinear region is encoded in the SH light power by the interference between the SH light generated in the two optical layers. Making use of the same stack configuration a group in Stanford demonstrated that the whole profile of the nonlinearity could be retrieved and not only its thickness [40]. Recently, an interferometric method based on a stack of a quartz plate and a poled glass which also enables the profile of the nonlinearity to be retrieved, has been developed by a group in Montreal [41]. These recent publications, together with refinements of the etching methods being published in the last couple of years [42, 43]

testify to the importance given to the characterization techniques as a tool for gaining insight on the physics of poling and support this way towards the development of devices. In this respect the works aimed at the determination of the $\chi^{(2)}$-profile find their immediate applications in poling of glass fibres and waveguides where it is necessary to maximize the overlap between the nonlinear region and the core [44].

1.2 Thesis overview

In chapter two the theoretical background for second-order nonlinear processes is addressed considering both free and guided propagation of the optical waves.

In chapter three an historical review of the research carried out in the poling field is given. The fundamental aspects of the physics of poling are presented following the argumentations that have characterized the scientific debate in this field for the last 15 years. Particular emphasis has been given to specific topics such as "poling methods" and poling of "non-silicate glasses" because they were important to make the choice of the best poling method and glass composition for the development of a frequency doubler device which is one of the aims of this thesis work. The review of the scientific breakthroughs in the field of electro-optic modulators and frequency converters is also covered.

In chapter four a detailed analysis of the Maker's fringe technique (MFT) is given and its limitations are shown. Such a detailed analysis was necessary to introduce the "Stack Maker's fringe technique" (SMFT) that has been developed in this thesis to overcome the MFT limitations. Both MFT and SMFT were used in this thesis for the characterization of bulk poled samples given in chapter five.

In chapter five our UV-femtosecond poling technique is presented together with the studies on nanocomposite glasses, IR-femtosecond pretreatment of silica and stability of the second-order nonlinearity. In the last section of this chapter various poling methods and type of glasses for poling have been compared on the basis of both the literature review and of the experiments presented in the chapter. A critical discussion in view of the fabrication of a frequency doubler based on periodically poled optical fibres is presented. In this respect, the most important criteria considered were the reproducibility of the results and the stability of the nonlinearity. On this basis, the poling method and type of glass to be used for the development of the frequency doubler fibre device, have been chosen.

In chapter six are outlined the considerations that guided us in making the choice of the fibre design and fibre parameters for the highest conversion efficiency and highest compatibility with standard optical fibres. Details about the fibre that was fabricated and used for the frequency doubler are also given in this chapter.

Chapter seven is devoted to the assessment of the periodic UV erasure technique. Here are also presented the numerical studies for the determination of the quasi-phase matching period in the fibre to be used for the demonstration of the all-fibre frequency doubling of fibre laser. The sensitivity of the QPM condition to variations in the fibre parameters have been estimated. The experimental validation of the numerical simulation is also given.

In chapter eight the fabrication of the periodically poled fibres is described. In particular, the implementation of the continuous periodic UV erasure for the fabrication of long $\chi^{(2)}$-gratings is given in this chapter, together with the realization of the truly all-fibre frequency doubling of a fibre laser.

Chapter nine is a summary of the achievements presented in this thesis. The potential of the periodically poled fibres with the efficiency demonstrated in this thesis work is discussed for practical applications of frequency doubled fibre lasers and as a rugged all-fibre source of entangled photon-pairs for quantum cryptography.

Finally, a list of the publications by the author is given.

Chapter 2

Parametric processes in optical fibres

2.1 The nonlinear wave equation

The starting point of the discussion are the Maxwell's equations in the time domain for the macroscopic variables given here for the international unit system (SI):

$$\boldsymbol{\nabla} \times \mathbf{E}(t) = -\frac{\partial}{\partial t}\mathbf{B}(t) \tag{2.1}$$

$$\boldsymbol{\nabla} \times \mathbf{H}(t) = \varepsilon_0 \frac{\partial}{\partial t}\mathbf{E}(t) + \mathbf{J}(t) \tag{2.2}$$

$$\boldsymbol{\nabla} \cdot \mathbf{D}(t) = 0 \tag{2.3}$$

$$\boldsymbol{\nabla} \cdot \mathbf{H}(t) = 0 \tag{2.4}$$

with

$$\mathbf{D}(t) = \varepsilon_0 \mathbf{E}(t) + \mathbf{P}(t) \tag{2.5}$$

$$\mathbf{B}(t) = \mu_0 \mathbf{H}(t) + \mathbf{M}(t) \tag{2.6}$$

μ_0 being the free space permeability, ε_0 the dielectric constant of vacuum, $\mathbf{B}(t)$ the magnetic induction field, $\mathbf{H}(t)$ the magnetic field, $\mathbf{E}(t)$ the electric field and $\mathbf{D}(t)$ the electric displacement. $\mathbf{J}(t)$ is the total-volume current density. In the following discussion we will focus on the polarization induced in a nonlinear material by the electric field, therefore we will consider materials with no permanent polarization. We will also assume that the main contribution to $\mathbf{J}(t)$ is due to the polarization current $\partial \mathbf{P}(t)/\partial t$, thus neglecting any effects due to the conduction current that are rigorously absent in dielectrics with only bound charges. Moreover, because in optics we are mainly concerned with non-magnetic media, we will neglect the magnetization vector $\mathbf{M}(t)$, too.

After simple algebraic manipulations on the Maxwell's equations (2.1), the wave equation in the time domain is given as:

$$\boldsymbol{\nabla} \times \boldsymbol{\nabla} \times \boldsymbol{E}(t) = -\frac{1}{c^2}\frac{\partial^2 \mathbf{E}(t)}{\partial t^2} - \mu_0 \frac{\partial^2 \mathbf{P}(t)}{\partial t^2}. \tag{2.7}$$

Since this chapter is concerned with Second Harmonic Generation (SHG), from hereafter we will use the wave equation expressed in the frequency domain:

$$\boldsymbol{\nabla} \times \boldsymbol{\nabla} \times \mathbf{E}(\omega) = \frac{\omega^2}{c^2}\mathbf{E}(\omega) + \mu_0 \omega^2 \mathbf{P}(\omega). \tag{2.8}$$

When the electric fields involved are small compared to the atomic electric fields, the response of the medium, i.e. the polarization, is linear in the applied electric field. We have

$$\mathbf{P}^L(\omega) = \varepsilon_0 \boldsymbol{\chi}^{(1)} \cdot \mathbf{E}(\omega) \tag{2.9}$$

$\boldsymbol{\chi}^{(1)}$ being the linear electric susceptibility, which in isotropic media is a simple proportionality factor defining the index of refraction: $n(\omega) \equiv \Re e\sqrt{(1+\chi^{(1)})}$. On the other hand, when the electric fields are of the same order of magnitude as the atomic electric fields the nonlinear response of the material cannot be neglected anymore. The nonlinear regime can be described by the Maxwell's equations themselves provided that we express the polarization $\mathbf{P}(\omega)$ as the sum of a linear (eq. (2.9)) and a nonlinear contribution ($\mathbf{P}^{\mathrm{NL}}(\omega)$):

$$\mathbf{P}(\omega) = \varepsilon_0 \boldsymbol{\chi}^{(1)} \cdot \mathbf{E}(\omega) + \mathbf{P}^{\mathrm{NL}}(\omega). \tag{2.10}$$

With such a definition, and by substituting eq. (2.10) into eq. (2.8), the wave equation describing the nonlinear regime is finally obtained:

$$\boldsymbol{\nabla} \times \boldsymbol{\nabla} \times \mathbf{E}(\omega) = \frac{\omega^2}{c^2}\boldsymbol{\varepsilon_r}(\omega) \cdot \mathbf{E}(\omega) + \mu_0 \omega^2 \mathbf{P}^{\mathrm{NL}}(\omega) \tag{2.11}$$

where $\boldsymbol{\varepsilon_r}(\omega)$ denotes the linear dielectric tensor defined as

$$\boldsymbol{\varepsilon_r}(\omega) = \mathbf{1} + \boldsymbol{\chi}^{(1)}. \tag{2.12}$$

In the case of SHG, eq. (2.11) constitutes a set of two wave equations, one for the component of the electric field at frequency ω and the other for the component at 2ω. The equations at ω and 2ω are coupled through the nonlinear polarization term $\mathbf{P}^{\mathrm{NL}}(\omega)$ given, in terms of its frequency component, by [6]:

$$\begin{aligned} \mathbf{P}^{(2)}_{\omega} &= g\varepsilon_0 \boldsymbol{\chi}^{(2)} | \mathbf{E}_{2\omega} \mathbf{E}^*_{\omega} \\ \mathbf{P}^{(2)}_{2\omega} &= g\varepsilon_0 \boldsymbol{\chi}^{(2)} | \mathbf{E}_{\omega} \mathbf{E}_{\omega} \end{aligned} \tag{2.13}$$

.

g being a degeneracy factor. For second harmonic generation $g = 1/2$, whereas $g = 1$ for linear absorption/emission processes, and linear refractive index. Through nonlinear coupling, energy can be transferred back and forth between waves so that the nonlinear polarization acts as a source for the electric fields propagating inside the nonlinear medium.

It is worth noting here that, in the absence of the source term, i.e. in the linear regime, eq. (2.11) has solutions of the form of plane waves propagating with velocity $c/n(\omega)$. In order to find the solution for the nonlinear wave equation (2.11), one is then tempted to retain the idea of propagating plane waves but with their amplitude and phase modified by the nonlinearity. We attempt a solution in the form of

$$\mathbf{E}(\omega) = \mathbf{A}(\omega)e^{i\mathbf{k}\cdot\mathbf{r}} \tag{2.14}$$

with

$$\mathbf{k} = \frac{\omega}{c} n_\omega \hat{\mathbf{s}} \tag{2.15}$$

and $\hat{\mathbf{s}}$ unit vector in the propagation direction. In general $\mathbf{A}(\omega)$ will be a function of the three coordinates $\hat{x}, \hat{y}, \hat{z}$.

We will now consider further approximations necessary to solve eq. (2.11).

- First of all we will assume that $\mathbf{A}(\omega)$ are **plane waves** propagating in an arbitrary chosen z direction. $\mathbf{k} \cdot \mathbf{r}$ thus reduces to $\pm kz$.
- Moreover we will consider a case in which the electric field vector is always orthogonal to the wave vector: $\hat{\mathbf{e}} \cdot \hat{\mathbf{s}} = 0$. This assumption is strictly valid only in isotropic media or media with cubic symmetry. Under these hypotheses the expression appearing in the left-hand side of eq. (2.11) can be simplified into:

$$\boldsymbol{\nabla} \times \boldsymbol{\nabla} \times \mathbf{E}(\omega) \rightarrow -\frac{\partial^2}{\partial z^2}\mathbf{E}(\omega). \tag{2.16}$$

- Furthermore we will assume the **Slowly Varying Envelope Approximation** (SVEA). As mentioned earlier, wave coupling in a nonlinear medium results in energy transfer among waves. Hence the wave amplitudes are expected to change during propagation. The SVEA approximation, expressed by

$$\left|\frac{\partial^2}{\partial z^2}\mathbf{A}(\omega)\right| \ll \left|k\frac{\partial}{\partial z}\mathbf{A}(\omega)\right| \tag{2.17}$$

  is justified when the variation of $\mathbf{A}(\omega)$, both in amplitude and phase, can be

considered small over distances of the order of a wavelength.

The aforementioned approximations lead to:

$$\frac{\partial}{\partial z}\mathbf{A}(\omega) = i\frac{\mu_0\omega^2}{2k}\mathbf{P}^{\mathrm{NL}}(\omega)e^{-ikz} \tag{2.18}$$

We are now ready to write the vector wave equation given in eq. (2.18) both for the pump and the second-harmonic:

$$\begin{aligned}\frac{\partial}{\partial z}\mathbf{A}_\omega &= i\,\frac{\mu_0\omega^2}{2k_\omega}\mathbf{P}^{\mathrm{NL}}_\omega e^{-ik_\omega z}\\ \\ \frac{\partial}{\partial z}\mathbf{A}_{2\omega} &= i\,\frac{\mu_0(2\omega)^2}{2k_{2\omega}}\mathbf{P}^{\mathrm{NL}}_{2\omega} e^{-ik_{2\omega} z}\end{aligned} \tag{2.19}$$

where $\mathbf{A}_\omega$ and $\mathbf{P}^{\mathrm{NL}}_\omega$ are the monochromatic frequency components of $\mathbf{A}(\omega)$ and $\mathbf{P}^{\mathrm{NL}}(\omega)$, respectively. Defining $\mathbf{A}_\omega = \hat{\mathbf{e}}_\omega A_\omega$, and making the scalar product $\hat{\mathbf{e}}\cdot$ at both sides of the previous equations, we can write in a more convenient form:

$$\begin{aligned}\frac{\partial}{\partial z}A_\omega &= i\,\frac{\mu_0\omega^2}{2k_\omega}\hat{\mathbf{e}}_\omega\cdot\mathbf{P}^{\mathrm{NL}}_\omega e^{-ik_\omega z}\\ \\ \frac{\partial}{\partial z}A_{2\omega} &= i\,\frac{\mu_0(2\omega)^2}{2k_{2\omega}}\hat{\mathbf{e}}_{2\omega}\cdot\mathbf{P}^{\mathrm{NL}}_{2\omega} e^{-ik_{2\omega} z}.\end{aligned} \tag{2.20}$$

Similarly the explicit form of the second order nonlinear polarization components $\mathbf{P}^{(2)}$ defined in eqs. (2.13) is given by:

$$\begin{aligned}\mathbf{P}^{(2)}_\omega &= \varepsilon_0\,\boldsymbol{\chi}^{(2)}\Big|\hat{\mathbf{e}}_{2\omega}\hat{\mathbf{e}}_\omega A_{2\omega}A^*_\omega e^{i(k_{2\omega}-k_\omega)z}\\ \\ \mathbf{P}^{(2)}_{2\omega} &= \varepsilon_0\,\frac{1}{2}\boldsymbol{\chi}^{(2)}\Big|\hat{\mathbf{e}}_\omega\hat{\mathbf{e}}_\omega A_\omega A^*_\omega e^{2ik_\omega z}\end{aligned} \tag{2.21}$$

Substitution of eqs. (2.21) into eqs. (2.20) gives the evolution for the pump and second harmonic electric fields:

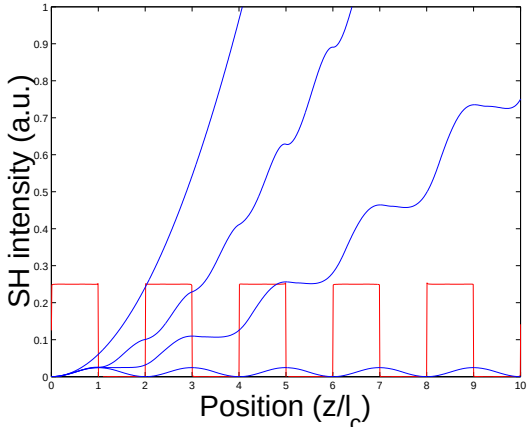

FIGURE 2.1: Intensity of SH wave along the propagation direction for (blue) non-phase matching, (green) phase-matching, (red) quasi-phase matching

$$\begin{aligned} \frac{\partial A_\omega}{\partial z'} &= i\,\frac{\omega^2}{k_\omega c^2}\,d_{\text{eff}}(z)A_{2\omega}A_\omega^* e^{i\Delta k z} \\ \frac{\partial A_{2\omega}}{\partial z} &= i\,\frac{(2\omega)^2}{2k_{2\omega}c^2}\,d_{\text{eff}}(z)A_\omega^2 e^{-i\Delta k z} \end{aligned} \tag{2.22}$$

Δk being equal to $k_{2\omega} - 2k_\omega$.

We have also introduced the effective nonlinear optical coefficient defined as:

$$d_{\text{eff}}(z) \equiv \frac{1}{2}\left[\hat{\mathbf{e}}_{2\omega}\cdot\chi^{(2)}|\hat{\mathbf{e}}_\omega\hat{\mathbf{e}}_\omega\right]. \tag{2.23}$$

2.2 Quasi-phase matching

It was mentioned earlier in this chapter that during the propagation of a pump beam along a nonlinear material, there is a continuous transfer of power from the pump to the SH field and, subsequently, back from the SH field to the pump (Fig. 2.1). Mathematically, this is expressed by the fact that eqs. (2.22) are coupled through the wave-vector mismatch Δk. Physically the flow of power, back and forth between pump and SH, is a consequence of the different velocities of the two waves in the medium owing to the material dispersion. The flow of power is reversed each time the pump and SH fields become π-out of phase, that is after propagating for a *coherence length* defined as $l_c = \pi/\Delta k$. A continuous growth of the SH power is obtained if the wave-vector mismatch Δk is equal to zero, i.e when $n^\omega = n^{2\omega}$. Because of dispersion this condition in general does not hold, but it is true for example in the case of *birefringent phase matching* where the different refractive indexes of the ordinary and extra-ordinary rays

in anisotropic crystals are matched for a particular direction of propagation of the light in the crystal. Birefringent phase matching is obtained in $LiNBO_3$ with the pump field having extraordinary polarization ($n^{\omega} = n_e^{\omega}$) and the SH field having ordinary polarization ($n^{2\omega} = n_o^{2\omega}$). When this condition is fulfilled, only for specific wavelengths and angles of propagation of the light within the crystal, the second-harmonic field grows linearly with the length of propagation and, consequently, its intensity grows quadratically as shown by the green curve in Fig. 2.1.

Compared to birefringent phase matching, a wave-guiding structure can offer some degree of flexibility as the waveguide dispersion can be used to compensate for the material dispersion [45]. Different modes travel at different propagation velocities meaning that it is possible to design the waveguide in order to match the velocity of the fundamental mode at ω with the one of a higher order mode at frequency 2ω. However, since high order modes are necessary to compensate for large mismatches, *modal phase matching* gives poor output beam quality and low conversion efficiency due to the small overlap between the fields involved.

A third way was proposed in 1962 [21] that, rather than rely on perfect phase coherence between the driving frequency and the wavelets of the second harmonic, one could compromise and allow a steady phase slippage between them. The suggestion was that by modulating the nonlinear coefficient periodically one could compensate for the phase mismatch. This method, known as *Quasi-phase matching* (QPM), has several advantages over birefringent and modal phase matching. It allows one access to new wavelengths, higher efficiencies, and noncritical interaction geometries, and it provides flexibility and new possibilities for phase matching, especially in materials in which the birefringence is not high enough to compensate for the dispersion and in which modal phase matching is not desirable because one wants to avoid generation of light in higher-order modes.

Supposing the nonlinear coefficient is a periodic function in z with period Λ, for example a square wave, it can then be expressed in terms of a Fourier expansion:

$$d(r, \phi, z) = \sum_q \tilde{d}_q(r, \phi) e^{-iK_q z} \tag{2.24}$$

where

$$K_q = \frac{2\pi q}{\Lambda} \tag{2.25}$$

and

$$\tilde{d}_q(r, \phi) = \frac{1}{\Lambda} \int_0^{\Lambda} d(r, \phi, z) e^{iK_q z} \tag{2.26}$$

2.3 Second-harmonic generation in optical fibres

Throughout this section the *weakly guiding approximation* for cylindrical fibres will be used [46]. This approximation implies $n_{\text{core}} - n_{\text{clad}} \ll 1$, which holds in the fibres used in the experiments presented in this thesis as $\Delta n \simeq 0.02$. Under this approximation, it has been shown that any electromagnetic field propagating in a fibre can be expressed as a linear combination of the modes that are solution to the modal equation [47]. In the weakly guiding approximation, the exact fibre modes are well approximated by the linearly polarized modes LP_{lm}, therefore the electromagnetic field in the fibre is expressed by:

$$\mathbf{E}(z,r,\phi,t) = \frac{1}{2}\sum_{l,m}\left[A_{lm}(z)\text{LP}_{lm}(r,\phi)e^{i(\beta_{lm}z-\omega t)} + c.c\right] \tag{2.27}$$

where $\beta_{lm} = \frac{\omega}{c}\left(n_{\text{eff}}^{\omega}\right)_{lm}$ is the propagation constant for the l,m mode which takes into account both material and waveguide dispersion through the mode effective index $\left(n_{\text{eff}}^{\omega}\right)_{lm}$. The LP_{lm} modes are normalized in such a way that:

$$\langle \text{LP}_{lm}|\text{LP}_{jk}\rangle = \delta_{jl} \tag{2.28}$$

Following the choice of the normalization the LP modes have the dimension of the inverse of length. The evolution equations for pump and SH electromagnetic fields for quasi-phase matching second-harmonic generation in a waveguiding structure are obtained likewise 2.22.

$$\frac{\mathrm{d}}{\mathrm{dz}}A_{2\omega}(z) = i\frac{\omega}{n_{2\omega}^{\text{eff}}c}A_{\omega}^{2}(z)\,d_{\text{eff}}^{\text{SH}}\,I_{\text{ovl}}^{\text{SH}}\sum_{q}e^{i[\beta(2\omega)-2\beta(\omega)-K_q]z} \tag{2.29}$$

$$\frac{d}{dz}A_{\omega}(z) = i\frac{\omega}{n_{\omega}^{\text{eff}}c}A_{2\omega}(z)A_{\omega}^{*}(z)d_{\text{eff}}^{\text{SH}}\,I_{\text{ovl}}^{\text{SH}}\sum_{q}e^{-i[\beta(2\omega)-2\beta(\omega)-K_q]z} \tag{2.30}$$

In analogy with 2.22 the effective nonlinear coefficient should be substituted by

$$d_{\text{eff}}^{\text{SH}} = \frac{\iint_{S_{\text{fibre}}}\tilde{d}_q(r,\phi)\text{LP}_{2\omega}(r,\phi)\;\text{LP}_{\omega}^{2}(r,\phi)\,\mathrm{d}\sigma}{I_{\text{ovl}}^{\text{SH}}} \tag{2.31}$$

where

$$I_{\text{ovl}}^{\text{SH}} = \iint_{S_{\text{fibre}}}\text{LP}_{2\omega}(r,\phi)\;\text{LP}_{\omega}^{2}(r,\phi)\,\mathrm{d}\sigma \tag{2.32}$$

Because of the choice of the normalization, eq. 2.28, the LP modes have the dimension of the inverse of a length. The overlap integral $I_{\text{ovl}}^{\text{SH}}$ depends on the mode overlap only

and it has the dimension of the inverse of a length. By introducing this factor, the dependence of the nonlinear coefficient from the transversal coordinate is lumped into d_{eff}.

The wave-vector mismatch is now:

$$\Delta K_q = \beta(2\omega) - 2\beta(\omega) - \frac{2\pi q}{\Lambda} \tag{2.33}$$

For every q there is a value of Λ for which the wave-vector mismatch is null and quasi-phase matching is achieved. As the expression for d_{eff} contains the coefficients of a Fourier expansion, which decreases with increasing index q value, the most efficient quasi-phase matching is obtained for $q = 1$. This case is referred to as first-order quasi-phase matching.

The second-harmonic power P_{SH} and the efficiency η_{SH} expressed in term of the fundamental power P_ω, of the interaction length L and of $A_{ovl} = |1/I_{\text{ovl}}|^2$ is:

$$P_{\text{SH}} = \frac{2\omega^2 \left| d_{\text{eff}}^{\text{SH}} \right|^2 L^2}{\varepsilon_0 c^3 \left(n_\omega^{\text{eff}}\right)^2 n_{2\omega}^{\text{eff}}} \frac{P_\omega^2}{A_{\text{OVL}}} sinc^2\left(\frac{\Delta K L}{2}\right) \tag{2.34}$$

$$\eta_{\text{SH}} = \frac{2\omega^2 \left| d_{\text{eff}}^{\text{SH}} \right|^2 L^2}{\varepsilon_0 c^3 \left(n_\omega^{\text{eff}}\right)^2 n_{2\omega}^{\text{eff}}} \frac{P_\omega}{A_{\text{OVL}}} sinc^2\left(\frac{\Delta K L}{2}\right) \tag{2.35}$$

where

$$P(z) = \iint_{S_{\text{fibre}}} I(\mathbf{r}) d\sigma = \frac{1}{2}\varepsilon_0 c n \left|A(z)\right|^2 \tag{2.36}$$

was used. At the phase matching the value of $sinc^2$ function is one so that:

$$\eta_{\text{SH}} = \frac{2\omega^2 \left| d_{\text{eff}}^{\text{SH}} \right|^2 L^2}{\varepsilon_0 c^3 \left(n_\omega^{\text{eff}}\right)^2 n_{2\omega}^{\text{eff}}} \frac{P_\omega}{A_{\text{OVL}}} \tag{2.37}$$

Starting from the expression for the conversion efficiency a figure of merit (FOM) can be defined for the second-harmonic generation process, thus enabling one to compare the performance of second-order nonlinear materials:

$$FOM = \frac{\left|d_{\text{eff}}^{\text{SH}}\right|^2 L^2 I_{\text{MAX}}}{\alpha n^3} \tag{2.38}$$

where α is the propagation loss and I_{MAX} represents the damage threshold intensity associated with different materials. For the bandwidth, that is the range of wavelength over which the frequency conversion is efficient, in first approximation, one can write [48]:

$$\Delta\lambda \simeq \frac{0.44\lambda_\omega^2}{cL \cdot GVM} \tag{2.39}$$

with the GVM being the group velocity mismatch defined as [4]

$$GVM = \left|v_g(2\omega)^{-1} - v_g(\omega)^{-1}\right| \tag{2.40}$$

with

$$v_g(\omega) = \frac{\partial\omega}{\partial\beta}\Big|_\omega \tag{2.41}$$

In silica fibres is GVM $\simeq 19\,\text{ps/m}$ between $\lambda_1 = 1550\,\text{nm}$ and $\lambda_2 = 775\,\text{nm}$ [4]. It follows that the bandwidth of a 10 cm long periodically poled fibre, phase matching between 1550 nm and 775 nm is $\simeq 1.73\,\text{nm}$.

Chapter 3

Thermal poling

3.1 The poling process

In this chapter is reported an historical review of the research carried out in the poling field. Throughout the chapter the fundamental aspects of the physics of poling will be described following the arguments that have characterized the scientific debate in this field. The aim of the chapter is to provide the background knowledge that was necessary to make the decision about the poling method and poled glass to employ for the development, in this thesis, of the frequency doubler. However, a critical comparison between different poling technologies and materials is postponed to chapter 5 after the experimental work carried out in this thesis is presented.

Silica glass is naturally an amorphous material possessing inversion symmetry on a macroscopic scale. Consequently the vanishing $\chi^{(2)}$ makes its use for efficient second-order nonlinear processes, impossible. Nonetheless, starting from the 1980s, photoinduced SHG has been observed by many researchers when launching strong IR beams, typically from a Nd:YAG laser into an optical fibre [49, 50, 51, 52, 53]. This was the first demonstration that it was possible to break the symmetry of an amorphous material such as a glass and to induce a second-order nonlinearity. The cause of the photoinduced SHG was attributed to the coherent photo-galvanic effect, through which a static electric field, spatially modulated along the fibre, is established [54, 55, 56, 57, 58]. The electric field couples with the $\chi^{(3)}$ of the glass to give an effective $\chi^{(2)}$. The period of the self-organized electric field in the fibre alternates spatially with the exact period to provide constructive interference through quasi-phase matching. The efficiency of the frequency doubling process is high enough such that in 1986 Österberg et al. [51] could pump a dye laser with the green light produced by photoinduced SHG. Following this demonstration a considerable amount of research effort, both from the theoretical and the experimental side, has been made in order to understand the fundamental physics behind this unexpected phenomenon and to prove the technology as

a viable alternative to nonlinear crystals. Eventually, the efficiency of photoinduced SHG was found to be limited by the low value of the nonlinearity, 10^{-3} pm/V, and by the length of the self-organized QPM-grating which cannot exceed $60 - 80$ cm owing to chromatic dispersion and phase modulation [52]. Efficiencies up to few % have been demonstrated [59, 60, 61, 62, 63, 64, 65], but unfortunately this figure does not make photoinduced SHG attractive for practical applications.

A turning point in the quest for an efficient glass-based second-order nonlinear material is the work by Myers et al in 1991 [7]. The authors observed that a permanent SON could be induced in a fused-silica glass plate once heated to 250 °C - 325 °C with an applied voltage of about 3 kV -5 kV for 15 min and then cooled down to room temperature with the voltage still applied. It has been suggested that a high electrostatic field E_{dc}, appearing in a thin depletion region near the anodic surface, is responsible for the poling phenomenon, similarly to the explanation of the photoinduced SHG. Despite the vanishing $\chi^{(2)}$ in glass, the coupling between the electro-static field E_{dc} and the intrinsic third-order nonlinearity of the glass produces an effective second-order nonlinearity. By recalling the expression that relates the amplitude of the second-order nonlinear polarization with the amplitude of the interacting electric fields, the following equations are obtained in the case of SHG [6]

$$P^{(2)}(\omega+\omega) = \frac{1}{2}\chi^{(2)}(-2\omega;\omega,\omega)E(\omega)E(\omega) \quad , \tag{3.1}$$

and in the case of third order nonlinear interactions [6]:

$$P^{(3)}(0+\omega+\omega) = \frac{3}{2}\chi^{(3)}(0-\omega-\omega;0,\omega,\omega)E_{\mathrm{dc}}(0)E(\omega)E(\omega) \tag{3.2}$$

where the factor in front of the right hand side of the above equations is the degeneracy factor and corresponds to the number of independent permutations of the frequencies (0, ω, ω) times a factor 1/2 for each of the interacting fields. This factor arises from the convention chosen to express the electric field (eq. 2.27). Furthermore, when the nonlinear polarization is expressed in the same analytical form used for the electric field (eq. 2.27), the degeneracy factor is multiplied by a factor of 2 [6]. From the above equations it follows:

$$\chi^{(2)} = 3\,\chi^{(3)}\,E_{\mathrm{dc}} \tag{3.3}$$

which physically means that the interaction between the $\chi^{(3)}$ and the electro-static field (ω=0) produces, on the optical fields $E(\omega)$, the same effect as a second-order nonlinearity.

As the $\chi^{(3)}$ in silica is $2 \times 10^{-22}\,\mathrm{m^2/V^2}$ [29] and as the field strength of E_{dc} is very close to the breakdown strength of fused silica, 2×10^{9} V/m [30, 31], the $\chi^{(2)}$ in *poled* glass is expected to be ~ 1 pm/V. Indeed this was the measured value and, as it is of the same order of magnitude as the nonlinear susceptibilities of widely used nonlinear

crystals for frequency doubling, the figure of 1 pm/V justifies for the enthusiasm that thermal poling in glass had generated in the scientific community. As a comparison the values of the SON susceptibility tensor elements reported in [5] for $LiNbO_3$ are: $\chi^{(2)}_{22} = 6.2\,\mathrm{pm/V}$, $\chi^{(2)}_{31} = 11.7\,\mathrm{pm/V}$ and $\chi^{(2)}_{33} = 82\,\mathrm{pm/V}$. But poled silica glass compares better with widely used nonlinear crystals such as quartz, KDP and BBO. For quartz $\chi^{(2)}_{11}$ is 0.6 pm/V [66]). For KDP $\chi^{(2)}_{14}$ is 1 pm/V and $\chi^{(2)}_{36}$ is 0.92 pm/V. BBO has a $\chi^{(2)}_{11}$ equal to 3.8 pm/V.

The mechanism that leads to the establishment of the SON in the glass has yet to be understood and nowadays, more than 14 years later, there is not a firm conclusion. The origin of the electro-static field E_{dc}, responsible for $\chi^{(2)}$, was at the centre of the scientific debate in the early 90s. Poling had been studied before in connection with electrets and polymers [67, 68]. The application of high voltages to silica at elevated temperatures has been studied since the 1970s, although not for applications in optics [69]. From these studies it was known that alkali ions such as Na^+ and Li^+, that are present in silica as impurities, are bonded to negatively charged non-bridging oxygen (NBO) sites, and may drift under the action of electric fields. It was also known, from Myers' and co-workers' observations that the nonlinearity was located in a thin layer, $< 10\,\mu$m, under the surface of the glass plate that had been in contact with the anode electrode [7]. Two mechanisms were proposed: either the nonlinearity was caused by orientation of bonds or by the creation of a space charge field leading to a dc electronic polarization [70, 71]. It has been suggested that the high temperature involved in the poling process increases the mobility of the impurities present in the glass, mainly alkali ions such as Na^+. Hence, upon the application of an electric field, the positively charged sodium ions drift towards the cathode where they are neutralized by injected electrons. Under the hypothesis of zero ionic conductivity at the anode (blocking electrode), the ions, while migrating, leave a depleted region behind them, negatively charged and located a few microns under the anodic surface. Due to the lack of mobile charges the depleted region has a much larger resistivity than the rest of the glass. Like in a voltage divider, the applied voltage drops mainly across the more resistive depleted region. As a consequence, a large static electric field is established between the depleted layer and the anode. Kazansky and Russell distinguished between two possibilities that could arise at this stage [71]. Either orientation of NBO bonds or glass ionization could take place under the action of the high electrostatic field. In the former hypothesis, the high temperature increases the mobility of NBO dipoles, whereas the applied electric field forces them all to orient in the same direction. After cooling, the dipoles would be frozen in this direction, thus breaking the symmetry of the glass and accounting for the second order nonlinearity. In the latter hypothesis, the static field is responsible for the ionization of the glass in the anodic region, leading to the creation of a positive charge layer that screens the external field and stops the process. When the sample is cooled down the ions are trapped in their positions. A high static electric field, between the positive layer and the negatively charged region, is then frozen in the glass once again breaking its centro-symmetric

structure.

Mukherjee and co-workers used a general expression for the effective $\chi^{(2)}$ [70]:

$$\chi^{(2)} = 3\,\chi^{(3)} E_{\mathrm{dc}} + \frac{Np\,\beta}{5k_bT}\,E_{\mathrm{dc}} \tag{3.4}$$

where the first term, as shown before, accounts for the interaction between E_{dc} and the third-order nonlinearity $\chi^{(3)}(-2\omega;0,\omega,\omega)$. The second term originates from $N\beta\left\langle\cos^3\vartheta\right\rangle$ and describes the electric-field orientation of the molecular second-order hyperpolarizability β, ϑ being the angle between the molecular axis and E_{dc} and N the concentration of orientable moieties. p is the permanent dipole associated with the bond.

Nowadays there are strong arguments against a significant contribution to the effective χ^2 due to orientation of dipoles, at least in silica glass [10, 39, 72, 73, 74]. In [71], the values of the nonlinear coefficients in poled silica glass, d_{33} and d_{31} were shown to be in a ratio of 3:1. This ratio is the only one possible in the space charge scenario, although it is also compatible with dipole orientation. Observations of the cross section of poled glass through ion mass spectrometry [73] and energy dispersion spectra (EDS) [10] confirmed that the nonlinear region is actually depleted of alkali ions. Moreover, taking advantage of the variation of the hydrofluoric acid etching-rate in the presence of an electric field [39], a large electric field was proven to exist within the depleted region [75, 76]. Insights into the charge distribution have been given with a laser induced pressure pulse (LIPP) method. With this technique a positive charged layer was found at the anodic surface [74] supporting the case of either glass ionization or in-diffusion of positive ions under the high electro-static field. Although the aforementioned studies give strength to the charge migration model, the controversy between the two descriptions is not completely resolved. Data collected in further experiments reveal, according to the authors, that reorientable moieties are at the origin of the induced nonlinearity [77]. Nonetheless if such moieties are present and oriented, then the individual hyperpolarizability β can be estimated from the measured $\chi^{(2)}$ and from the dipole concentration [7]. Assuming a reasonable concentration of orientable defects in the glass of about 50 ppm, β is estimated to be many orders of magnitude larger than that of urea or 2-methyl-4-nitroaniline. Although non conclusive, the previous statement is one of the first and stronger arguments against the reorientational model [7].

3.2 Single Carrier Model

In an early paper, Von Hippel and co-workers developed a model for the space charge build-up in alkali halide crystals [78]. The model can be easily adapted to the case of positive charge carriers. According to this model, Na^+ is assumed to be the only mobile charge carrier. The anode is assumed to act as a blocking electrode. Electrical

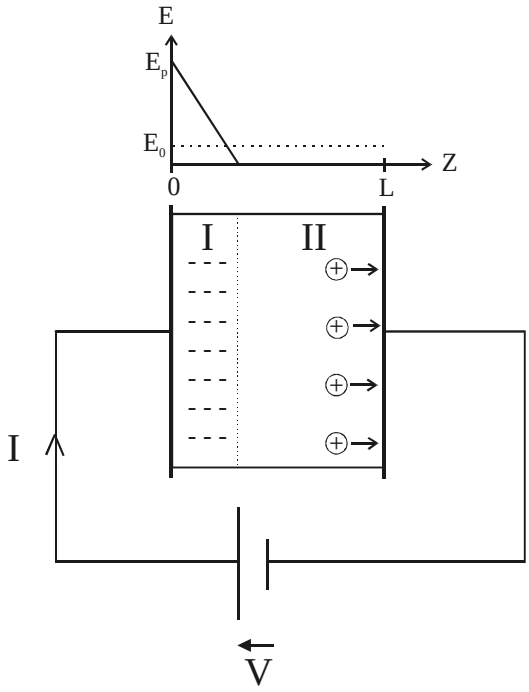

FIGURE 3.1: The single-ionic carrier model. The negatively charged depletion region (I), the neutral region (II) and the distribution of the electric field are shown in the steady-state. Also shown is the uniform field distribution in the absence of charge motion $E_0 = V/h$. This simplified picture of the poling corresponds to the early stage of the actual poling process.

neutrality requires an equal amount of fixed negative charges to be present in the glass (e.g. negatively charged non-bridging oxygens). NBO sites are assumed to be immobile. At steady state the electric-field is given by:

$$E_{\mathrm{dc}} = \frac{eN}{\varepsilon}(d_\infty - x) \qquad 0 < x < d_\infty \tag{3.5}$$

$$E_{\mathrm{dc}} = 0 \qquad x > d_\infty \tag{3.6}$$

where d_∞ is the thickness of the depleted region, e the elementary charge, N the fixed charge density associated with the nonbridging oxygen-hole centers and ε the dielectric permittivity of glass. This simple model can describe all the essential features of thermal poling. During the migration of Na^+, the charge front (at $z = d$) which separates the depletion region and the neutral region moves in the glass according to:

$$d(t) = d_\infty \tanh\left(\frac{t}{2\tau}\right) \tag{3.7}$$

with

$$d_\infty = \sqrt{\frac{2\varepsilon V}{eN}} \tag{3.8}$$

and

$$\tau = \frac{d_\infty}{2\mu E_0} \tag{3.9}$$

where μ is the effective mobility of sodium. The motion of the charge front can be measured by the current that flows through the glass. The current in the limit of $d_\infty \ll L$ is well approximated by:

$$I(t) \simeq \frac{I(0)}{\cosh^2\left(\frac{t}{2\tau}\right)} \tag{3.10}$$

where the current at $t = 0^+$ is $I(0) = AeNd_\infty/(2\tau)$ and A is the electrodes' cross section.

Using the values for fused silica reported in [30] and references therein, $\varepsilon = 3.8\varepsilon_0$, $N = 2 \times 10^{22}\,\mathrm{m}^{-3}$, $\mu_{\mathrm{Na}^+} = 1 \times 10^{-15}\mathrm{m}^2\mathrm{V}^{-1}\mathrm{sec}^{-1}$, we can estimate the thickness of the depletion region to be approximately $9\,\mu$m. The depletion region is formed on the time scale of about 20 min for a 1 mm thick sample and with 4 kV applied and it is ten times faster for a ten times thinner sample. The frozen electric field peaks at the surface in contact with the anode and its maximum value according to eq. 3.5, is $\simeq 10^9$ V/m which is very close to the value of the electrical breakdown in silica. It suggests that high field ionization stops the poling process, as envisaged in [72]. As a consequence the $\chi^{(2)}$ is also limited in silica to values of $\simeq 1$ pm/V. E_{dc} is also independent of the applied field. The applied field mainly alters the time scale of the process. E_{dc} is found to depend upon the charge carrier concentration. From this simple model it is possible to infer that a glass sample having lower charge concentration will exhibit lower nonlinearity and a wider depletion region. It is indeed the case, as measurements performed in Suprasil$^{\mathrm{TM}}$ have pointed out [79]. Suprasil is a synthetic silica glass having approximately 10 times less impurities compared to fused silica glass. After poling a 10 times smaller $\chi^{(2)}$ is induced and d_∞ is wider, generally above $20\,\mu$m. Incidentally, a larger second-order nonlinearity in synthetic silica has been induced by thermal poling if the glass had been previously thermally annealed and exposed to UV-irradiation from a KrF excimer laser [80]. Both the previous treatments are believed to produce point defects inside the silica matrix.

Quiquempois and co-workers reported the existence of a poling voltage threshold in fused silica (Infrasil$^{\mathrm{TM}}$ 301), below which is not possible to induce any second-order nonlinearity. In order to explain such a feature a model considering diffusion of charge carriers and their dissociation and recombination was introduced [31] based on the Proctor and Sutton model [81].

3.3 Multiple Carrier Model

Although the single carrier model successfully describes the general features of the poling process, it does not account for all the experimental evidence. Alley et al. found two

time scales while measuring the poling and de-poling currents [30]. This behaviour was attributed to the presence of a second charge carrier with orders of magnitude lower mobility. In-diffusion of H^+ from the atmosphere, driven by the high electrostatic field, was believed to take place. Indeed the presence of a positive charge layer between the negatively charged depleted region and the anodic surface was revealed by Kazansky et al. with a laser-induced pulse pressure (LIPP) technique [74]. Pruneri and co-workers pointed out the relevance of the poling atmosphere by performing poling in air or under vacuum (10^{-8} atm) [82]. Samples poled in vacuum exhibit wider depletion regions and consequently lower nonlinearity compared to samples poled in air for the same time. In agreement with Alley et al. [30], it was speculated that H^+/H_3O^+ may in-diffuse from the atmosphere, while poling in air, and slow down the movement of the faster species.

LIPP measurements also showed a different charge distribution for poling in vacuum and air. A positive charge layer was revealed to be present also in the samples poled in vacuum. It was therefore thought that, in vacuum, glass ionization with liberation of e^-, must take place. The same phenomenon is probably occurring in air as well, but in that case in-diffusion of positive species from the atmosphere is believed to be the dominant mechanism. More recently Faccio et al. published a study of the dynamics of thermal poling for different sample thicknesses [83]. The existence of an optimum poling time, $\simeq$ 10 min depending on sample thickness, for which the $\chi^{(2)}$ was maximized, was presented. The decrease of $\chi^{(2)}$ for longer poling times cannot be explained by a single carrier model. In order to account for the new experimental findings new models have been developed. In Alley et al. two charge carriers with vastly different mobility were considered. The same hypotheses as the Von Hippel model (see Section 3.2) were used [30]. Diffusion of ions has been considered by Godbout and Lacroix [84]. The models have shown good agreement with experimental results when applied to poling of Suprasil^{TM} silica glass. Xue-Ming Liu and co-workers have considered ionization of the glass together with in-diffusion of H_3O^+ and H^+ from the atmosphere [85, 86]. The model predicts the existence of a *ionosphere* sandwiched between the positive charge layer and the negatively charged depletion region which seems to be in agreement with the findings of [82].

3.4 Characterization Techniques

The understanding of the physical mechanism involved in thermal poling is crucial for the identification of the critical parameters affecting the process. Such a knowledge could lead towards engineering of the glass system and/or of the poling procedure for enhancing the induced second-order nonlinearity. Early on it was realized that progress was hindered by the difficulty in accessing the depletion region and obtaining information from its thickness, profile and dynamics. Hence, the improvement of characterization techniques and the development of new methods has never stopped from the early days

of poling. The Maker's fringe technique (MFT), which will be described in detail in Chapter 4, was the first method to be employed for the measurement of $\chi^{(2)}$ [7], but, unless the thickness of the nonlinear region is measured independently, the MFT is not suitable for the characterization of poled glasses when the width of the nonlinear region is thinner than one coherence length. Typically, the silica plates were etched in hydrofluoric acid solution in steps separated by a few seconds or minutes. At each step the thickness of the etched glass was measured with a profilometer and the SH signal recorded. The width of the nonlinear region was extrapolated to be the thickness for which the SH signal had disappeared [7]. Lesche et al. observed that the presence of E_{dc} affects the etching rate. Namely the etching rate of poled silica is 0.7 times slower than unpoled silica. Based on this discovery they developed an interferometric etching technique that enabled them to monitor, in real time, the evolution of the depletion region by looking at the sudden change in the etching rate [42]. In 2003 Kudlinski and co-workers proposed a very accurate method for the determination of the $\chi^{(2)}$ profile. The evolution of the SH signal is monitored as the poled sample is etched with hydrofluoric acid. The sample thickness is measured in real time using an interferometric method. The nonlinear profile was reconstructed from the full set of data by means of a layer peeling method [43]. Given that the spatial resolution is below $1\,\mu$m and that the reconstructed profile does not depend on a priori assumptions, this technique is a very powerful tool for characterizing the distribution of the nonlinearity in the poled glass and so gain knowledge about the physical processes involved in thermal poling. The nonlinear profile that was inferred for a 10 min poling of Infrasil$^{\mathrm{TM}}$ at 290°C was compatible with a multiple carrier model but not with the single carrier model. Sign reversal of the nonlinearity in the first $2\,\mu$m beneath the anodic surface was observed during poling of pre-annealed samples [87].

The aforementioned technique has the only disadvantage that samples are unusable after having been characterized. Another direction followed by researchers in order to obtain the distribution of the nonlinearity in the glass was the improving of the MFT technique. The limitation in the MFT is caused by total internal reflection of the SH light beam at the output surface of the sample being tested. Pureur et al. demonstrated a prism-assisted MFT, in which the sample was sandwiched between two prisms in order to avoid the total internal reflection. For the first time the profile of the nonlinearity, and not only its thickness, could be estimated. Best fit to the experimental data was obtained for a truncated Gaussian profile, $8\,\mu$m wide when the nonlinear coefficient decreased by a factor 1/e [88]. Quiquempois et al. suggested to use hemispherical lenses instead of the prisms [89]. The main advantage was that this configuration allowed for easier measurements as it was no longer necessary to adjust the focus of the beam on the sample for each angle. The use of cylindrical lenses in place of the hemispherical ones is a further technical improvement of the same initial idea [90]. A different approach was followed by Faccio and co-workers where a *Non-Collinear* MFT (NCMFT) was demonstrated [91]. In this technique two beams at the fundamental frequency radiation

are focused on the poled sample and SH light generated in the non-collinear direction is collected. The coherence length of such a process is about 2 μm in silica compared to the 24 μm of the collinear interaction, meaning that the NCMFT is able to resolve the spatial distribution of the nonlinearity. Best fit to the data gave a truncated Gaussian profile for poling of Herasil^{TM}1 glass plates. Guillet de Chatellus et al., also used a NCMFT but they also vary the angle between the two pump beams to increase the sensitivity to the nonlinear profile [92]. The nonlinearity profile that was inferred from the data gave credit, once more, to the existence of a double charged layer close to the anodic surface in poled glass.

In contrast to the layer peeling method mentioned before, all these techniques derived from the MFT are non-destructive. On the other hand the profile of the nonlinearity is inferred from the Maker's fringe patterns under a priori hypothesis of having a single maximum and no change in sign. This last assumption might be too crude as in some poling conditions the existence of double layer, positive (H^+, ionized glass) and negatively charged depletion region was shown [30, 74].

In parallel to the development of new and accurate characterization techniques, a conspicuous amount of effort was devoted to the fabrication of novel glasses for poling. As the characterization techniques became more and more sophisticated there was the need for glass scientists to have a simple and practical tool for evaluating the glass samples and have an immediate feedback for improving the glass composition. Bearing this idea in mind, in this thesis we proposed a variation of the MFT technique in which a sandwich structure formed by two identically poled samples stacked together with their nonlinear regions facing each other. The thickness of the nonlinearity is inferred from interference pattern between the SH light beams generated by the two nonlinear layers. The major advantage of such a technique is that it is non-destructive and can measure thicknesses of the depletion layer as small as 4 μm, with a resolution of 1 μm. The approximation of a square nonlinear profile is made and therefore this technique provides the same information as a classical MFT plus an etching measurement of the thickness of the nonlinear region. A beautiful technique was proposed by Ozcan et al. at Stanford, that makes use of the same sandwich structure, together with a cylindrical lens assisted MFT, to determine the nonlinear profile [40, 93]. The method they suggested is based on an inverse Fourier transform algorithm. Their technique was refined in subsequent publications [94, 95], also employing a Fineup algorithm [96] and applied to the characterization of thermally poled germano-silicate thin-films [44]. Very recently Tréanton and co-workers proposed to use a quartz plate, of known nonlinearity, instead of one of the poled samples in the stack so that the $\chi^{(2)}(z)$ spatial distribution could be determined by an interferometric method.

3.5 Poling of non-silica glass systems

According to the charge migration model, the second-order nonlinear optical susceptibility $\chi^{(2)}$ induced in thermally poled glass is related to the third-order nonlinear optical susceptibility $\chi^{(3)}$ by $\chi^{(2)} = 3\chi^{(3)}E_{dc}$ where E_{dc} is the frozen-in electrostatic field induced by charge migration. For a given glass $\chi^{(3)}$ is fixed and, since E_{dc} is limited by the dielectric breakdown strength of the glass, $\chi^{(2)}$ has an upper limit. High-index glasses, which possess higher $\chi^{(3)}$ than silica, are potentially attractive since $\chi^{(2)}$ increases in proportion to $\chi^{(3)}$, for a fixed value of E_{dc}. However, in order to obtain higher $\chi^{(2)}$ values than in silica from high-index glasses, a permanent electrostatic field of the same order of magnitude as in silica has to be built in the glass. When one moves from silica to a high-index glass, the enhancement of $\chi^{(3)}$ can be estimated from Miller's rule. In 'esu' units , the linear and third-order nonlinear optical susceptibilities $\chi^{(1)}$ and $\chi^{(3)}$ are expressed by:

$$\chi^{(1)} = \frac{n^2 - 1}{4\pi} \tag{3.11}$$

$$\chi^{(3)} = 10^{-10}\left(\chi^{(1)}\right)^4 \tag{3.12}$$

where n is the refractive index. The $\chi^{(3)}$ enhancement factor is therefore given by:

$$\frac{\chi^{(3)}}{\chi_s^{(3)}} = \left(\frac{n^2 - 1}{n_s^2 - 1}\right)^4 \tag{3.13}$$

where n and n_s are the refractive indexes of high-index glass and silica, respectively. Miller's rule predicts an enhancement of $\chi^{(3)}$ by one order of magnitude in a glass which has a refractive index equal to 1.7 and by two orders of magnitude in a glass which has a refractive index equal to 2.1. It should be noted that actual values of $\chi^{(3)}$ are generally higher than those predicted by Miller's rule [5]. Although the approach may appear straightforward, we anticipate issues as we move from silica to other glass systems. First, it could be more difficult to create and to freeze a space charge in the glass. Second, the dielectric breakdown strength of the glass could be lower than in silica. For the poling process to be efficient, an electrostatic field of sufficiently high strength must be frozen-in the high-index glass such that the benefit of a high intrinsic $\chi^{(3)}$ is not lost.

Hereafter is a review on poling of high-index glasses. Possible candidates are zinc- or tungsten-doped tellurite glasses, titanium-doped silicate glasses, lead- or bismuth-doped silicate glasses.

Tellurite Glasses

TeO_2-based glasses have one of the largest $\chi^{(3)}$ among homogeneous glasses [97]. Re-

fractive index values (at 633 nm) range from 2.0 to 2.3 and $\chi^{(2)}$ values range from 0.3 to 3×10^{-12} esu [97]. For comparison, $\chi^{(2)} = 0.028 \times 10^{-12}$ esu in SiO_2 [97]. A peculiar property of tellurite glass is their low glass transition temperature, ranging from 250 °C for $30NaO_{1/2}{\cdot}70TeO_2$ glass [9] to 350 °C for $10MgO \cdot 20ZnO{\cdot}\ 70TeO_2$ glass [98]. Because the glass transition temperature is very close to usual poling temperatures, the latter must be optimized for each glass composition.

In thermally poled $ZnO{\cdot}TeO_2$ glass, an increase of ZnO doping concentration enhances SHG [99]. It is believed that non centro-symmetric structural units of tellurite glass are oriented in the direction of the applied electric field during poling. Orientation of these units takes place more easily in ZnO-rich glass because the glass network is softer in this case. In thermally poled $15BaO{\cdot}85TeO_2$ glass, however, no SHG was observed, presumably because the applied electric field mainly causes the electronic polarisation of Ba^{2+} ions, which readily disappears when the electric field is removed after poling [99]. In thermally poled $B_2O_3{\cdot}TeO_2$ and $MgO{\cdot}ZnO{\cdot}TeO_2$ glasses, rather small values of the nonlinearity ($\chi^{(2)} \sim 0.2$ pm/V) were reported [100]. Nonlinearity was larger in the latter glass system than in the former. In $MgO{\cdot}ZnO{\cdot}TeO_2$ glass system, the glass transition temperature (T_g) increases with replacement of ZnO by MgO. Maximum SHG intensity is higher and poling temperature, which corresponds to maximum SHG, is lower in the glass with lower T_g [98]. A similar correlation between optimal poling temperature and glass transition temperature is also found in $Na_2O{\cdot}ZnO{\cdot}TeO_2$ glasses [9]. At least, such a correlation suggests that the structural changes of glass network occurring near T_g affect the poling process. Heat treated (but not poled) $15K_2O{\cdot}15Nb_2O_5{\cdot}70TeO_2$ glass exhibits SHG that is comparable to that in thermally poled TeO_2-based glass [101]. The origin of SHG is thought to be closely related to the presence of slightly distorted cubic crystalline phase. In $15BaO{\cdot}15TiO_3{\cdot}70TeO_2$ glass, thermal poling was found to stabilise the tetragonal $BaTiO_3$ crystals which are precipitated at the glass surface, leading to a larger second-order nonlinearity [102]. In early studies on thermally poled $WO_3{\cdot}TeO_2$ glasses, rather small values of the nonlinearity ($\chi^{(2)} = 0.1 - 0.2$ pm/V) were obtained [99]. Recently, nonlinearity as high as $\chi^{(2)} = 2.1$ pm/V was achieved in $20WO_3{\cdot}80TeO_2$ glasses [8]. Nonlinear thickness was estimated to be 15 μm. Nonlinearity in this glass is attributed to migration of Na^+ from borosilicate glass plates, between which the sample is sandwiched, and to subsequent formation of a large electrostatic field beneath the anode which results in fairly large $\chi^{(2)}$ through interaction with the large $\chi^{(3)}$ of the glass [8]. Hence, application of higher voltage (limited to 3 kV in the experiment) should lead to even higher $\chi^{(2)}$. However, nonlinearity induced in this glass decays with relaxation time of $\sim$ 15 days at room temperature.

Titanium Silicate Glasses

In thermally poled TiO_2-doped silica glass, rather small values of the nonlinearity were reported ($\chi^{(2)} = 0.02$ pm/V) [103]. However, in this early experiment, dielectric breakdown prevented from applying dc voltage higher than 3 kV and temperature higher than

300 °C. SHG was attributed to the presence of TiO_2 in silica, assuming the formation of dipoles and their orientation in the direction of the applied electric field. More recently, ab-initio calculations were performed in order to estimate the first and second-order microscopic polarisabilities for titanium oxygen clusters in $TiO_2{\cdot}NaPO_3{\cdot}Na_2B_4O_7$ and $TiO_2{\cdot}K_2O{\cdot}SiO_2$ glasses [104]. Enhancement of the polarisabilities through formation of dimeric entities was demonstrated.

Lead Silicate Glasses
Lead silicate glasses have large third-order optical nonlinearity. In SF59 lead silicate glass (Pb $\sim$ 83 %wt) $\chi^{(3)}$ is equal to $6.2 \times 10^{-21}\,m^2/V^2$, which is about 30 times the value of pure silica glass ($2.0 \times 10^{-22}\,m^2/V^2$) [105].
By electron-beam irradiation poling, a value of $\chi^{(2)}$ equal to 0.7 pm/V was achieved in F_2 lead silicate glass (Pb $\sim$ 45 %wt.) [24]. The nonlinearity induced in lead silicate glass by this technique increases linearly with the lead concentration. Using the same poling technique, $\chi^{(2)}$ as high as 4 pm/V was obtained for ZF7 lead silicate glass (Pb $\sim$ 70.9 %wt) [106]. The accumulative effect of electron irradiation for inducing the nonlinearity appears limited by the breakdown threshold in the charged layer. Recently, SH intensity in thermally poled lead silicate glass was found to increase exponentially with an increase in lead concentration. A value of $\chi^{(2)}$ as high as 7 pm/V is inferred for ZF7 lead silicate glass [107].

3.6 Alternative poling methods

UV Poling
The method of direct UV poling, first realized by Fujiwara, consists of the irradiation of highly Ge-doped (15.7 %mol.) fused silica glass by short UV (193 nm) laser light in the presence of an applied electric field of $100 - 300$ kV/cm. Fujiwara reported the induction of a nonlinear second-order coefficient d as high as 3.4 pm/V [108]. In following publications 5.2 pm/V were reported for pre-heated GeO_2-SiO_2 glass and 12.5 pm/V in GeO_2-SiO_2 sputtered thin-films[27]. The authors claim that orientation of GeE' dipoles together with the formation of micro-crystallites in the poled glass are likely to be the cause of such a high nonlinearities. Despite the following publications on this subject by the same group [26, 109, 110], there is growing scepticism about these results in scientific literature as they are not reproducible by independent research groups [111, 112]. Moreover, the results on poled fibres have not been reproduced at all after their first publication. The report by [112] of repeatable UV-poling in fibres with induction of linear electro-optic coefficient $r = 0.1$ pm/V is interesting. The fibre was a specially fabricated twin-hole germanosilicate fibre with a layer of boron deposited around the anodic hole to act as a trapping layer for the electrons generated during the UV irradiation.

CO_2 Laser-Assisted Poling

This poling method is a variation of thermal poling. The source of heat is provided here by a CO_2 laser beam. It was first introduced by [113], but it was then extensively used by [25, 112]. Compared to thermal poling it is claimed that a more efficient heat energy transfer to the fibre is achieved due to the localized action of the laser beam. This leads to a faster poling process (in the region of few seconds compared to tens of minutes in thermal poling [112]). Furthermore, as the laser beam can be focused in a small area, it is possible to achieve periodic poling in fibre, without the need of periodic electrodes defined by photolithography. CO_2 laser assisted poling could greatly simplify the production of periodically poled fibres and in principle devices longer than 10 cm and up to about 1 m are feasible. In [114] an irradiance of $54 \pm 2\,\mathrm{W/cm^2}$ was judged as the optimum for poling of optical fibre. Such a value raises the temperature of the core to 280 °C. From the point of view of a periodically poled fibre device, it is interesting to note that 2.2 s of exposure (beam size $l = 3\,\mathrm{mm}$, scanning speed $v = 1.36\,\mathrm{mm/s}$) were required to bring the induced linear electro-optic coefficient to the maximum value of 0.2 pm/V. A periodic poled device, having QPM period of $\sim 40\,\mu$m, could be fabricated by focusing the laser beam down to about $20\,\mu$m in size, attenuated in order to maintain the same irradiance, and exposed for 2.2 s. The procedure has to be repeated every $40\,\mu$m for the whole device length. It becomes clear then that the fabrication of a 20 cm long periodic poled device would require about 3 hours to be completed. Such a long time imposes very strict requirements about the stability of the laser source and on the fibre positioning. Fascinating is the possibility to periodically reverse the nonlinearity by periodically reversing the sign of the applied field while scanning the laser beam. This would make devices made by this method four times as efficient, for the same length, as devices made by periodic thermal poling.

electron-beam Poling

The electron-beam poling consists of exposing the glass surface to a focused electron beam [24].As a result of electron implantation, a space-charge electro-static field is created in a thin region beneath the surface. The electron-beam poling is very efficient for lead-silicate glasses. Interestingly, it should be noted that electron-beam irradiation is able to erase the nonlinearity induced by thermal poling in silica, thus providing a way for the fabrication of $\chi^{(2)}$-gratings for quasi-phase matching [115].

3.7 Electro-Optic Modulators and Switches

The discovery of thermal poling in 1991 opened up the possibility of electro-optic modulation and frequency conversion in glass fibres and waveguides. Together with fundamental studies aimed at enhancing the value of the second-order nonlinearity, the first working devices were demonstrated. Since the nonlinearity is located a few microns below the anodic surface, the challenge from the technological point of view was the fabrication of fibres and waveguides having the core close to that surface. In 1989,

even before the discovery of thermal poling, Li and Payne induced a permanent linear electro-optic coefficient in a fused silica fibre subjected to strong electric field by means of internal electrodes [116]. The fibre had two holes running parallel to the core that were filled with gallium liquid electrodes at room temperature. A 65 cm long fibre modulator was fabricated by exposing the core to 4000 kV/cm. The induced linear electro-optic coefficient was $r \simeq 2\chi^{(2)}/n^4 = 2 \times 10^{-3}$ pm/V. In 1994 a D-shape fibre, where the core is placed close to the flat side of the fibre, was used for the first time and a $\chi^{(2)}$ as large as 0.2 pm/V was obtained after poling [117]. The reproducibility of the results was greatly improved by poling in vacuum in order to circumvent problems caused by partial electric breakdown in air during poling [118]. Also in 1994, the research group in Albuquerque, fabricated a poled fibre electro-optic modulator using a D-shape fibre [119]. HF etching of the fibre allows the reduction of the thickness of the cladding above the core to only 6 μm. The reported linear electro-optic coefficient was 0.05 pm/V. The major issue while poling D-shape fibre is that breakdown may occur between the flat electrode and the ground. Further improvement of the packaging using polyimide as insulator resulted in $r = 0.3$ pm/V and the half-way driving voltage of the fibre modulator was 75 V at 633 nm and for a 12 cm long device. A planar device was first obtained in 1996 by the NTT Opto-electronics laboratories. 2x2 electro-optic switching was demonstrated in an integrated Mach-Zehnder interferometer constructed with thermally poled GeO_2-doped silica based channel waveguides on a Si substrate. The switching voltage was 1700 V in the 1.55 μm wavelength region for a 36 cm long device [120]. Fascinating is also the demonstration of poling of holey fibres by Faccio and co-workers [121]. A maximum linear electro-optic coefficient of $\simeq 0.02$ pm/V was obtained after 40 minutes poling at 4 kV at 280 °C. This work demonstrates that the air-holes structure of micro-structured fibres is compatible with poling. More than for electro-optic modulators, this work opens new possibilities for efficient and broadband frequency conversion owing to the endlessly single mode operation and tight mode confinement of micro-structured fibres [122]. A conspicuous amount of work on the fabrication of electro-optic modulators has been carried out by the research group at Sydney University. A powerful tool they have been using is a Mach-Zehnder interferometer employed for a real-time monitoring of the evolution of the E-O coefficient during poling of twin-hole fibres [123, 124]. The experimental set-up enabled the measurement of both amplitude and direction of the frozen-in field E_{dc} and also of the $\chi^{(3)}$ in poled and unpoled fibres [123]. On the basis of the experimental observations, including a different behavior for positive and negative poling [125] and direct visualization of the depletion region in fibres [114], they proposed a model for the thermal poling in fibre based on the competition between three fields, the applied field, a shielding field created by the diffusion of charges which opposes to the applied field, and an ionizing field originated by charge emission and glass ionization as the depletion region builds up [114, 126]. The depletion region was found to be formed all around the hole containing the anode electrode. A novel design of twin-hole fibre, having a ring of either boron or erbium to act as a trap, or donor, of electrons respectively, was

fabricated in order to improve the poling performance [112]. Indeed the B-ring doped twin-hole fibre exhibited longer stability, in the range of few years [127] compared to hundreds of days in the undoped fibres used by them [128]. It should be mentioned that several groups observed an enhancement of $\chi^{(3)}$ in the fibre after thermal poling [127]. This enhancement was measured to be $\simeq 2$ by the group in Sydney and was found to be 1.98 by Garcia et al. after poling of a channel waveguide [13]. A tentative explanation was given by Kashyap [129] but overall the enhancement of $\chi^{(3)}$ is still questionable and not all groups could observe it [14]. A very promising technology has been developed by Fokine et al. [130]. The holes of a twin-hole fibre have been filled with a AuSn alloy in the liquid state at 300°C under pressure. Subsequent poling has been carried out at 250°C with the alloy in the solid state. A wide wedge shaped nonlinear region was revealed around the anodic hole, by etching, in agreement with simulations considering the air surrounding the fibre to be at the same potential as the cathode electrode [14]. From the point of view of an electro-optic modulator or 2×2 switch, the good contact between the electrodes and the walls of the holes ensured by this technology, makes it possible to use the electrodes in order to apply the driving field. An half-way voltage, V_π, of 1.37 kV at 1550 nm for a 20 cm device was demonstrated. Although filling the holes with alloys enables over a meter long electrodes, in this first experiment, the total length of the devices was limited by the loss caused by the interaction of the light modes with the metallic interfaces. Improvements in the fibre design are expected to lead towards long > 1 m electro-optic modulators with a switching voltage as low as 50 V [14].

3.8 Quasi-Phase Matched Frequency Converters

In 1989 R. Kashyap demonstrated for the first time quasi-phase matched frequency conversion in optical fibres by electric field induced second-harmonic generation [131]. The electric field was not frozen in the glass, rather it was applied externally with interdigited electrodes. Four years later, again using interdigitated electrodes he thermally poled a bulk fused silica plate and demonstrated quasi-phase matching. [72]. In 1995 at the Optoelectronics Research Centre, the first demonstration of quasi-phase matching in a thermally poled optical fibre was reported. Frequency doubling to the blue was obtained in a D-shape fibre [132]. The breakthrough was made possible by the vacuum poling technique that improved the uniformity and reproducibility of the fibre poling [118]. A maximum of 400 pW of blue light for a pump power of 100 mW was produced. The low efficiency was attributed to a combination of imperfections (slight chirping and randomness in the length of the individual poled sections) and of inexact overlap between the nonlinear layer and the core. Later it was also found by the same group that poling in vacuum produces a value of the nonlinearity which is approximately three times lower than for poling in air [82]. In 1997 Pruneri et al. achieved QPM SHG generation into the blue by frequency doubling picosecond pulses [19]. The

average conversion efficiency, defined as the ratio of the second harmonic (SH) power over the pump power, was $\simeq 0.22\%$ in a 1.8 cm long periodically poled D-shape fibre enabling 76 μW of SH blue light power to be produced with a 35 mW average input power (200 W peak power). In contrast to the previous work, in this case the comb electrode was patterned by photolithography directly on the flat surface of the D-shape fibre, allowing better contact. Using the same technology Pruneri et al. demonstrated for the first time frequency doubling of femtosecond pulses [20]. A 1.2% conversion efficiency was obtained in a 4 cm long periodically poled fibre and was found to be limited by competing third-order nonlinear processes [133]. In 1999, the same group reported frequency doubling of a nanosecond Q-switched fibre based source. Compared to the picosecond and femtosecond pulses, nanosecond pulses enable longer interaction lengths before walk-off takes place. Up to 7.5 cm long $\chi^{(2)}$-gratings were fabricated by thermal poling in vacuum and periodic electrodes defined by standard photolithography on the flat surface of a D-shape fibre. Average conversion efficiency of 21% was demonstrated for pump peak powers as high as 4 kW corresponding to a normalized conversion efficiency of 5×10^{-3} %/W [12]. The conversion efficiencies obtained in this work aroused considerable excitement as they are on the same level as can be obtained with widely used nonlinear crystals for frequency conversion such as LiB_3O_5 and KTP. Following this work Bonfrate and co-workers demonstrated for the first time parametric fluorescence in a quasi-phase matched optical fibre [134]. Photon-pairs were produced at a rate of $\simeq$ 150 MHz, which in principle is large enough to demonstrate a quantum-key distribution system at 1550 nm with poled fibres.

Although successful, periodic poling of D-shape fibres in vacuum, has some drawbacks which prevent scalability towards higher conversion efficiency. The photolithographic process limits the device length to about 10 cm. Also the quality of the $\chi^{(2)}$-grating might be an issue as the fringe field produced by the comb-electrode might vary the duty cycle and reduce the contrast of the QPM structure. Furthermore, as it was mentioned earlier, poling in vacuum results in about a three times smaller value of the nonlinearity compared to poling in air [12]. For this reason it was necessary to look into alternative technologies which could be compatible to poling in air and also scalable to longer lengths. One possibility that has been investigated in order to overcome the limitations imposed by the fabrication of periodic comb electrodes is the periodic erasure of a uniform nonlinearity. Since the work on photoinduced second-harmonic generation in fibres it has been known that the self-organized $\chi^{(2)}$-grating could be erased by exposure to ultraviolet light excitation [135, 136]. In principle, since long uniformly poled fibres with internal electrodes can be fabricated [130], the uniformly poled fibre could be exposed through an amplitude mask and even translated relative to it in order to achieve long $\chi^{(2)}$-gratings. Several groups have reported erasure by UV light in thermally poled silica glass plates [80, 137, 138]. Montant and co-workers at Bordeaux University demonstrated erasure of the nonlinearity by two-photon absorbtion in thermally poled borophosphate bulk glasses exposed to femtosecond pulses at 800 nm [139, 140]. The

same group also demonstrated that the erasure of the nonlinearity could be spatially controlled by appropriately controlling the intensity distribution of the erasing beam [141]. The first demonstration of UV erasure for quasi-phase matched second-harmonic generation in a poled optical fibres was in 2000 by Bonfrate et al. [22]. For a 4 kW peak power of the fundamental radiation, an average conversion efficiency of 6% was reported after exposure of a uniformly poled D-shape fibre through a 6 cm long amplitude mask. The UV light excitation was provided by a non-collimated mercury-xenon lamp. This result was very encouraging as, although not completely optimized, devices fabricated by periodic UV erasure had performances comparable with the best fibres fabricated by periodic comb electrodes [12]. Nonetheless, the possibility of scaling to longer lengths was not exploited in this case. In this thesis quasi-phase matching second-harmonic generation in long ($> 10\,cm$) periodically poled silica fibres is reported [16]. All fibre frequency doubling of a fibre laser operating at 1554.8 nm produced 3.6 mW of red light in the fundamental mode. The average conversion efficiency was 2.4% achieved in a 11.5 cm long device with a pump peak power of only 108 W compared to the 4 kW used in the previous works. The corresponding conversion efficiency, normalized for the pump power, is 2.2×10^{-2} %/W and is the highest ever reported for poled fibres. The fabrication of long devices has been made possible by the use of a twin-hole fibre with internal wire electrodes in order to produce a long uniformly poled region and by a new technology for the $\chi^{(2)}$-grating fabrication: the continuous periodic UV erasure. A UV beam is flashed intermittently and translated along the poled fibre in order to produce the desired modulation of the nonlinearity, without the need for an amplitude mask. The continuous periodic UV erasure derives from the continuous Bragg-grating writing technology which enabled up to 1 m long Bragg gratings to be fabricated [142, 143]. A further extension of the potentialities offered by periodically poled fibre devices is the demonstration, by Canagasabey and co-workers of more than 30 nm tuneability of the QPM wavelength [144].

Chapter 4

Improvement of the Maker's fringe technique

Nowadays, efforts are focused on the search for novel glass systems and optimum poling conditions to obtain the highest SON [145, 146], even though a reliable determination of the value of $\chi^{(2)}$ is still an issue. Typically, the Maker's fringe technique (MFT), first developed by Maker et al. in 1962 [147], is used to evaluate the $\chi^{(2)}$ of nonlinear materials. In this technique, a laser beam is focused onto the nonlinear sample of length L and, while varying the angle of incidence, the beam is used as a pump to generate second harmonic light. Due to the dispersion of the glass the SH and the driving polarization waves propagate with different velocities and their phase relationship at the output of the nonlinear medium depends on the actual path travelled inside. Therefore, while rotating the sample and recording the power at the second-harmonic frequency, an oscillating behavior results from the interference between the polarization wave and the SH-wave. The spacing between two adjacent peaks of the second-harmonic power carries the information about the thickness of the nonlinear region. The critical point of the Maker's fringe technique for the measurement of $\chi^{(2)}$ is the determination of the thickness of the nonlinear region, which is not straightforward in thin nonlinear samples like, in most cases, in thermally poled glasses. In thin samples no fringes in the MFT pattern are present and unless an independent measurement of the thickness of the depletion layer is performed, the MFT *cannot* be used. Unfortunately, in the literature values of $\chi^{(2)}$ in poled glasses are reported where the thickness of the nonlinearity had only been estimated, making it difficult to compare results.

A detailed analysis of the theoretical background and principle of operation of the Maker's fringe technique is discussed in the following section. Care is taken in order to highlight the refinements that are necessary for the highest accuracy. The validation of the experimental procedure is the subject of sections 4.1.5 to 4.1.7. The limits of the Maker's fringe technique are discussed in Section 4.2 and a novel technique is pro-

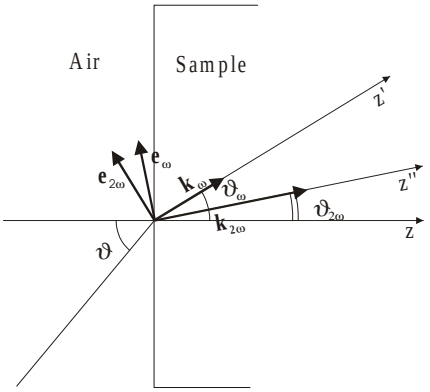

FIGURE 4.1: The incident and refracted rays at the fundamental and second harmonic frequencies near the boundary between a nonlinear medium and air.

posed for characterizing the second-order nonlinearity in thin samples and to overcome the limits of the MFT. The technique developed in this work was called *Stack Maker's Fringe Technique* (SMFT): it is based on the interference between SH light beams which are generated by two identically poled glasses pressed together in a stack. The SMFT was tested on a set of thermally poled silica plates.

4.1 Maker's fringe technique

In this section the same formalism as in chapter 2 is used. In addition, the presence of an interface between a linear and a nonlinear medium as well as the general case of non-normal incidence are considered here in order to adequately describe the Maker's fringe technique.

Due to the boundary conditions for second harmonic generation at the interface between a linear and a nonlinear medium, i.e. from the continuity of the magnetic and electric field tangential components, the pump and second harmonic waves propagate in a slightly different direction (see Fig.4.1) [148]:

$$\vartheta_\omega = \arcsin\left(\frac{\sin\vartheta}{n_\omega}\right) \tag{4.1}$$

$$\vartheta_{2\omega} = \arcsin\left(\frac{\sin\vartheta}{n_{2\omega}}\right). \tag{4.2}$$

From hereafter the z axis will be defined as the axis normal to the sample surface. Hence, the pump travels with a k-vector $k_\omega = (\omega/c)n_\omega$ along a z' axis. Similarly the second harmonic travels with a k-vector $k_{2\omega} = (2\omega/c)n_{2\omega}$ along a z'' axis (see Fig. 4.1).

4.1.1 Derivation of the second harmonic intensity

The vector wave equation for both pump and second-harmonic electromagnetic fields is derived from eq. 2.18. The treatment follows the same line as in chapter 2 but it has been generalized in order to consider the two different directions of propagation of pump and SH.

$$\begin{aligned}\frac{\partial \mathbf{A}_\omega}{\partial z'} &= i\frac{\mu_0\omega^2}{2k_\omega}\mathbf{P}_\omega^{\mathrm{NL}}e^{-ik_\omega z'} \\ \frac{\partial \mathbf{A}_{2\omega}}{\partial z''} &= i\frac{\mu_0(2\omega)^2}{2k_{2\omega}}\mathbf{P}_{2\omega}^{\mathrm{NL}}e^{-ik_{2\omega} z''}\end{aligned} \tag{4.3}$$

Like before, we can write

$$\begin{aligned}\frac{\partial A_\omega}{\partial z'} &= i\frac{\mu_0\omega^2}{2k_\omega}\hat{\mathbf{e}}_\omega\cdot\mathbf{P}_\omega^{\mathrm{NL}}e^{-ik_\omega z'} \\ \frac{\partial A_{2\omega}}{\partial z''} &= i\frac{\mu_0(2\omega)^2}{2k_{2\omega}}\hat{\mathbf{e}}_{2\omega}\cdot\mathbf{P}_{2\omega}^{\mathrm{NL}}e^{-ik_{2\omega} z''}\end{aligned} \tag{4.4}$$

by defining $\mathbf{A}_\omega = \hat{\mathbf{e}}_\omega A_\omega$, and making the scalar product $\hat{\mathbf{e}}\cdot$ at both sides of equations 4.3. The explicit form of the second order nonlinear polarization components $\mathbf{P}^{(2)}$ defined in eqs. (2.13) is given by:

$$\begin{aligned}\mathbf{P}_\omega^{(2)} &= \varepsilon_0\boldsymbol{\chi}^{(2)}|\hat{\mathbf{e}}_{2\omega}\hat{\mathbf{e}}_\omega A_{2\omega}A_\omega^* e^{i(k_{2\omega}z''-k_\omega z')} \\ &= \varepsilon_0\boldsymbol{\chi}^{(2)}|\hat{\mathbf{e}}_{2\omega}\hat{\mathbf{e}}_\omega A_{2\omega}A_\omega^* e^{i(k_{2\omega}\cos(\vartheta_{2\omega}-\vartheta_\omega)z'-k_\omega z')}\end{aligned} \tag{4.5a}$$

$$\begin{aligned}\mathbf{P}_{2\omega}^{(2)} &= \varepsilon_0\frac{1}{2}\boldsymbol{\chi}^{(2)}|\hat{\mathbf{e}}_\omega\hat{\mathbf{e}}_\omega A_\omega A_\omega e^{2ik_\omega z'} \\ &= \varepsilon_0\frac{1}{2}\boldsymbol{\chi}^{(2)}|\hat{\mathbf{e}}_\omega\hat{\mathbf{e}}_\omega A_\omega^2 e^{2ik_\omega\cos(\vartheta_{2\omega}-\vartheta_\omega)z''}\end{aligned} \tag{4.5b}$$

Substitution of eqs. (4.5a) into eqs. (4.4) gives the evolution of the second harmonic electro-magnetic field:

$$\frac{\partial A_{2\omega}}{\partial z''} = i\frac{(2\omega)^2}{2k_{2\omega}c^2} d_{\text{eff}}(z'')|A_\omega|^2 e^{-i\Delta k'' z''} \tag{4.6}$$

$\Delta k''$ being the projection of the wave-vector mismatch $\boldsymbol{\Delta k} = \mathbf{k_{2\omega}} - 2\mathbf{k}_\omega$ along the second harmonic direction (i.e. the z'' axis):

$$\begin{aligned} \Delta k'' &= k_{2\omega} - 2k_\omega \cos(\vartheta_{2\omega} - \vartheta_\omega) \\ &= \frac{4\pi}{\lambda}\left(n_{2\omega} - n_\omega \cos(\vartheta_{2\omega} - \vartheta_\omega)\right) . \end{aligned} \tag{4.7}$$

The expression defining d_{eff} is the same as in eq. (2.23). The second harmonic field, after it propagates across the full length of the nonlinear material, is obtained through integration of eq. (2.22) with the condition $A_{2\omega}(z = 0) = 0$ and the hypothesis of low conversion efficiency $A_\omega(z) = \text{const}$. If L is the thickness of the nonlinear slab, the actual path travelled by the light inside the sample varies with the angle of incidence and it is given by $L/\cos\vartheta_{2\omega}$:

$$A_{2\omega}(L) = i\frac{\omega}{n_{2\omega}c}|A_\omega|^2 \int_0^{\frac{L}{\cos\vartheta_{2\omega}}} d_{\text{eff}}(z'')e^{-i\Delta k'' z''} dz'' \tag{4.8}$$

The intensity of the SH is then obtained by squaring eq. (4.8) bearing in mind that

$$I_{2\omega} = \frac{1}{2}\varepsilon_0 c n_{2\omega}|A_{2\omega}|^2. \tag{4.9}$$

Finally it follows:

$$I_{2\omega}(L) = \frac{2\omega^2}{\varepsilon_0 c^3 n_{2\omega} n_\omega^2} I_\omega^2 \left| \int_0^{\frac{L}{\cos\vartheta_{2\omega}}} d_{\text{eff}}(z'')e^{-i\Delta k'' z''} dz'' \right|^2 \tag{4.10}$$

4.1.2 Measurement of the second-order nonlinearity

In the previous section the expression for the second-harmonic intensity was derived (eq. 4.10). The aim of this section is to give all the necessary refinements in order to

apply it to practical situations [149]. In particular the losses at the air-sample and sample-air interfaces that are due to reflections must be considered.

The main limit of eq. (4.10), when trying to apply it to Maker's fringe measurements, is that its validity is limited to inside the material whereas, experimentally, the only measurable quantities are the powers of the pump and SH beams outside the nonlinear medium. The transmittance coefficients relating the external powers of the pump and of the second harmonic, $\mathcal{P}^{\omega}_{\text{ext}}$ and $\mathcal{P}^{2\omega}_{\text{ext}}$ respectively, with the internal powers,$\mathcal{P}^{\omega}_{\text{int}}$ and $\mathcal{P}^{2\omega}_{\text{int}}$, have to be included in the final equation. The following discussion will be restricted to the case of polarization parallel to the plane of incidence, i.e. the plane containing the normal to the surface and the beam itself (p-pol. case).
At the **air-sample interface** power is removed from the pump by a factor depending on the transmittance (T^{ω}) of the material, defined as the ratio between the transmitted and the incident power:

$$T^{\omega} \equiv \frac{\mathcal{P}^{\omega}_{\text{int}}}{\mathcal{P}^{\omega}_{\text{ext}}} \tag{4.11}$$

T^{ω}, in turn, depends on the index of refraction, on the direction of the polarization of the light and on the angle of incidence. In the case of polarization parallel to the plane of incidence, it follows [150]:

$$T^{\omega}_{\text{p-pol}}(\vartheta) = 1 - \left(\frac{n_{\omega}\cos\vartheta - \cos\vartheta_{\omega}}{\cos\vartheta_{\omega} + n_{\omega}\cos\vartheta}\right)^2 \tag{4.12}$$

At the **sample-air interface** the second harmonic beam is refracted and the same consideration as before can be applied. Due to partial reflection the power that actually comes out from the nonlinear medium is reduced by the transmittance factor $T^{2\omega}$ expressed by the ratio

$$T^{2\omega} \equiv \frac{\mathcal{P}^{2\omega}_{\text{ext}}}{\mathcal{P}^{2\omega}_{\text{int}}} \tag{4.13}$$

Noting that from Snell's law and from eq.(4.2), the exit angle of the second harmonic beam is equal to the incidence angle of the pump ϑ, the transmission coefficient for p-pol can be written as [150]:

$$T^{2\omega}_{\text{p-pol}}(\vartheta) = 1 - \left(\frac{\cos\vartheta_{2\omega} - n_{2\omega}\cos\vartheta}{n_{2\omega}\cos\vartheta + \cos\vartheta_{2\omega}}\right)^2 \tag{4.14}$$

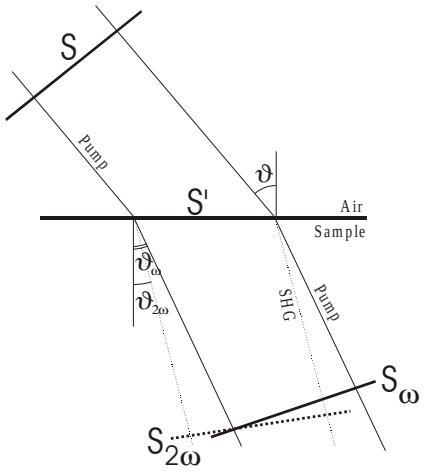

FIGURE 4.2: Cross sectional area of the pump and second harmonic beams. Note how the cross section changes due to the refraction at the air sample interface.

Moreover while considering the power per unit area we must take into account that the cross section of the beam inside the material is different from that of the beam propagating outside due to the refraction. This situation is depicted in Fig. (4.2) and with the aid of the above definitions:

$$\begin{aligned} \mathcal{P}^{\omega}_{\rm int} &= I^{\omega}_{\rm int} S_{\omega} \\ \mathcal{P}^{2\omega}_{\rm int} &= I^{2\omega}_{\rm int} S_{2\omega} \end{aligned} \tag{4.15}$$

where

$$\begin{aligned} S_{\ \omega} &= S' \cos\vartheta_{\omega} \ = S\ \frac{\cos\vartheta_{\omega}}{\cos\vartheta} \\ S_{2\omega} &= S' \cos\vartheta_{2\omega} = S\ \frac{\cos\vartheta_{2\omega}}{\cos\vartheta} \end{aligned} \tag{4.16}$$

with S being the cross-sectional area of the pump beam and S' its projection on the sample (Figure 4.2). Combining eqs. (4.11,4.13,4.15,4.16) and substituting into eq. (4.10) it follows:

$$\eta_{\rm SHG} \equiv \frac{\mathcal{P}^{2\omega}_{\rm ext}}{\mathcal{P}^{\omega}_{\rm ext}} = \frac{1}{S}\frac{2\omega^2}{\varepsilon_0 c^3 n_{2\omega} n_{\omega}^2}\, a\, T \left| \int_0^{\frac{L}{\cos\vartheta_{2\omega}}} d_{\rm eff}(z'') e^{-i\Delta k'' z''} dz'' \right|^2 \mathcal{P}^{\omega}_{\rm ext} \tag{4.17}$$

where the beam correction factor a has been introduced

$$a \equiv \frac{\cos\vartheta_{2\omega}}{\cos\vartheta} \left(\frac{\cos\vartheta}{\cos\vartheta_{\omega}} \right)^2, \tag{4.18}$$

and the Fresnel transmission losses have been accounted for by the factor T

$$T = T^{2\omega}(T^{\omega})^2. \tag{4.19}$$

When $d_{\text{eff}}(z'')$ is uniform along z'' the integral can be analytically solved and the expression describing the output of a Maker's fringe measurement is obtained:

$$\eta_{\text{SHG}} \equiv \frac{\mathcal{P}^{2\omega}_{\text{ext}}}{\mathcal{P}^{\omega}_{\text{ext}}} = \frac{1}{S}\frac{2\omega^2}{\varepsilon_0 c^3 n_{2\omega} n_{\omega}^2} d_{\text{eff}}^2\, a\, T \frac{L^2}{(\cos\vartheta_{2\omega})^2}\ \text{sinc}^2\left(\frac{\Delta k'' L}{2\cos\vartheta_{2\omega}}\right)\mathcal{P}^{\omega}_{\text{ext}} \tag{4.20}$$

with $\Delta k''$ defined in eq. 4.7 as

$$\Delta k'' = \frac{4\pi}{\lambda}\left(n_{2\omega} - n_{\omega}\cos\left(\vartheta_{2\omega} - \vartheta_{\omega}\right)\right) \tag{4.21}$$

and d_{eff} defined in eq. 2.23:

$$d_{\text{eff}} \equiv \frac{1}{2}\left[\hat{\mathbf{e}}^{2\omega}\cdot\chi^{(2)}|\hat{\mathbf{e}}_{\omega}\hat{\mathbf{e}}_{\omega}\right]. \tag{4.22}$$

4.1.3 The case of poled glass

The Maker's fringe technique can be applied to all nonlinear materials and thin films. Hereafter the particular case of the measurement of the second-order nonlinearity in a poled glass is discussed.

The glass plates are rotated along an axis perpendicular to the plane of incidence to perform the MFT measurement (Fig. 4.3). The pump electric-field is p-polarized in order to be co-planar with the frozen-in field E_{dc}. The direction of E_{dc} defines the optical axis of the poled glass as well as the group symmetry the poled glass belongs to: (6mm or $C_{\infty\text{mm}}$). A straightforward picture of the principle of operation of the Maker's fringe technique arises if the second harmonic is considered to be always collinear with the pump (i.e. $\vartheta_{2\omega} \backsimeq \vartheta_{\omega}$). Such approximation is extremely useful: it gives an intuitive physical description and moreover it fails only for extremely high incident angles ϑ. The approximation is justified because, owing to the low dispersion of silica, the difference between the index of refraction at the two frequencies is typically very small: $\backsimeq 0.01$. As a result, the difference between the internal angle of propagation for the pump and the second harmonic $\vartheta_{\omega} - \vartheta_{2\omega}$, given by eqs. (4.1 and 4.2), is always smaller than 0.4°

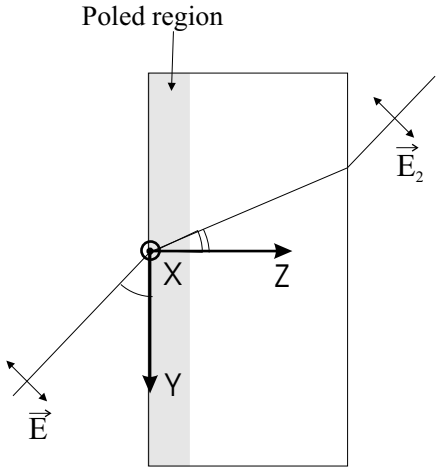

FIGURE 4.3: Geometry of a Maker's fringe experiment for a thermally poled glass. The pump beam is parallel to the plane of incidence (p-pol), which contains the Y and Z axis. The Z-axis is the optical axis of the poled glass (group symmetry $6mm$ or $C_{\infty mm}$). The sample is rotated along the X axis.

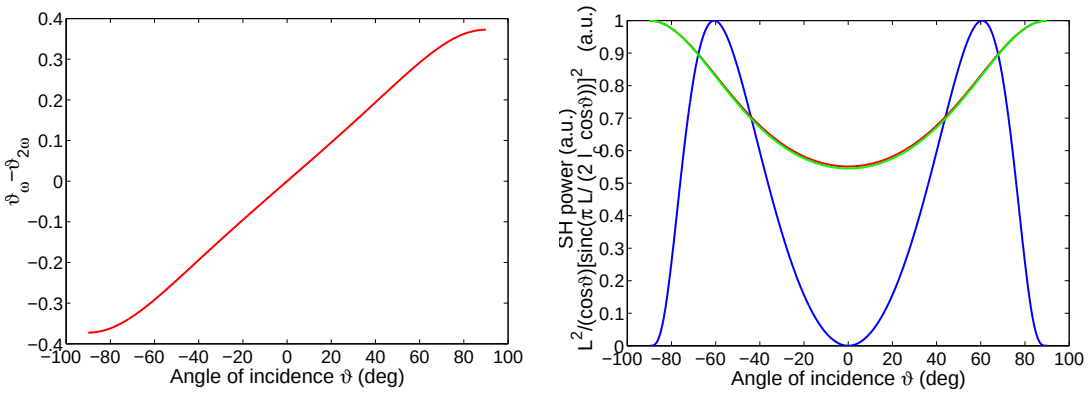

FIGURE 4.4: (left) Plot of the angular difference, $\vartheta_\omega - \vartheta_{2\omega}$, between pump and second harmonic internal propagation directions, as a function of the angle of incidence ϑ. (right) Theoretical computation of the oscillating function in the Maker Fringe formula (eq. (4.20)) assuming the case of a poled glass. (Red curve) $\vartheta_\omega \neq \vartheta_{2\omega}$, (Green curve) Approximated curve for $\vartheta_\omega = \vartheta_{2\omega}$. Note that the green and red curves are overlapped. The parameters used for the computation are the same as described in Fig. (4.5)

(Fig. (4.4(left))) It is worth noting that for normal incidence (i.e. $\vartheta = 0$) the difference is rigorously zero. Therefore for normal incidence the approximation $\vartheta_{2\omega} \backsimeq \vartheta_\omega$ is rigorously exact.

A numerical computation of the output of a Maker's fringe measurement of a poled glass with a uniform nonlinear depletion layer of 10 μm is shown in Fig. (4.5). On the same graph, the approximate curve is also shown. No appreciable difference can be observed.

Due to the dispersion, the polarization wave (bound wave) and the second harmonic wave (free wave) travel at different velocities inside the medium. As a result, the intensity $I_{2\omega}(L)$ of the second harmonic along the length of the sample is determined by the

interference between the two waves. Rotation of the sample alters the phase relationship between the bound and the free wave at the output of the sample because of the variation in the optical path length. There will be angles for which the two waves interfere constructively and angles for which there is complete destructive interference. The result of a Maker's fringe measurement is an oscillating curve obtained by recording the second harmonic power as a function of the incident angle.

The sinc^2 function, in eq. (4.20), accounts for this oscillating behavior. The angular separation between two adjacent peaks of the interference pattern corresponds to a difference in the optical path length equal to one coherence length. According to $l_c = \pi/\Delta k$, the argument of the sinc^2 function in eq. (4.20) can be expressed in term of the coherence length as: $\frac{\pi}{2}\frac{L}{l_c\cos(\vartheta_{2\omega})}$. When $(L/\cos\vartheta_{2\omega}) \ll l_c$ the sinc^2 tends to one and the second harmonic efficiency scales with the square of the interaction length $(L/\cos\vartheta_{2\omega})$. This condition holds for small angles of incidence and for thin nonlinear samples. The poled glass, having $l_c = 24\,\mu$m and a nonlinear region of $\backsimeq 10\,\mu$m is a typical case. The sinc^2 function, plotted in Fig. (4.4(right)), is close to one for all the incident angles.

$\Delta k''$ represents the projection of the vector $\mathbf{\Delta k} = \mathbf{k_{2\omega}} - 2\mathbf{k}_\omega$ along the second harmonic direction and it was defined in eq. (4.21): Owing to the low chromatic dispersion of silica glass, the dependence of $\Delta k''$ on the angle of incidence is limited. When $\vartheta_{2\omega}$ is assumed to be equal to ϑ_ω, $\Delta k''$ reduces to the well known modulus of the wave-vector mismatch

$$|\mathbf{\Delta k}| = \Delta k = \frac{4\pi}{\lambda}(n_{2\omega} - n_\omega). \tag{4.23}$$

As Δk can be considered constant for all ϑ, the major contribution to the oscillations in the MFT pattern is given by the variation of the path travelled by the light in the material: $L/\cos\vartheta_{2\omega}$. The wave-vector mismatch Δk accounts for the dispersion of the medium.

In Fig. (4.4(right)) the variation between the exact and the approximated oscillating function can be observed. The computed Maker's fringe curve is also shown.

The envelope of the MFT pattern (eq. 4.20) reflects the angular dependence of the Fresnel transmission losses T (eq. 4.19), the beam correction factor a (eq. 4.18) and of the effective nonlinear coefficient d_{eff} (eq. 4.22).

In the case of the poled glass with the $10\,\mu$m depletion layer depicted in Fig. (4.5), the path travelled by the light in the nonlinear region is smaller than the coherence length for all the incident angles. The maximum angle of refraction in silica is in fact $43.6°$, hence the maximum path travelled by the light in the nonlinear region is $10\,\mu$m $/\cos(43.6) = 13.8\,\mu\mathrm{m} < l_c = 24\,\mu$m. As long as no coherence length is reached in the Maker Fringe measurement, we would expect the second harmonic to grow with the

angle according to $(L/cos\vartheta_{2\omega})^2$. The maxima and the subsequent drops in Fig. (4.5) are due to the Fresnel transmission losses of the pump and of the second harmonic beam at the sample interfaces. The situation is clarified in Fig. (4.6) where the transmittance coefficient for the second harmonic and the Fresnel loss correction factor to the Maker Fringe formula ($T^{2\omega} \times (T^{\omega})^2$) are plotted versus the angle of incidence.

From symmetry considerations poled glass can be considered as belonging to the group symmetry $6mm$ or $C_{\infty mm}$. According to the Kleinman symmetry condition [5], the nonlinear tensor for a poled glass is given by:

$$\begin{pmatrix} 0 & 0 & 0 & 0 & d_{31} & 0 \\ 0 & 0 & 0 & d_{31} & 0 & 0 \\ d_{31} & d_{31} & d_{33} & 0 & 0 & 0 \end{pmatrix} \tag{4.24}$$

with $d_{33} = 3d_{31}$ and $d_{ij} = (1/2)\chi^{(2)}_{ij}$.

The angular dependence of d_{eff} is obtained from eq. 4.22:

$$d_{\text{eff}} = \frac{2}{3}\, d_{33}\,(\sin\vartheta_\omega \cos\vartheta_\omega \cos\vartheta_{2\omega}) + \frac{1}{3}\, d_{33}(\cos\vartheta_\omega)^2 \sin\vartheta_{2\omega} + d_{33}(\sin\vartheta_\omega)^2 \sin\vartheta_{2\omega} \tag{4.25}$$

The simpler case of $\vartheta_{2\omega} \backsimeq \vartheta_\omega$, hence,

$$d_{\text{eff}} \backsimeq d_{33} \sin\vartheta_\omega, \tag{4.26}$$

provides a better understanding of the role played by this parameter in the Maker's fringe output pattern. At normal incidence the nonlinear optical coefficient causes the second harmonic intensity to be zero. A plot of d^2_{eff} is shown in Fig. (4.7(left)).

Finally, the beam correction factor (eq. 4.18)versus the angle of incidence is plotted in Fig. (4.7(right)). The effect of this correction is merely a reshaping of the envelope.
The envelope of the MFT pattern is dominated at small ϑ by the contribution given by d_{eff} and at large ϑ by the Fresnel transmission losses.

4.1.4 The case of α-quartz

The absolute determination of the nonlinear coefficient d_{33} in poled glass with the MFT, requires the power of the fundamental beam and, in the case of a pulsed fundamental laser beam, the spatial and temporal distribution of the pulses, to be known with high

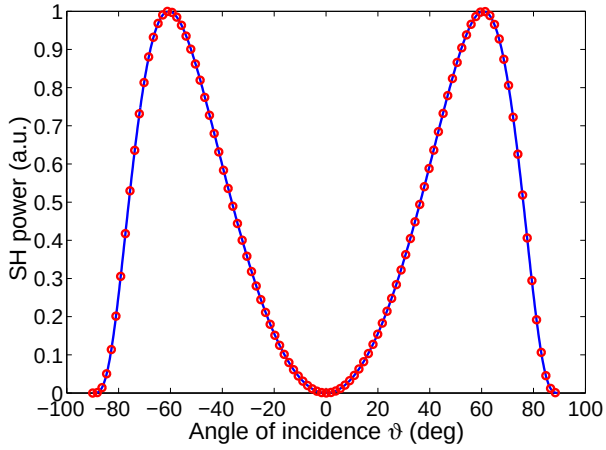

FIGURE 4.5: The output of a Maker's fringe measurement is evaluated numerically for the case of a poled glass with a nonlinear depletion layer of 10 μm. Both the exact equation (eq. (4.20)) (blue curve) and the approximate case for $\vartheta_{2\omega} \backsimeq \vartheta_{\omega}$ are plotted (circles). Other parameters used in the simulation are: $\lambda_{\text{pump}} = 1064\,\text{nm}$, $\lambda_{\text{shg}} = 532\,\text{nm}$, $n_{\omega} = 1.45$, $n_{2\omega} = 1.46$

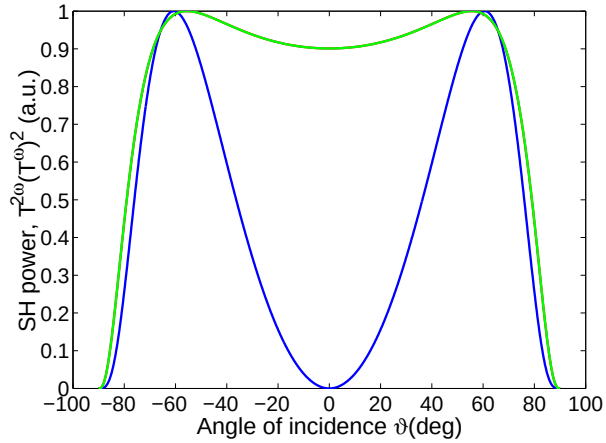

FIGURE 4.6: (Blue curve) Theoretical computation of the MFT pattern for a poled glass. (Red curve) Angular dependence of the Fresnel loss correction factor T (eq. 4.19). Note the sharp decrease in the transmitted power for angles larger than 60°. (Green curve) Approximated curve for $\vartheta_{\omega} = \vartheta_{2\omega}$. Note that the green and red curves are overlapped.

precision. Unfortunately this is not always easy especially when short pulses, typically hundreds of picosecond long pulses, are employed as the fundamental radiation. This issue can be circumvented by means of a comparative measurement with a material of known second-order nonlinearity, typically α-quartz is used for this purpose.

In this section a theoretical computation of a Maker's fringe pattern for α-quartz is presented. The case shown in figure (4.8) reflects the probing geometry used in the experiments, further described in this thesis. The crystal was an x-cut crystal. It had X-axis perpendicular to the optical window ($\alpha = 0°$) and the Z axis, which is the optical axis, parallel to the optical window. The Maker Fringe pattern for a 1.0186 mm thick quartz plate was derived according to eq. 4.20 (Fig. 4.9). The curve resulting from the

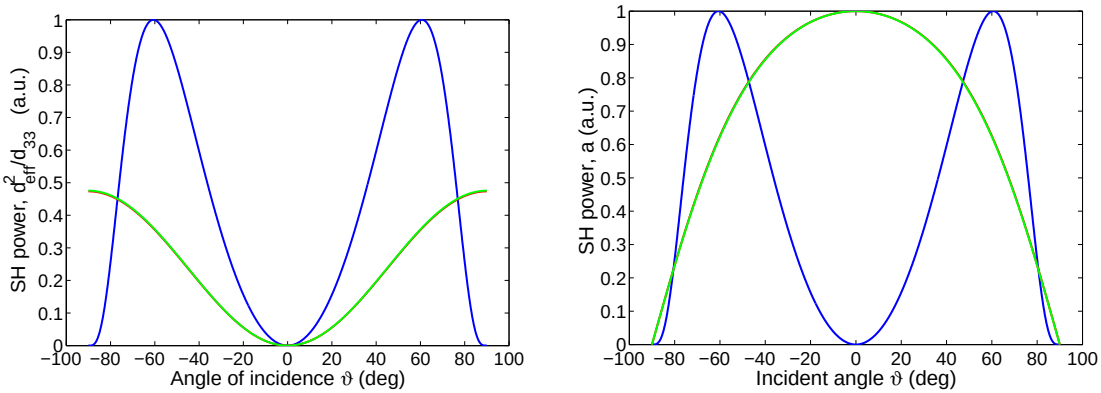

FIGURE 4.7: (Blue curve) Theoretical computation of the MFT pattern for a poled glass. (left) Theoretical computation of the squared effective nonlinear optical coefficient defined in eq. (4.22)) assuming the case of a poled glass (group symmetry 6mm ($C_{\infty mm}$)). (right) Plot of the correction factor a (eq. 4.18) accounting for the variation of the beam cross section due to refraction at the sample interfaces.

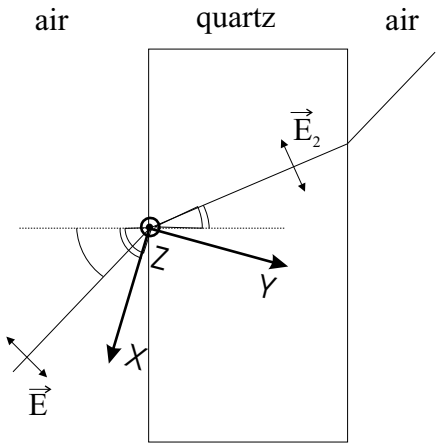

FIGURE 4.8: Geometry of a Maker Fringe experiment for the α-quartz plate used as a reference. The pump beam is parallel to the plane of incidence (p-pol), which contains the X and Y crystallographic axis. The Z-axis is the optical axis of the quartz (crystallographic class 32). The plate is rotated along the Z axis.

approximation introduced in the previous section ($\vartheta_\omega \simeq \vartheta_{2\omega}$) is shown on the same graph, too. Note that at large angles this approximation is no longer valid. A large number of fringes is observed due to the thickness of the quartz plate being much larger than the coherence length ($l_c = 20\,\mu$m). A plot of the oscillating part in eq. 4.20 is given in Fig. (4.10).

The contribution to the envelope given by the Fresnel transmission losses, $T = T^{2\omega}(T^{\omega})^2$, (see eq. (4.19)) and by the beam correction factor,a, (see eq. (4.18)), is shown in Fig. (4.12). The angular dependence of the nonlinear optical coefficient (d_{eff}) is calculated from the nonlinear tensor for a α-quartz crystal (crystallographic class 32):

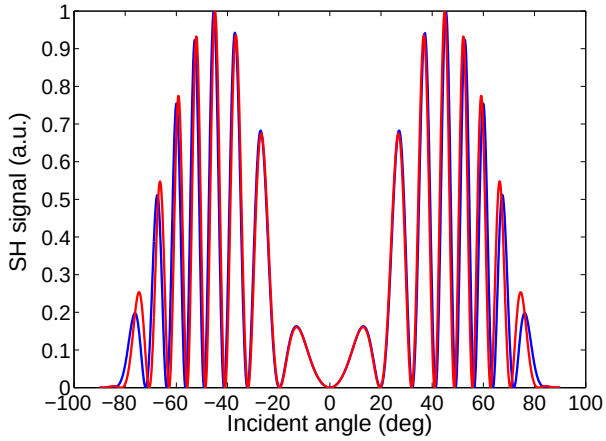

FIGURE 4.9: Theoretical computation of the MFT pattern of α-quartz. Numerical simulation of the output of a Maker Fringe measurement. A 1018.6 μm thick α-quartz plate is considered. Both (Blue curve) eq. (4.20)and (Red curve) the approximate case for $\vartheta_{2\omega} \backsimeq \vartheta_{\omega}$ are plotted. Other parameters used in the simulation are: $\lambda_{\text{pump}} = 1064\ nm$, $\lambda_{\text{shg}} = 532\ nm$. The indexes of refractions are evaluated from Sellmeier's eqs. $n_{\omega} = 1.5342$, $n_{2\omega} = 1.5469$

$$\begin{pmatrix} d_{11} & -d_{11} & 0 & d_{14} & 0 & 0 \\ 0 & 0 & 0 & 0 & -d_{14} & -d_{11} \\ 0 & 0 & 0 & 0 & 0 & 0 \end{pmatrix} \tag{4.27}$$

with $d_{ij} = (1/2)\chi^{(2)}_{ij}$. From eq. 4.22 follows:

$$d_{\text{eff}} = d_{11} \sin\left(\vartheta_{2\omega} + 2\vartheta_{\omega} - 3\alpha\right) \tag{4.28}$$

where α was defined in Fig. 4.8 and it is equal to zero for an x-cut crystal. The previous equation reduces to

$$d_{\text{eff}} = d_{11} \sin\left(3\left(\vartheta_{\omega} - \alpha\right)\right) \tag{4.29}$$

under the hypothesis of $\vartheta_{\omega} \simeq \vartheta_{2\omega}$ (Fig. 4.11)).

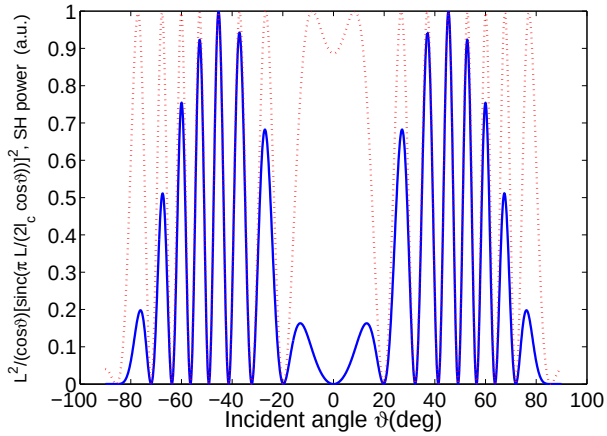

FIGURE 4.10: (Blue curve)Theoretical computation of the MFT pattern of α-quartz. (Red curve) Plot of the oscillating part in the Maker Fringe formula (eq. (4.20)) assuming the case of an α-quartz plate. The parameters in the simulation are the same as described in Fig. (4.9)

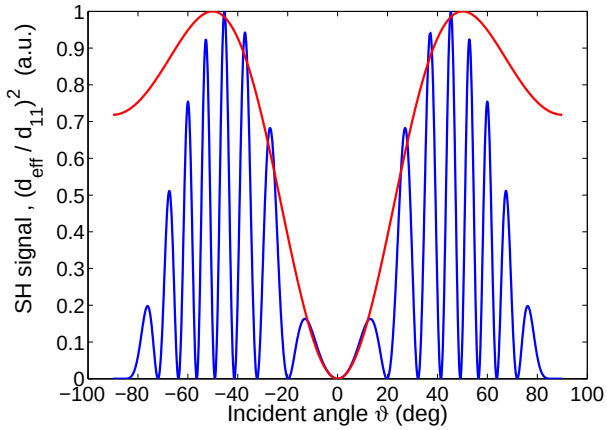

FIGURE 4.11: (Blue curve)Theoretical computation of the MFT pattern of α-quartz. (Red curve) Squared effective nonlinear optical coefficient defined in eq. (4.22)) assuming the case of an α-quartz plate (crystallographic class 32).

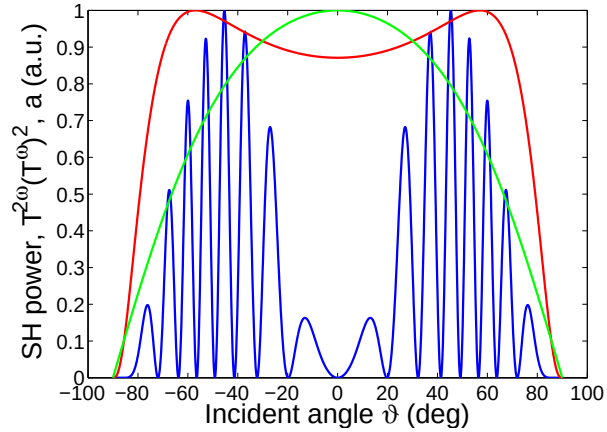

FIGURE 4.12: (Blue curve)Theoretical computation of the MFT pattern of α-quartz. Contribution to the envelope of the Maker fringe pattern due to (Red curve) the Fresnel transmission losses ($T = T^{2\omega}(T^{\omega})^2$ cfr. eq. 4.19) and to (Green curve) the beam correction factor (a cfr. eq. 4.18).

Work	**Reference**	$\mathbf{d_{11}(pm/V)}$	**Cited Source**
Henry, 1995	[151]	not specified	
Kameyama, 2001	[80]	0.31	Singh [a]
Kameyama, 1997	[152]	0.31	Singh [a]
Narazaki, 2002	[153]	0.34	not cited
Tanaka, 1996	[100]	0.34	not cited
Narazaki, 1998	[9]	0.34	not cited
Narazaki, 1999	[154]	0.34	not cited
Fujiwara, 1997	[108]	0.51	not cited
Hayashi, 1995	[155]	0.51	not cited
Khaled, 2001	[27]	0.51	not cited
Matsumoto, 2001	[156]	0.51	Levine [b]
Okada, 1992	[23]	0.51	Kurtz [c]
Okada, 1993	[157]	0.51	Kurtz [c]
Khaled, 2000	[158]	0.51	not cited
Ohama, 1999	[110]	0.51	Levine [b]
Tanaka, 1994	[99]	not specified	
Le Calvez, 1997	[77]	not specified	
Tanaka, 2000	[8]	not specified	

TABLE 4.1: Values of d_{11} reported in articles. Cited sources are (a) **S. Singh** in ref.[1],(b) **B.F. Levine** in ref.[2] and (c) **S.K. Kurtz, J. Jerphagnon and M.M. Choy** in ref.[3]

4.1.5 Calibration issues

Even though quartz is a well studied crystal, the values of the nonlinear coefficient d_{11} published in the literature far exceed the quoted experimental errors. The most cited works are 30 years old and the values of the nonlinearity for the d_{11} coefficient range from 0.31 [1] to 0.51 [3]. In a recent paper [66] the d_{11} of α-quartz is determined relative to d_{36} of ammonium dihydrogen phosphate (ADP) and found to be equal to $0.30 \pm 0.01\,\mathrm{pm/V}$ at 1064 nm. This is the value of d_{11} that is used in this thesis for the characterization of the SON in poled glass.

In table 4.1 results are reported on thermal poling of various glasses together with the cited values of d_{11} for quartz. It is clear how it is hard, and in some cases impossible, to make a comparison among published results.

4.1.6 Calibration measurements

For the content of this section it is convenient to write the expression for the second-harmonic power defined in eq. (4.20) as the product of two different contributions:

$$\mathcal{P}^{2\omega}_{g,q} = K'\, f(\vartheta, L_{g,q}, d^{g,q}_{\mathrm{eff}}, \ldots). \tag{4.30}$$

One of these contributions

$$K' = \frac{2\omega^2}{\varepsilon_0 c^3} \frac{\left(\mathcal{P}^{\omega}_{g,q}\right)^2}{S} \tag{4.31}$$

depending only on physical constants such as the pump frequency ω, pump power $\mathcal{P}^{\omega}$ and the pump beam area S and the other factor ($f(\vartheta, L_{g,q}, d^{g,q}_{\text{eff}})$) containing all the dependencies on the sample '(g,q)' (q: quartz or g: glass) characteristics.

In experiments, $\mathcal{P}^{2\omega}_{g,q}$ is not directly measured. What is actually measured is the signal from the photomultiplier tube which is a voltage ($V^{g,q}_{2\omega}$) proportional to the second-harmonic power:

$$V^{g,q}_{2\omega} = K\, f(\vartheta, L_{g,q}, d^{g,q}_{eff}, \ldots), \tag{4.32}$$

where K is simply a calibration factor determined by recording $V^{q}_{2\omega}$ for the quartz. It does not depend on the sample characteristics, therefore, it does not change when measuring, in the same conditions, the second-harmonic generated by a thermally poled glass. The second-order nonlinear optical susceptibility in the poled glass is eventually obtained by recording the Maker fringe pattern, $V^{g}_{2\omega}$, and fitting the data with eq. (4.32) and K given by the reference measurement with the quartz plate.

In principle, it is sufficient to record $P^{2\omega}_{q}$ at a given angle ϑ. However, the Maker fringe pattern is extremely sensitive to the sample thickness L_q. Therefore, in order to determine L^q with high accuracy, Maker's fringe patterns for the quartz plate were measured for a wide range of incident angles and the experimental data were fitted to eq. (4.30) with K, L^q and ϑ_0 as free parameters. The latter takes into account the error which may affect the reading of the incident angle (Figs. 4.13 and 4.14). Remarkably, the values of L^q obtained from two different sets of data are almost the same and are close to the value that was obtained by measuring the sample thickness with a micrometer (1016 μm-1018 μm).

4.1.7 Evaluation of d_{33} in a thermally poled silica glass

In this section, an example of the complete procedure used to determine the nonlinear optical coefficient d_{33} in thermally poled glasses, is given. A 1 mm thick silica plate (Herasil 1 by Heraeus) is thermally poled at 280 °C for 30 minutes with 4 kV applied in air. For the reference measurement, only a few points were recorded and the calibration factor was determined by fitting the data with K as the only parameter (see Fig. (4.15)). The thickness of the quartz sample L^q was taken as equal to 1018.5 μm from a full Maker fringe measurement (see section 4.1.6).

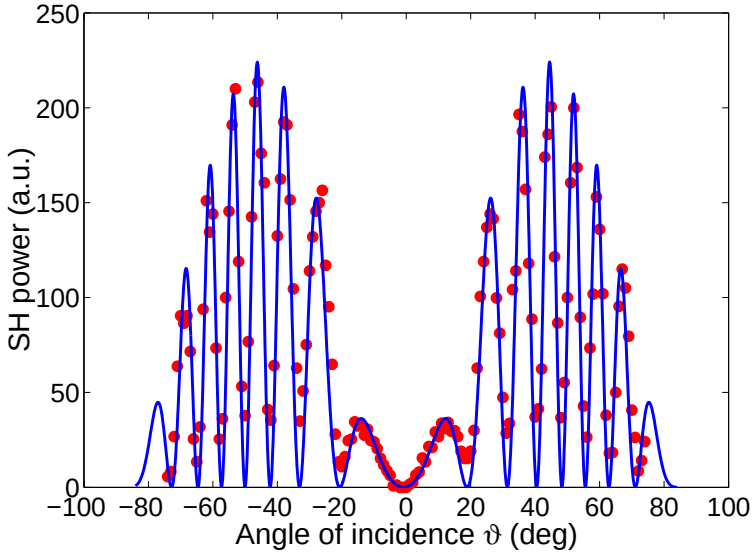

FIGURE 4.13: Full-range Maker fringe pattern recorded for a nominal 1-mm thick quartz sample (circles). The line is the best fit to eq. (4.30) with $K = 67.7$, $L^Q = 1018.6\,\mu$m, $\vartheta_0 = -0.9\,^\circ$. $d_{11} = 0.3\,$pm/V

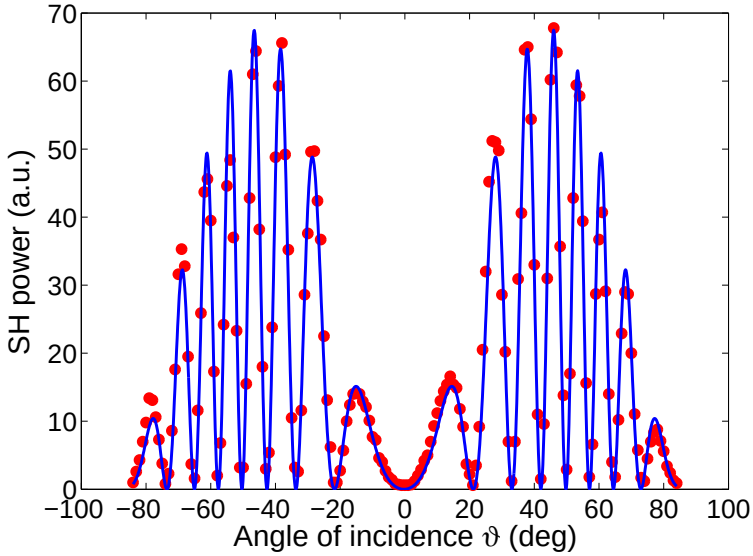

FIGURE 4.14: Full-range Maker fringe pattern recorded for a nominal 1-mm thick quartz sample (circles). The line is the best fit to eq. (4.30) with $K = 20.45$, $L^q = 1014.2\,\mu$m, $\vartheta_0 = 0.3\,^\circ$. $d_{11} = 0.3\,$pm/V

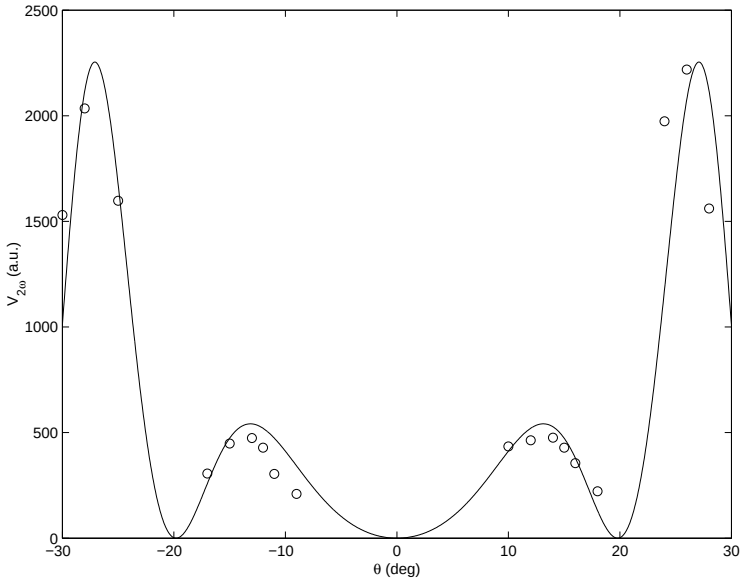

FIGURE 4.15: Calibration data obtained using quartz as a reference sample (circle). The second-harmonic signal was measured only for a limited set of angles. The line is a best fit. to eq. (4.30) with K=999.7. Fixed parameters are $L^g = 1018.5\,\mu$m, $\vartheta_0 = 0$ degree,$d_{11} = 0.3\,$pm/V

The second harmonic signal recorded for the poled glass is shown in Fig. 4.16. The SH power is proportional to the product $\left(\chi^{(2)}\,L\right)^2$. Hence, the ability to determine the value of $\chi^{(2)}$ requires the knowledge of L that is possible, in the MFT, only if the fundamental beam travels through the nonlinear medium for a length (L') at least equal to one coherence length ($l_c \sim 24\,\mu$m in silica). In principle it is possible to make L' longer than l_c by probing at large angles, but the total internal reflection (TIR) limits the minimum measurable thickness to $L = l_c \cos(\vartheta_{\rm TIR})$, that is about $18\,\mu$m for silica. In poled glasses the thickness of the nonlinear layer is usually smaller than this value ($\sim 10\,\mu$m) and therefore the MFT *cannot* be used.

This point is highlighted in Fig. 4.16 by fitting the experimental data to eq. (4.30) for a range of possible values of the nonlinear thickness. When L^g is below $10\,\mu$m all the fitting curves overlap and it is impossible to estimate the nonlinear thickness. For L^g between $10\,\mu$m and $18\,\mu$m there is a small difference in the position of the maximum, meaning that it should be theoretically possible to discriminate among them. On the other hand the difference is so small that it is hard to appreciate due to experimental errors. Practically, the MFT should not be used for L_g below $18\,\mu$m. The knowledge of the nonlinear thickness is crucial since different values of L^g lead to different values of d_{33}. Since the experimental data appears to indicate that the nonlinear region is smaller than $18\,\mu$m, the nonlinear thickness must be obtained independently. L^g was measured by etching measurements, and inferred to be $4\,\mu$m. The experimental data were then fitted to eq. (4.30) with d_{33} as a free parameter. Taking $L^g = 4\,\mu$m , a d_{33} value of $0.22\,$pm/V ($\chi^{(2)} = 0.44$ pm/V) is found by fitting the data, in good agreement with

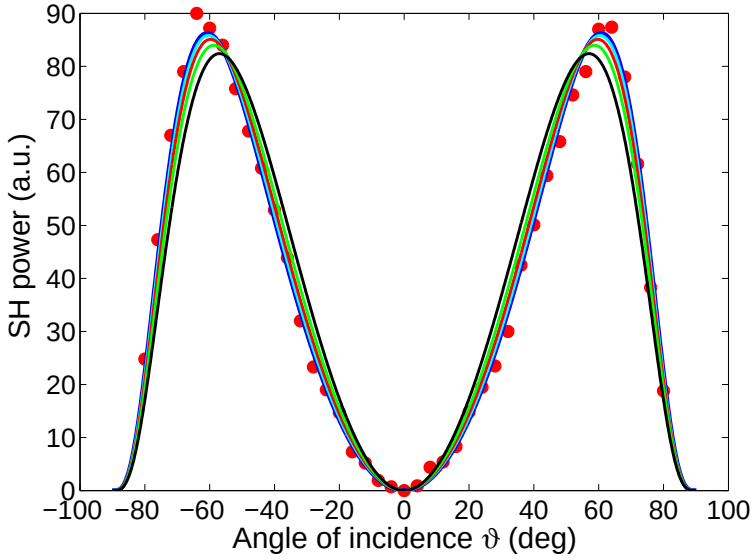

FIGURE 4.16: Second-harmonic signal as a function of the incident angle, for a poled glass sample (circles). The thickness of the nonlinear region was measured to be $L = 4\,\mu$m by etching measurement. The Blue curve is the best fit to the data and $d_{33} = 0.22\,pm/V$ is obtained. Equation (4.30) is fitted to the experimental data assuming different thickness of the nonlinear layer in order to highlight the limitation of the MFT to measurements of thin nonlinear samples: (Yellow) $L = 2\,\mu$m, (Blue) $L = 4\,\mu$m, (Cyan) $L = 8\,\mu$m, (Red) $L = 12\,\mu$m, (Green) $L = 16\,\mu$m and (Black)$L = 20\,\mu$m

previously reported values for poled silica glass (Fig. 4.16).

4.2 Stack Maker's fringe Technique: a practical technique for measurement of second-order nonlinearity in poled glass

In the literature, when the measurement of the thickness of the nonlinear optical layer L in poled glass is impossible using MFT, the reported values of $\chi^{(2)}$ are sometimes only estimated, giving less significance to the achievements in this area. It can possibly be explained by the difficulties of handling hydrofluoric acid for an independent determination of L [103, 159]. Hence, a reliable and practical optical technique to measure the thickness of the induced nonlinear layer would be extremely important in the field of poling.

Modified MFT set-ups, with the sample sandwiched between a couple of prisms or glass hemispheres, were proposed in order to avoid the limitation imposed in the MFT by the total internal reflection, so that the condition $L' > l_c$ is achieved [79, 88]. A variant of the MFT[121] , employs two fundamental beams, at an angle, in order to produce a

non-collinear SH beam which has a much smaller coherence length ($\sim 2\,\mu$m in silica), compared to the collinear ones, so that $L' > l_c$ is easily achieved. Chemical etching in which the etched depth is monitored interferometrically, was also used as an independent measurement of L[76].

In this section a non-destructive and more practical technique is proposed for measuring the nonlinear thickness of poled glass. The technique is based on the interference between SH light beams which are generated by two identically poled glasses pressed together in a stack. Thicknesses, as small as $4\,\mu$m can be measured with a resolution better than $1\,\mu$m.

4.2.1 Principle of Operation

In the technique presented hereafter, a stack is made by pressing in contact two identically poled glasses (or alternatively the same sample cut in two pieces) with the nonlinear layers facing each other. The stack is then probed just as in the MFT (Fig. 4.17). In our "stack" Maker's fringe technique (SMFT), each of the two nonlinear layers generates a SH light beam which interferes with the other one and the SH power at the output of the stack depends on the relative phase between the two SH beams. The key point of the SMFT is that, at a given angle, the ratio of the SH powers measured for the stack ($\mathcal{P}_S^{2\omega}$) and for the single glass ($\mathcal{P}^{2\omega}$) only depends on L' which is the quantity we want to determine. It should be noticed that, at the interface between the two glasses, the sign of the nonlinearity is reversed because of the opposite orientations of $\mathbf{E}_{\mathrm{dc}}$. It follows that the mathematical treatment typically used in quasi-phase matching analysis is applicable to the SMFT as well.

The SH field at the output surface $\mathbf{A}_S^{2\omega}$ is given by the interference between the SH fields generated by the two nonlinear layers.

$$\mathbf{A}_S^{2\omega} \;=\; \mathbf{A}_1^{2\omega} + \mathbf{A}_2^{2\omega}, \tag{4.33}$$

where $\mathbf{A}_1^{2\omega}$ is the SH field generated by the first layer after propagation to the output surface and $\mathbf{A}_2^{2\omega}$ is the SH field generated by the second layer after propagation to the output surface. Any effect due to the presence of interfaces and Fresnel transmission losses will be considered afterwards to simplify the treatment, moreover the hypothesis of undepleted pump is considered as previously. It is worth noting here that the SH field at the output of the first layer $\mathbf{A}^{2\omega}$ is the SH field for a conventional Maker's fringe defined in eq. (4.8). Assuming a uniform $\chi^{(2)}$ across the nonlinear layer, $\mathbf{A}_1^{2\omega}$ and $\mathbf{A}_2^{2\omega}$ can be written as

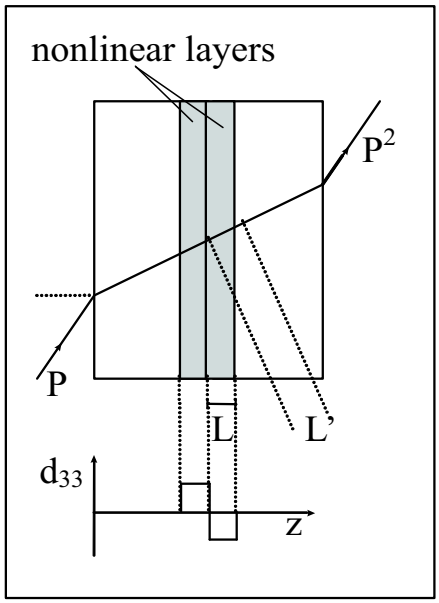

FIGURE 4.17: Schematic of the stack made by pressing two poled glasses together.

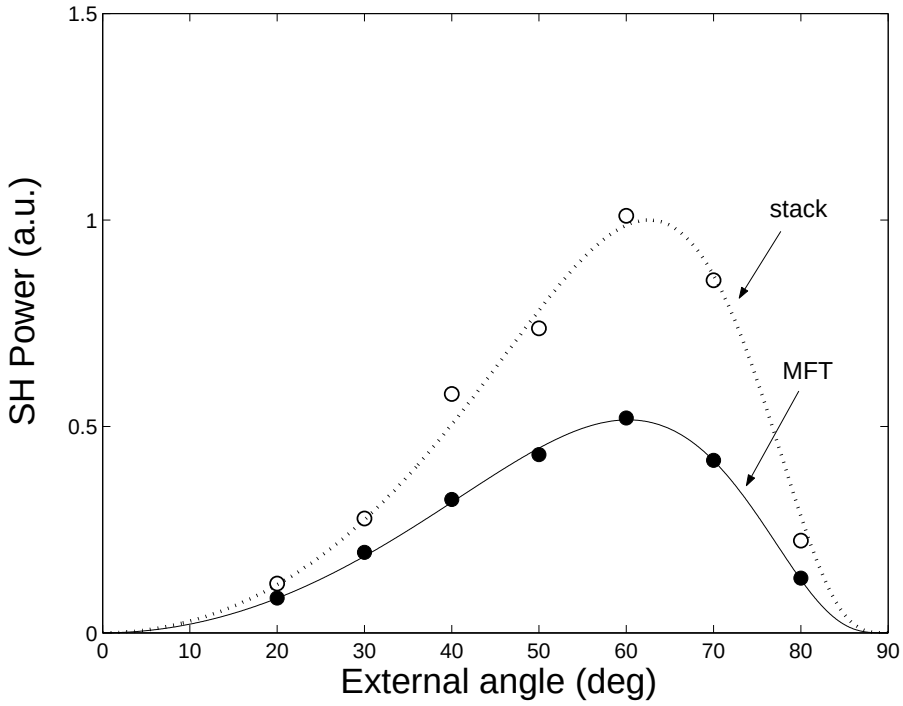

FIGURE 4.18: SH power, as a function of the external angle measured for a single poled glass (solid symbols) and for the stack of two identically poled glasses (open symbols). Data refers to the sample poled for 90 min. From the ratio of the SH powers at each angle, the thickness of the nonlinear layer is calculated and its value is used to fit the data (solid and dashed line).

$$\begin{aligned} \mathbf{A}_1^{2\omega} &= \mathbf{A}^{2\omega} e^{ik_{2\omega}L'} \\ \mathbf{A}_2^{2\omega} &= \mathbf{A}^{2\omega} \left[e^{ik_{\omega}L'} \right]^2 . \end{aligned} \tag{4.34}$$

with $L' = L/\cos(\vartheta_{2\omega})$ where L is the thickness of the nonlinear layer that we want to measure and $\theta_{2\omega}$ the internal angle of propagation for the SH light beam. From eq.(4.33) we have

$$\mathbf{A}_S^{2\omega} = \mathbf{A}^{2\omega} e^{ik_{2\omega}L'} - \mathbf{A}^{2\omega} e^{i2k_{\omega}L'} \tag{4.35}$$

where the minus sign before the second term is caused by the opposite orientation of the frozen-in static electric field in the poled glasses. Simple mathematical manipulation gives

$$\mathbf{A}_S^{2\omega} = 2i\mathbf{A}^{2\omega} e^{ik_{2\omega}L'} e^{-i\frac{(2k_{\omega}-k_{2\omega})L'}{2}} \sin\left(\frac{\Delta k}{2}L'\right) \tag{4.36}$$

The intensity of the SH light beam at the output surface is then obtained by squaring eq.(4.36) and with $I^{2\omega}$ defined in eq.(4.9).

$$I_S^{2\omega} = 4\ I^{2\omega} \sin^2\left(\frac{\Delta k}{2}L'\right). \tag{4.37}$$

The quantity

$$R \equiv \frac{I_S^{2\omega}}{I^{2\omega}} \tag{4.38}$$

is the ratio of the SH beam intensities generated by a stack of two identical poled glasses and by a single poled glass sample. The Fresnel transmission losses and the beam size correction (eqs.(4.18,4.19)) contribute in the same way to the Maker Fringe pattern for both the stack and the single sample. Hence, they simplify in the ratio and finally R is equal to the experimentally measurable quantity

$$R = \frac{\mathcal{P}_S^{2\omega}}{\mathcal{P}^{2\omega}} = 4\ \sin^2\left(\frac{\Delta k}{2}L'\right). \tag{4.39}$$

For $L' = L/\cos(\vartheta_{2\omega}) < l_c$, the function described in eq.(4.39) is monotonic so that, by inverting it, L is uniquely determined:

$$L = \frac{2}{\pi} l_c \cos(\vartheta_{2\omega}) \arcsin\left(\frac{1}{2}\sqrt{\frac{\mathcal{P}_S^{2\omega}}{\mathcal{P}^{2\omega}}}\right) \tag{4.40}$$

where the definition $\Delta k \equiv \pi/l_c$ is used.

Indeed, for $L' = L/\cos(\vartheta_{2\omega}) > l_c$ the SMFT cannot be used, but in this range the MFT provides enough accuracy for the determination of both L and $\chi^{(2)}$. Hence, we found the interesting result that the SMFT is complementary to the MFT and extends its range to smaller values of L. In the stack, the SH power is maximized for $L = lc$ which is the condition for quasi-phase matching. It should also be pointed out that, with the SMFT, the measurement of the thickness is further simplified, compared to other techniques, as the angular dependence of the Fresnel transmission losses and of the beam size correction factor do not have to be taken into account.

4.2.2 Error analysis

The most important sources of errors for the determination of L were found to be the error in the measurement of the ratio $\mathcal{P}_S^{2\omega}/\mathcal{P}^{2\omega}$, the error in the reading of the angle of incidence of the fundamental beam and the error in the coherence length. Assuming realistic values for the aforementioned errors, the error in L is evaluated from eq.(4.40). $\delta L/L$ is found to increase for L below $4\,\mu$m and when the path travelled by the light in the nonlinear layer (L') is equal to the coherence length (see peaks in Fig. 4.19). In such a case the error goes to infinite because around these values, variations in L produce only little variation in the power ratio (eq. 4.40).

The major sources of experimental errors are found in the measurement of the ratio of the SH powers and in the reading of the incident angle. The former contribution to the error is more important when L is small, whereas the latter dominates when L is large, especially if the sample is probed at large angles(Fig.4.20).

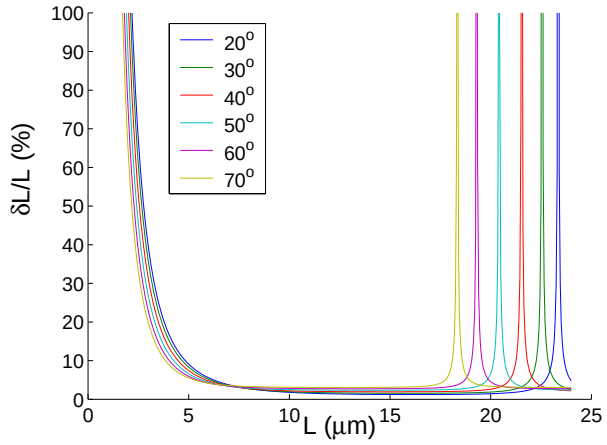

FIGURE 4.19: Percentage error of the nonlinear thickness (L) against L evaluated for different angles of incidence.

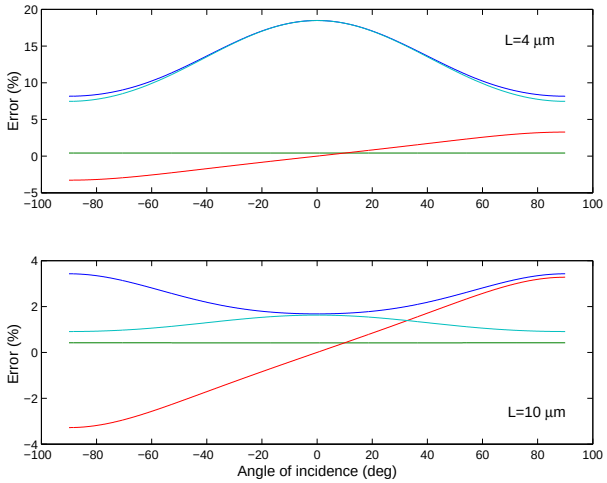

FIGURE 4.20: Contributions to the error in the nonlinear thickness against the angle of incidence of the fundamental beam for two values of L. (green) error in l_c, (red) error in the angle reading, (light blue) error in the ratio $\mathcal{P}_S^{2\omega}/\mathcal{P}^{2\omega}$. (Dark blue) overall error in L.

4.2.3 Assessment of the method

The method to measure the nonlinear thickness in a poled glass presented here is based on the measurement of two Maker fringe patterns. One pattern is recorded using a poled glass, and the second one is measured using a stack made of the measured poled glass and an identical one that could be fabricated either by poling it in the same conditions as the first glass or by cutting the first glass in two halves. The method also requires that the two nonlinear regions are facing each other in the stack. According to eq.(4.21) the ratio of the SH power measured at each angle gives the nonlinear thickness L. Finally, having L, the $\chi^{(2)}$ is estimated with reference with to a α-quartz crystal as described in section 4.1.7.

MFT and SMFT measurements were performed (Fig. 4.18) on a set of 200 μm thick

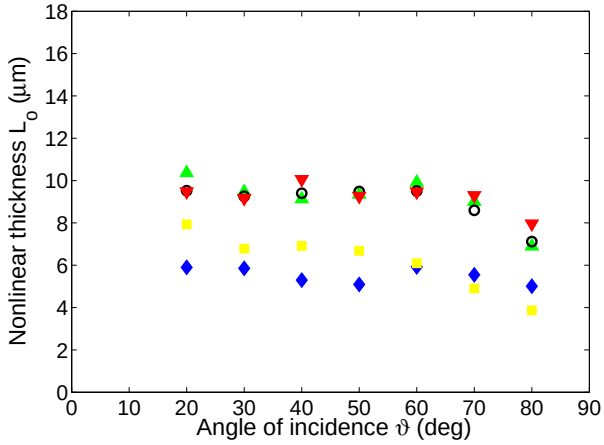

FIGURE 4.21: Thickness of the nonlinear layer in a set of silica plates poled for different times: (diamonds) 7 min, (square) 15 min, (up -triangle) 30 min, (down triangle) 45 min, (circles) 90 min.

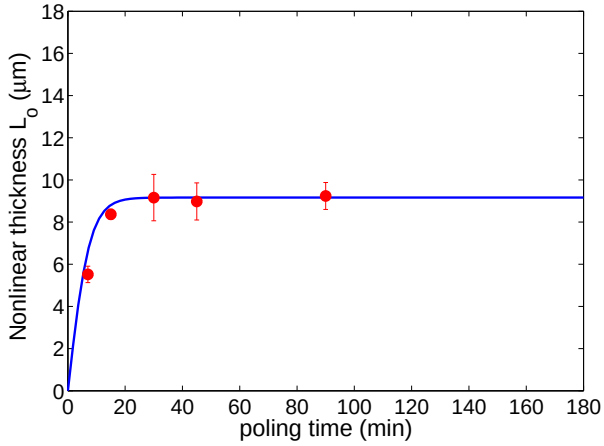

FIGURE 4.22: Measured values for the nonlinear thickness against poling time. The solid curve is the best stretched-exponential fit for the experimental data

silica plates (Herasil 1), poled in air for 7, 15, 30, 45 and 90 minutes at 280 °C, with 4 kV applied voltage. The samples were tested for SHG using a mode-locked and Q-switched Nd:YAG laser ($\lambda = 1064$ nm) with a focused spot radius of $w_o = 26\,\mu$m. The corresponding Rayleigh range ($2z_0 \sim 4$ mm) is long enough to encompass the whole stack, so that the effect of spherical aberrations and astigmatism is reduced. No index matching fluid is used between the samples, since its larger dispersion (compared to air) would introduce a phase shift between the SH beams generated by the two layers, randomly modifying their interference condition and making it impossible to retrieve the value of L. According to eq. (4.40) the thickness of the nonlinear optical layer is calculated, for each sample, at different angles (Fig.4.21). As in the standard Maker's fringe technique, once determined, the value of L is used to fit the MFT pattern (Fig. 4.18) and $\chi^{(2)}$ is evaluated by comparison with α-quartz crystal ($d_{11} = 0.3$ pm/V). A $\chi^{(2)}$ of 0.14 pm/V is determined in the sample poled for 90 minutes. The evolution of L with poling time agrees well with the result of previous studies [75] (Fig. 4.22). Each datum for L

presented in Fig. 4.22 is the average of the values obtained at different angles (Fig. 4.21). The experimental errors, evaluated from the standard error of the mean, are in general below 10%.

Chapter 5

Evaluation of poling methods and materials for devices

The value of the induced second-order nonlinearity in thermally poled silica glass is more than one order of magnitude smaller than the $\chi^{(2)}$ in nonlinear crystals such as $LiNbO_3$. Two main possibilities to reduce this gap can be envisaged: the first possibility is to use a different technique from thermal poling (see section 3.6). Corona poling [23, 157, 160], UV-poling [27, 156],electron-beam poling [24, 161], all-optical poling [162] have been reported so far. The second possibility is to either change or modify the material to make it more prone to the poling process. Several groups are now working on poling of glasses other than silica (see Section 3.5). Glasses with high $\chi^{(3)}$ [8, 100, 159] are the most promising in order to obtain a larger $\chi^{(2)}$ (see $\chi^{(2)} = 3\chi^{(3)}E_{\mathrm{dc}}$). Moreover, pre-treatment of silica glass, with the aim of preserving its excellent optical properties whilst including new features, has already proven to be effective. For example it was shown that the creation of point defects in synthetic silica by UV exposure led to a ten fold increase in the value of the nonlinearity induced by thermal poling [80].

This thesis led to the discovery of a new poling method [28]: UV-fs poling, where two-photon absorption of femtosecond UV pulses in the presence of an applied electric field creates a permanent space-charge in pure silica glass. This technique is described in section 5.1. Various nanostructured glass-ceramic families have also been characterized, both using standard MFT technique and the new stack Maker's fringe technique introduced in section 4.2. In particular, thermal poling as efficient as in silica, was demonstrated in photosensitive tin-doped silica glass (Section 5.2). The addition of photosensitivity to the optical properties of poled silica makes this new material attractive for planar poled devices where waveguides can be written by UV exposure. The generation of point defects in silica and their effect on the poling process have been studied by exposing the glass to either γ-ray or IR-femtosecond pulses. γ-ray pre-treatment has been experimentally investigated in both type-II and type-III silica glass, in a wide range

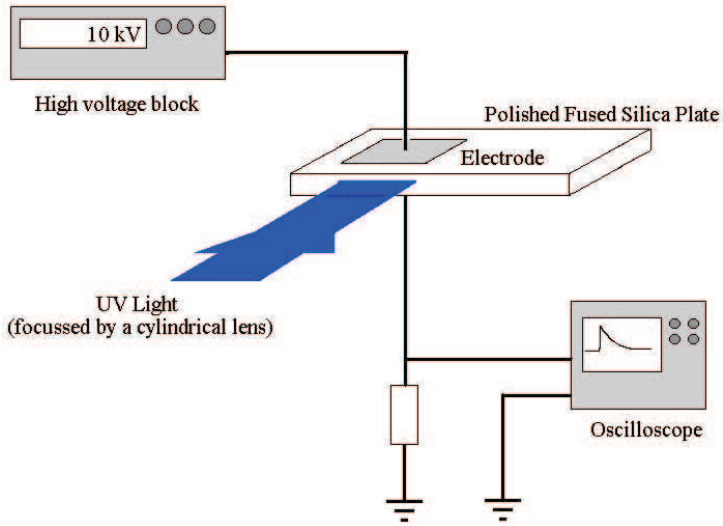

FIGURE 5.1: Schematic of the UV-assisted poling experiment with induced photocurrent measurement.

of doses and dose-rates of exposures to γ-rays. This study is presented in Section 5.3. An original contribution of this thesis is also the discovery that IR femtosecond pre-treatment of silica enhances the capability of the glass to freeze an electric field, leading to higher nonlinearity (Section 5.4).

The issue of the stability of the nonlinearity in poled glass, that is fundamental for the development of practical devices, has been addressed in Section 5.5. Glass compositions, whose second-order nonlinearity is far more stable than for poled silica, were identified.

In Section 5.6, the compatibility of each poling method, glass, and glass pre-treatment with the fabrication of a glass based frequency doubler, is critically discussed on the basis of both literature review and of the experiments presented in this chapter.

5.1 UV-fs poling

In this section the discovery of a new poling technique is reported. Differently from Fujiwara's experiments a high intensity UV femtosecond laser source and un-doped fused silica samples, excited by a two-photon mechanism were used. After irradiation, a strong second-harmonic signal in the areas of the sample that had been subjected to both the electric field and UV light, was observed. To the best of our knowledge, it is the first experimental demonstration of direct UV-poling in pure fused silica.

Samples Preparation

The experimental set-up is shown in Fig.5.1. The fused silica samples used for poling were made from Herasil 1 glass (Heraeus Quarzglas GmbH) and had dimensions $37.2 \times 11 \times 0.5\,\mathrm{mm}^3$. All the sides of the samples were polished and aluminium electrodes,

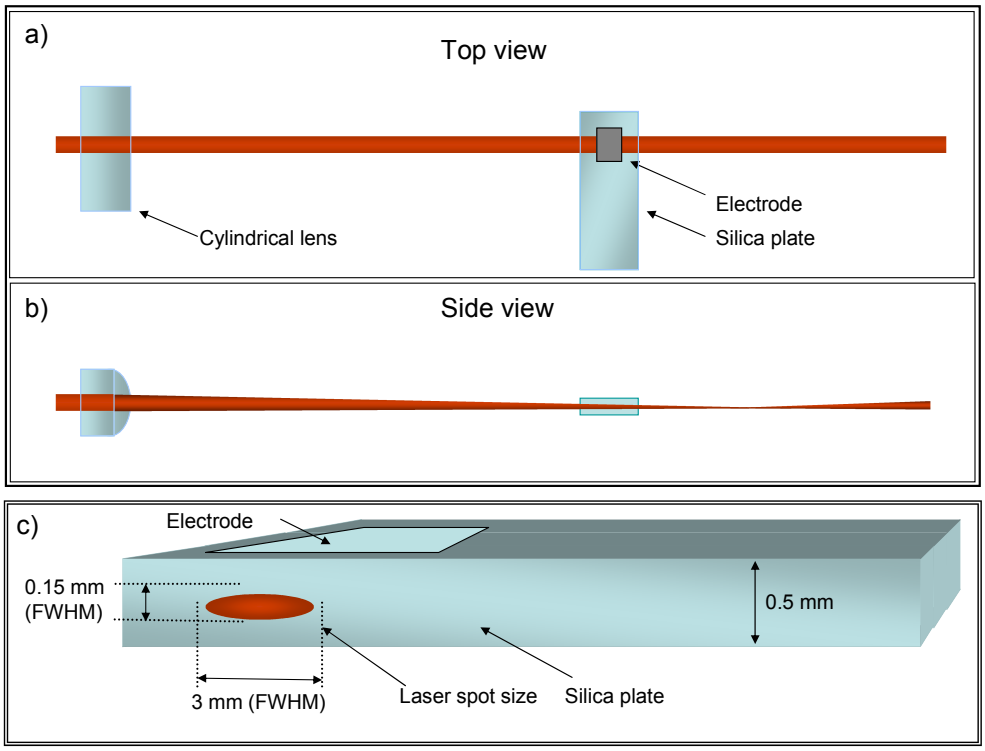

FIGURE 5.2: Schematic of the UV-assisted poling experiment: details of the beam propagation.

$11 \times 5\,\mathrm{mm}^2$, were deposited on both plane sides of the samples in such a way that the edges of each electrode were at a distance of about 3 mm from the end of the plate and side edges (see Fig.5.1).

For sample irradiation, we used the UV pulses from a femtosecond Nd:glass laser (Twinkle, Light Conversion Ltd., Vilnius, Lithuania). It is based on an active-passive mode-locked negative-feedback controlled Nd:glass master oscillator, a stretcher, a Nd:glass regenerative amplifier, and a compressor. It delivers 0.9 ps pulses with energy of as much as 4 mJ at 1055 nm with a repetition rate of 27 Hz. Further compression to 200 fs pulse width is accomplished in the course of second-harmonic generation with a potassium dihydrogen phosphate type II (KDP) crystal with time predelay between pulses with orthogonal polarization. The subsequent generation of third (351 nm), fourth (264 nm), and fifth (211 nm) harmonics of fundamental radiation is carried out in KDP and β-barium borate (BBO) crystals. The energy stability of pulses at 264 nm is $\sim 10\%$ [163].

The laser parameters used for the UV femtosecond poling were the following: the pulse energy, ε_p, is around $200\,\mu$J; the wavelength, λ, is 264 nm; the pulse duration,τ_{FWHM}, is 220 fs ($\tau = \tau_{\mathrm{FWHM}}/\sqrt{ln2}$ at 1/e); the beam radius, w_{FWHM}, is 0.15 cm ($w = w_{\mathrm{FWHM}}/\sqrt{ln2}$ at 1/e); and the repetition rate, R_r, is 27 Hz. The UV radiation was focussed into the narrow side of the sample by a cylindrical lens with focal length 21.8 cm. The sample was placed at a distance of 21 cm from the lens (Fig. 5.2).

The peak beam intensity, I_0, is calculated assuming that the pulses generated by the laser have a Gaussian temporal and spatial profile. The following representation was chosen for the Gaussian beam:

$$I(r,t) = I_0 exp\left[-\frac{r^2}{\left(w_0/\sqrt{2}\right)^2}\right] exp\left[-\frac{t^2}{(\tau/2)^2}\right] \tag{5.1}$$

where $w = w_0/\sqrt{2}$ is the beam radius when the intensity has decreased by 1/e and τ the pulse width at 1/e. Eq.(5.1) has to be integrated over time and space in order to obtain the pulse energy, ε_p. This leads to the following result:

$$\varepsilon_p = \int_{-\infty}^{+\infty} dt \int_0^{+\infty} I(r,t) 2\pi r dr = \frac{\pi\sqrt{\pi}}{4} I_0 \tau w_0^2 \tag{5.2}$$

From the above expression the peak beam intensity is calculated to be:

$$I_0 = \frac{\varepsilon_p}{\frac{\pi\sqrt{\pi}}{4}\tau w_0^2} \tag{5.3}$$

corresponding to 8.7 GW/cm^2 on the lens. Due to the focusing the beam cross sectional area at the sample edge is reduced by approximately 27 times, as calculated using Gaussian beam propagation. As a result the peak intensity incident on the sample is about 236 GW/cm^2. The incident fluence was calculated from the following equation [28]:

$$E = \frac{\varepsilon_p N}{\pi w_0^2} \tag{5.4}$$

where N is the total number of pulses incident on the sample. A high voltage block FC30P4 (Glassman High Voltage, Inc.) was used to create an electric field of about 200 kV/cm through the sample. The sample, with the high voltage applied across it, was irradiated with the high-intensity UV laser light for approximately 3 hours (total incident fluence of around 8 kJ/cm^2). Using the experimental values for the two-photon absorption coefficient for Herasil glass reported in [164], we can estimate the light intensity value entering the volume inside the sample under high voltage as 40 GW/cm^2 (the pulse energy, entering the poling volume, is about 40 μJ). The total irradiation fluence regarding the poling volume was 2 kJ/cm^2.

Current Measurements

A digital oscilloscope LT372 (LeCroy) was used to measure the photoelectric current induced in the sample while applying the high voltage and exposing it to the UV-femtosecond pulses. No current was observed in the absence of high-intensity UV light. Immediately, at the start of irradiation, a strong photocurrent pulse with an amplitude of up to 20 V (measured across an 100 kΩ resistor) appeared, which corresponded to a conductivity value of $\sigma = 2\times10^{-9}$ cm$^{-1}\Omega^{-1}$ (resistivity value $\rho = 5\times10^8$ cm$\cdot\Omega$, which is ten

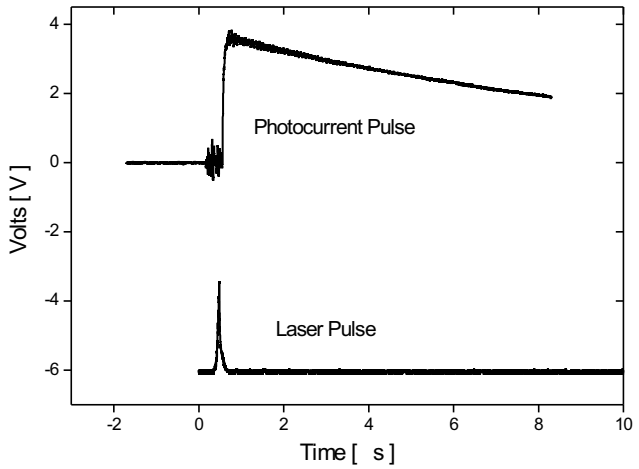

FIGURE 5.3: Laser pulse and simultaneous current pulse

orders less than the standard reference value for room temperature $\rho = 10^{18}\,\mathrm{cm}\cdot\Omega$[165]). The calculated initial quantum yield of charged particles between the electrodes was about 2×10^{-6}, if we presume that the time resolution of our oscilloscope was 50 ns. During the irradiation, the pulse amplitude value degraded rather quickly (during some seconds) to a level of some volts (Fig.5.3). A horizontal movement of the sample in respect to the laser beam led to a revival of the photocurrent signal. After switching off the applied voltage, the photocurrent pulse changed its polarity and continued to degrade. The observed photocurrent behavior is qualitatively consistent with the one induced in earlier experiments on two-step ionization $S_0 \rightarrow S_1 \rightarrow S_N$ of oxygen deficient fused silica by KrF excimer laser radiation with $\lambda = 248\,\mathrm{nm}$ and $t = 25\mathrm{ns}$[166]. However, a side effect, which is difficult to isolate in this type of experiments, is the photoelectric emission of electrons from the electrodes, when illuminated by high energy UV photons. In order to estimate the importance of the contribution of photoelectrons to the measured current, future experiments will be performed using various metal electrodes, having different work-functions. Another possibility is to shine the UV laser beam alternatively on the anode electrode, inside the glass and on the cathode electrode and see how the measured current is affected.

Measurements of the Second-Order Nonlinearity

After the poling and removal of the electrodes (by etching), the sample was tested for evidence of second-harmonic generation. As a pump source, a mode-locked and Q-switched Nd:YAG laser was used ($\lambda = 1064$ nm). For the Maker's fringe measurement the sample was placed on a rotation stage and the laser beam was focused on the poled area, with polarization parallel to the plane of incidence. The generated SH light was detected with a photomultiplier. The fit to the experimental data reveals that the region with an induced $\chi^{(2)}$ corresponds to the whole bulk volume between the two electrodes

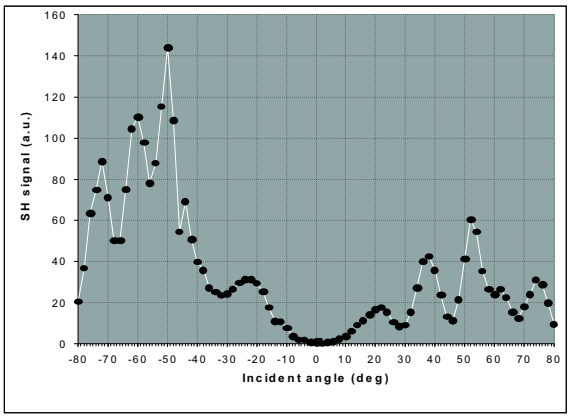

FIGURE 5.4: Maker's fringe measurement on the UV poled sample

(Fig.5.4).

The comparison of the SHG signal value with that obtained from a reference sample (crystalline α-quartz) with a known $\chi^{(2)}$ value of 0.6 pm/V, allowed us to estimate the maximum value of the induced second-order nonlinearity as about 0.02 pm/V. A rectification model, $\chi^{(2)} = 3\chi^{(3)}E_{\mathrm{dc}}$ with $\chi^{(3)}$, being the third-order nonlinear susceptibility, equal to $2 \times 10^{-22}\,\mathrm{m^2V^{-2}}$ for silica and the applied electric field E_{dc} equal to 200 kV/cm, gives a predicted $\chi^{(2)}$ of 0.01 pm/V in remarkable agreement with the measured value. If the same experiment is performed in twin-hole fibres, where the maximum applied field is only limited by the dielectric strength of silica at room temperature (2×10^9 V/m [75]) we can tentatively predict $\chi^{(2)}$ exceeding 1 pm/V. The pump beam was also scanned across the surface of the sample to test the distribution of the second-order nonlinearity (Fig.5.5). The geometry was the same as for the Maker's fringe measurements described above. The angle of incidence was chosen to be close to normal incidence (10 degrees) to reduce the effects of non-uniformities. A stronger SH signal is observed near the side where the laser beam entered the sample which could be explained by the decrease of UV intensity caused by two-photon absorption in the glass. During the inscription procedure we poled several regions under the electrodes by translating the sample. It is clearly seen that the second-harmonic signal is observed only in the area under the electrodes illuminated by the UV light beam, indicating that the poling takes place under the simultaneous action of both UV light and the applied electric field.

5.2 Poling of nanostructured glass-ceramics

Crystals which do not possess inversion symmetry inevitably show second-order nonlinear optical properties. Therefore, composite materials containing nonlinear nanocrystals are interesting for nonlinear optical applications especially if orientation of the nanocrystals is achieved.

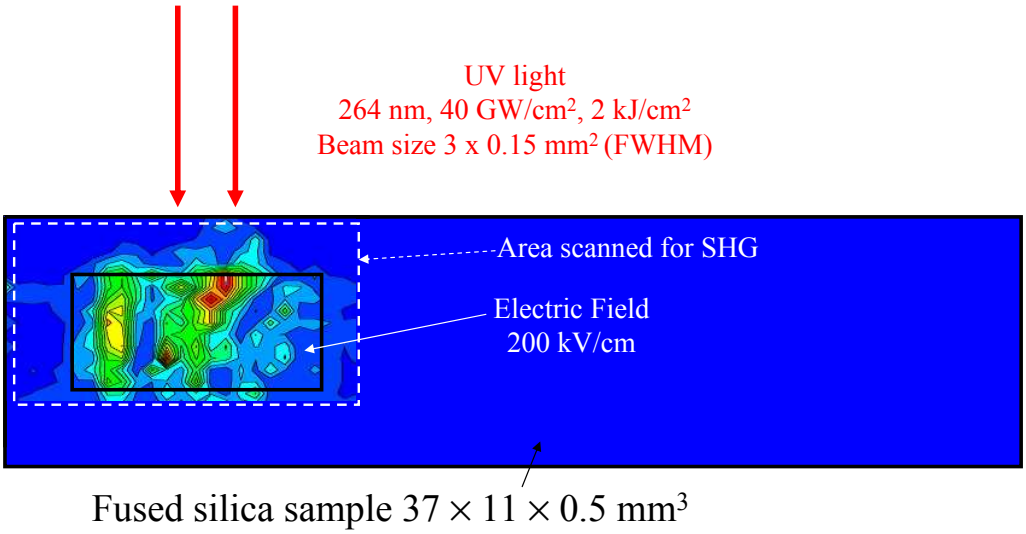

FIGURE 5.5: The two dimensional distribution of the second-harmonic signal in the poled fused silica sample. The sample geometry and the area covered by the electrode are marked by the black lines and the area that was scanned for SHG is delimited by the white lines. The UV beam entered the sample from the top.

So far only a few studies have been reported on second harmonic generation in semiconductor nanocrystals and the mechanism leading to the second harmonic is still unclear. Second-harmonic generation in commercial filter glass, where CdSSe semiconductor nanocrystal were dispersed, have been reported[167]. It has been suggested that photo-induced formation of positive holes and electrons in the semiconductor nanocrystalline phase is responsible for an internal electric field, leading to SHG via $\chi^{(2)} = 3\chi^{(3)}E_{\mathrm{dc}}$. Another study claims that surface effects, inherently lacking in inversion symmetry, as well as bulk effects can contribute to second harmonic generation[168]. In that work the effect of the surface is found to enhance the first order hyperpolarizability corresponding to the second-order optical nonlinearity for CdSe nanocrystals smaller than 1.3 nm in radius.

SHG in CuCl-nanocrystal-embedded indium tin oxide film

CuCl is a semiconductor nanocrystal with a zinc-blende type structure and it possesses a large second-order nonlinearity. In addition it shows high transparency in the visible wavelength region. Recently SHG in CuCl nanocrystal-embedded silica glass films and thermally poled borosilicate glasses containing CuCl nanocrystals have been reported [169, 170]. Second harmonic generation from CuCl nanocrystal-embedded amorphous indium tin oxide(ITO) film, which is known as a transparent electrode, has also been reported [171]. SHG was larger by one to two orders of magnitude in the ITO thin film than in the silica glass film. The second-order nonlinear optical properties of the ITO thin film containing a nanocrystalline phase are interesting considering that the ITO crystalline film itself exhibits SHG [172] and that it has been found to enhance the second harmonic intensity of organic polymer (PMMA) film, when this was deposited

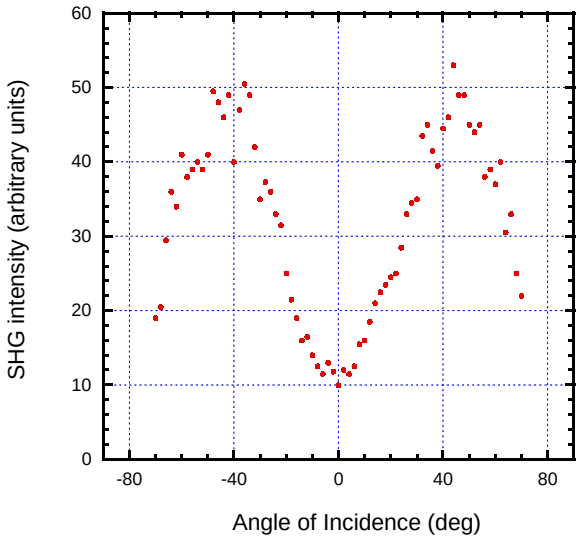

FIGURE 5.6: Maker Fringe pattern for the CuCl nanocrystal-embedded ITO film.

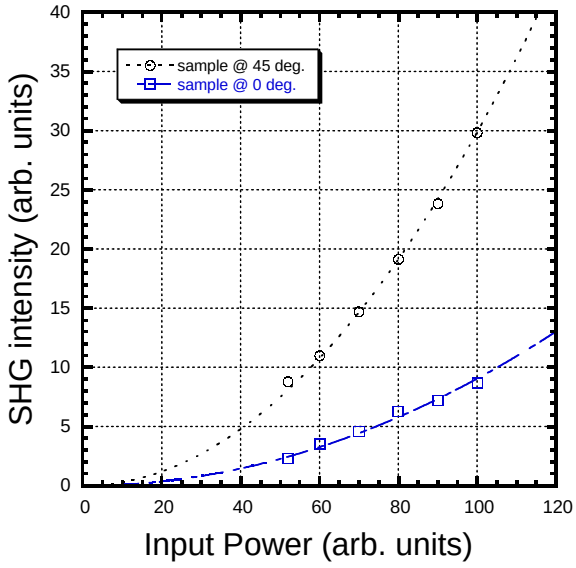

FIGURE 5.7: Second harmonic dependence on the incident laser power for the CuCl nanocrystal-embedded ITO film. The two curves refer to the angle of incidence of the fundamental wave on the sample: (square) 0° and (circle) 45°. The solid lines drawn by least square fitting show that the SHG is proportional to the second power dependence of the incident laser power.

onto the ITO film, thanks to surface-induced ordering of the polymer [173].

As for the CuCl nanocrystal-embedded ITO film, details for the second-harmonic generation still remain unclear, in the present study, which was carried out in collaboration with professor Katsuhisa Tanaka[1], SHG under various conditions is reported.

The CuCl nanocrystal-embedded ITO film has been prepared by sputtering. The preparation process is extensively described in ref. [169]. According to X-ray diffraction analysis, the film is composed of CuCl in a crystalline phase (20 *nm* size) and amorphous ITO. SHG measurements are performed using a Q-switched, mode-locked Nd:YAG laser and the second-harmonic is detected using a photomultiplier and an oscilloscope. The Maker's fringe pattern is shown in Fig.(5.6). The maximum of the second-harmonic is around $40° - 45°$ agreeing with previous measurements in analogous samples [171]. The noise of the data is mainly due to the inhomogeneity of the sample. The random orientation of the CuCl nanocrystals causes SH light to be produced at normal incidence. Indeed, the generation of SH light from powders of nonlinear crystals have been exploited in the past for the measurement of nonlinear coefficients. In order to demonstrate that the measured signal is genuinely second-harmonic we show in Fig. (5.7) that the SHG intensity increases with a second-power law while increasing the fundamental power. The two curves refer to a different orientation of the sample with respect to the fundamental wave: normal incidence (square) and 45^o (circle). The dashed lines are the best least-squares fit with a second-order polynomial confirming that the measured signal is second-harmonic even at normal incidence.

Poling of tin-doped silica glasses fabricated by sol-gel technique
Promising results in terms of nonlinearity were obtained in silica glass prepared by sol-gel. In an early paper, the increase of bulk second-order nonlinearity (SON) with the OH concentration was reported [174]. More recently, high SON has been demonstrated in sol-gel glasses with low OH content. In the latter case the second-order optical nonlinearity was located in a 20 μm thick region close to the anodic surface [82].

Sn-doped silica-based materials have been supplied by N. Chiodini and M. Paleari from Università di Milano-Bicocca (Italy). They were prepared by a sol-gel method [174] and synthesized at 1050 °C. Thermal poling has been investigated in Sn-doped glasses and SnO_2:SiO_2 nanostructured composites. The tin-content was $\sim$ 1.2%w/w and 2 %w/w, respectively. In the samples with lower concentration Sn acts as a substitutional atom for silicon in the silica matrix. In the sample with the higher concentration, Sn atoms segregate, giving rise to nanosized SnO_2 clusters homogenously dispersed in the silica matrix [175].

Thermal Poling has been carried out in air at 280 °C for 30 min with 3 kV applied. The second-order optical nonlinearity induced in glass by poling has been evaluated through

[1]Department of Chemistry and Material Technology, Faculty of Engineering and Design, Matsugasaki, Sakyo-ku, Kyoto, Japan

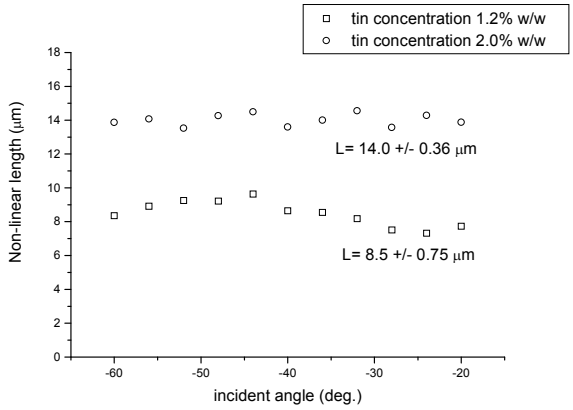

FIGURE 5.8: SMFT measurement of the thickness of the poled region in thermally poled tin-doped silica glass.

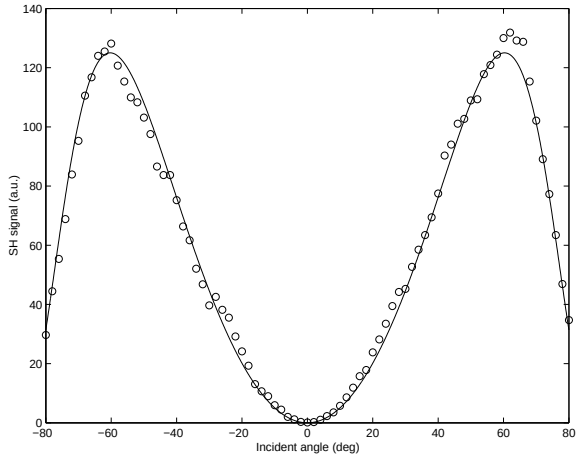

FIGURE 5.9: Maker's fringe pattern of thermally poled tin-doped silica glass.

the Stack Maker's fringe technique (SMFT) described in Section 4.2. The depth of the nonlinear region was found to be 8.5 ± 0.75μm and 14.0 ± 0.36μm for the glass and glass-ceramic, respectively (Fig. 5.8). The second-order susceptibility was measured with the conventional MFT (Fig. 5.9 and 5.10). A $\chi^{(2)} = 0.26$pm/V was found for the glass system (1.2%w/w tin-content) whereas $\chi^{(2)} = 0.18$pm/V was found for the glass-ceramic (2.0%w/w tin-content). The $\chi^{(2)}$ is found to be almost the same in both the glass and glass-ceramic. Tentatively we can draw the conclusion that in this glass system, during the poling process, the glass matrix is mainly involved despite the presence of nanocrystals.

5.3 γ-ray pre-treatment of silica glass

In the past, it has been reported that silica glass exposed to gamma radiation exhibits enhanced SHG when it is thermally poled [176]. Although promising, this result has

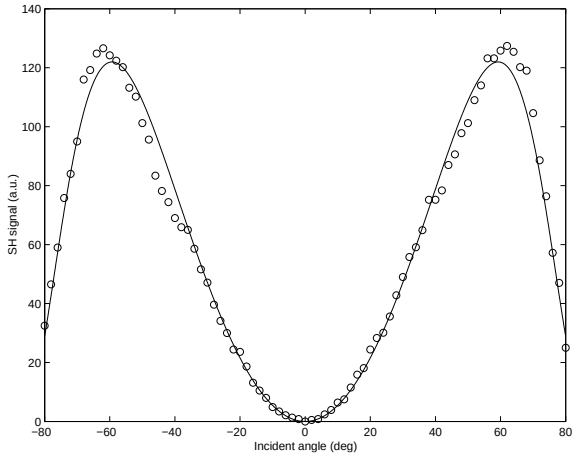

FIGURE 5.10: Maker's fringe pattern of a thermally poled tin-doped silica glass-ceramic.

been reported only for type-III silica glass (manufactured by flame hydrolysis of $SiCl_4$) which was irradiated at a maximum dose of 100 kGy. On the other hand, all the poling parameters being identical, SHG is 10 times higher in type-II silica glass (manufactured by flame fusion of quartz) than in type III silica glass. In order to evaluate the ability of gamma-radiation pre-treatment to increase the second-order nonlinearity, we have carried out thermal poling of silica glass modified by gamma radiation. Type-II (Herasil) and type-III (Suprasil) silica glass samples (0.53 mm and 1 mm thick, respectively) were exposed to gamma-rays from a Cobalt-60 source at high dose rates of 10 kGy/h and total doses from 100 kGy to 10 MGy. Temperature during irradiation was about 55 °C. After irradiation, the samples were thermally poled at 280 °C, 4 kV for 30 minutes. For each type of silica, a fresh (non-irradiated) sample was poled in the same conditions and taken as a reference. Results of the SHG tests are summarized in Table 5.3 (the incident angle of 60 ° was chosen because it corresponds to the maximum SH intensity in the Maker fringe pattern of thermally poled silica glass). Depending on the type of silica and the dose, the SH intensity in the irradiated samples is either considerably reduced or almost unchanged in comparison with the corresponding reference sample. Enhancement of SH intensity is not observed, in any of the samples, including the Suprasil ones, in contradiction with [176]. MFT measurements were performed on the irradiated samples. Surprisingly, we observed Maker's fringes in both Herasil and Suprasil samples which were irradiated at 7 MGy and then thermally poled, meaning that the depth of the induced nonlinear region was larger than the coherence length, i.e. larger than 24 μm. In both cases the period of the oscillations corresponds to the thickness of the sample. This result indicates that the nonlinearity is induced either in the whole bulk or in thin layers at both the anode side and the cathode side. In the former case, the orientation of dipoles (possibly related to defects) would be responsible for the nonlinearity. Indeed, typical UV optical absorption bands due to defects (e.g. E' centre) are observed in all the irradiated samples, showing that the glass is significantly modified after exposure

Sample	Dose (KGy)	Dose Rate (KGy/h)	$I_{SH}/I_{SH_{ref}}$
H1	7096	9.07	8.6×10^{-5}
H2	1466	9.07	0.92
H3	817	9.07	0.97
S1	7096	9.07	1.1×10^{-3}
S2	1466	9.07	5.3×10^{-4}
S3	817	9.07	4.2×10^{-4}
S4	119	6.78	7.8×10^{-4}

TABLE 5.1: Results of SHG tests. The p-polarised pump beam from a Q-switched and mode-locked NdYAG laser (1064 nm) was used to probe the sample at an incident angle of 60°. SH intensity is normalised to that measured in a non-irradiated sample. H: Herasil (type II fused silica, Na and Ge impurities), S: Suprasil (type III synthetic silica, 600-1000 ppm water impurities).

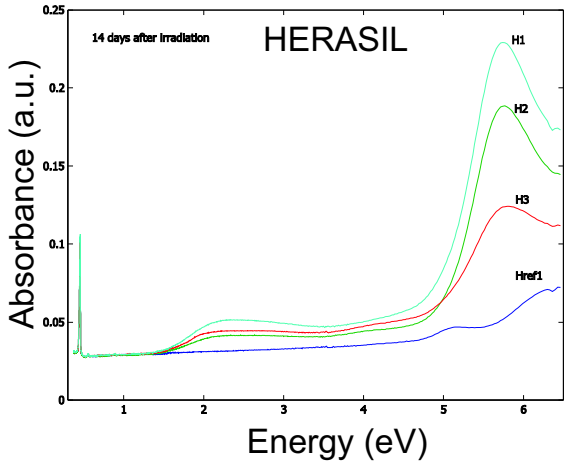

FIGURE 5.11: Optical absorbance spectra of as-received Herasil glass sample (Href1) and gamma-irradiated Herasil glass samples (H1-H3).

to gamma rays (Figures 5.11 and 5.12). Although no enhancement of the second-order nonlinearity could be obtained by gamma-irradiation pre-treatment, these new and unexpected results on thermal poling of silica glass modified by gamma radiation are important for our understanding of the poling mechanisms, in particular on the aspects related to the role of defects.

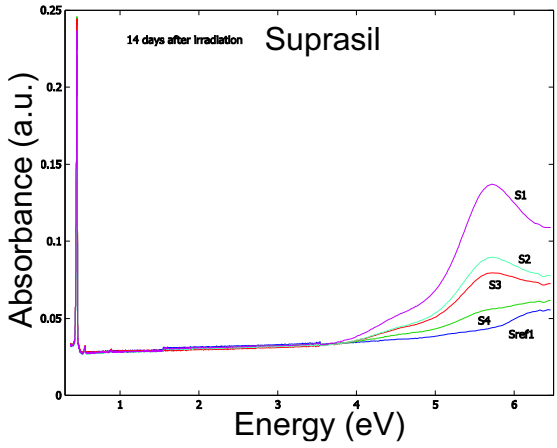

FIGURE 5.12: Optical absorbance spectra of as-received Suprasil glass sample (Sref1) and gamma-irradiated Suprasil glass samples (S1-S4).

5.4 IR-fs laser pre-treatment of silica glass

In this work the silica is first modified by irradiation with a focused femtosecond laser. The femtosecond irradiation, by a multiphoton absorption process, violently breaks the Si-O covalent bonds and defects, such as oxygen deficiency centers, E' centers and NBOHC are created inside the silica as well as densification [33]. Although much is known about the type of defects generated by femtosecond irradiation, little is known about the effect of these defects on the poling process.

Preparation of the samples

A refractive index grating of 20 μm period and 4 μm line width is written within a fused silica glass plate (Herasil 1 by Heraeus) by scanning ($v = 200\,\mu$m/s) with the focused beam produced by a regeneratively-amplified mode-locked Ti:Sapphire laser operating at $\lambda = 850$ nm, 150 fs pulse duration and 250 kHz repetition rate. The energy is 1.2 μJ per pulse. The grating is written in the bulk of the glass with its plane parallel to the surface of the silica plate. The silica plate is polished until the surface reaches the grating. Thermal poling is then carried out in air for 15 minutes at 280 °C with 4 kV applied. The short poling time, together with the polishing, ensures overlapping between the grating and the nonlinear layer created by the poling, the latter usually being only a few microns thick.

Experimental setup

After poling, SHG in the poled glass is investigated using a mode-locked and Q-switched Nd:YAG laser ($\lambda = 1064$ nm), with a focused spot size of $w_0 = 4.1 \pm 0.4\,\mu$m, smaller than the spacing between two grating lines. The polarization of the pump beam is controlled by means of a half-wave plate. The experimental setup is described in Fig. 5.13. The silica plate containing the grating is mounted on a rotation stage and placed in the focus

of the Nd:YAG laser beam. A step-motor translation stage is used in order to scan the beam across the grating. The second harmonic light generated in the poled region is detected by a photomultiplier (PMT) and recorded by an oscilloscope. Simultaneously, by means of a beam splitter placed in front of the PMT, the SH light spot is imaged on a CCD camera connected to a computer for analysis. A white light beam collinear with the laser beam is also used in order to overlap, in the plane of the CCD camera, the image of the grating with the image of the SH light spot thus enabling assessment of whether the SH light is generated outside the grating, on a grating line or in between two lines. The sample was probed with either the grating lines parallel or perpendicular to the plane of incidence and with either an s-polarized or p-polarized pump beam (see Fig. 5.14).

Results and Discussion

First, before poling, the sample is tested to characterize structural modifications induced by femtosecond irradiation[33]. The photoluminescence (PL) spectrum is recorded by pumping with an He-Ne laser ($\lambda = 632.8\,\text{nm}$) while scanning the beam perpendicular to the grating lines. The PL intensity peak at 1.9 eV (655 nm) is associated with non-bridging oxygen hole centres (NBOHC) [177]. The extremely strong PL signal observed on the grating lines (Fig. 5.15(top)) indicates that a large number of these defects is induced by irradiation. No SH light is detected before poling.

After poling, a well-defined modulation of the SH light, having the same period as the grating, is observed, while scanning the p-polarized pump beam across the grating lines oriented parallel to the plane of incidence (Fig. 5.15(bottom)). In the region well away from the grating SH light is generated, as expected for uniformly poled regions, with a well-defined Gaussian spot (Fig. 5.16(a)). A significant enhancement in the SH intensity is observed when the pump beam is focused on the grating lines (Fig. 5.16(b),(d)). The average enhancement is a factor of two compared to the poled region well away from the grating. Remarkably the SH intensity generated when the pump beam is focused between two lines (Fig. 5.16(c)) has the same level as outside the grating. With an s-polarized pump beam focused on a grating line no SH light is generated on that line but, quite surprisingly, two lobes are observed, one on each side of the line (Fig. 5.16(e)). The diffraction pattern in the far-field, although not shown here, presents a gap in the centre suggesting that the two lobes are π-out of phase. Testing the sample in a different geometry, i.e. by scanning across the grating with the plane of incidence perpendicular to the grating lines and with a p-polarized pump beam, a bright SH spot is visible on the left side of each line if the incident angle is positive, whereas the spot is on the right side if the incident angle is negative (Fig. 5.17).

The enhancement of SHG when the pump beam is upon a grating line gives evidence that the poling process is more efficient due to the structural modifications in the irradiated glass. There are indications that E_{dc} is higher in the irradiated regions. The presence of a large number of defects such as NBOHC could be responsible for the higher frozen-

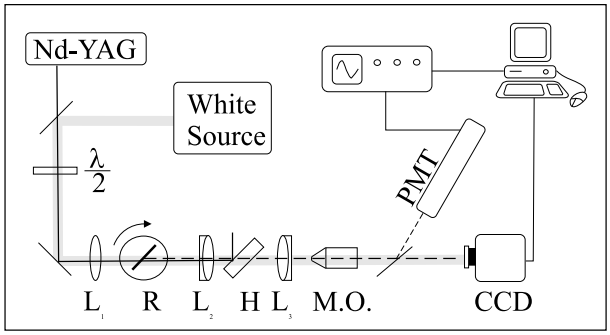

FIGURE 5.13: Experimental setup for measuring and imaging the SH light generated from the sample (S). Paths of the pump beam (1064 nm) and the SH light are indicated by thin and dashed lines respectively. White light illumination used for imaging the sample is indicated by a shaded grey stripe. L_1, L_2, L_3 lenses; R rotation stage; H harmonic separator; $M.O.$ microscope objective; PMT photomultiplier tube; CCD charge coupled device.

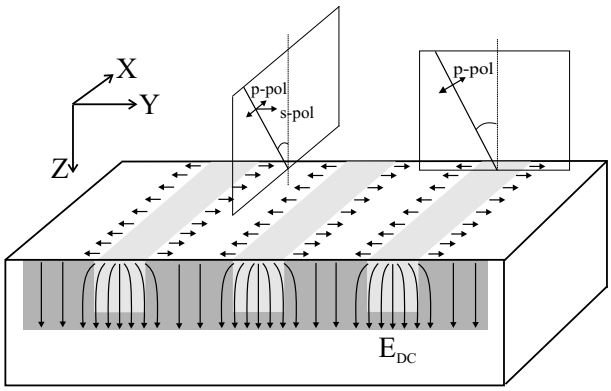

FIGURE 5.14: Schematic of the sample and geometry used for SHG tests. The regions of the glass modified by femtosecond irradiation before poling (i.e. the grating lines) are indicated in light grey. The poled region, lying underneath the anode side (top surface), is indicated in dark grey. In the poled region the field lines of the electrostatic field frozen in glass during poling (E_{dc}) are sketched. The frozen-in field has components along z and x directions (the latter is symbolized by arrows on the top surface). For SHG tests, the plane of incidence is either parallel or perpendicular to the grating lines and the pump beam is either p-polarized or s-polarized.

in electrostatic field and moreover these defects could be oriented and contribute to the enhancement of SHG. There are also indications that the spatial distribution of E_{dc} is changed by the femtosecond irradiation treatment. Assuming the field lines of E_{dc} are those sketched in Fig. 5.14, our experimental results can be explained. In the first geometry, with the plane of incidence parallel to the grating lines and with p-polarized pump beam, the component of E_{dc} perpendicular to the surface (Z axis) is probed. Possible distortions of the electrostatic field distribution are expected to lie in the YZ plane from symmetry considerations and therefore cannot give any contribution to SHG in this geometry. The observed enhancement of the SHG when the beam is focused on a grating line is due to a higher electrostatic field in the irradiated regions (Fig. 5.16(b),(d)). In the same geometry, but with an s-polarized pump beam, the Z-component of E_{dc} does not give any contribution to SHG and there is no SHG on a line,

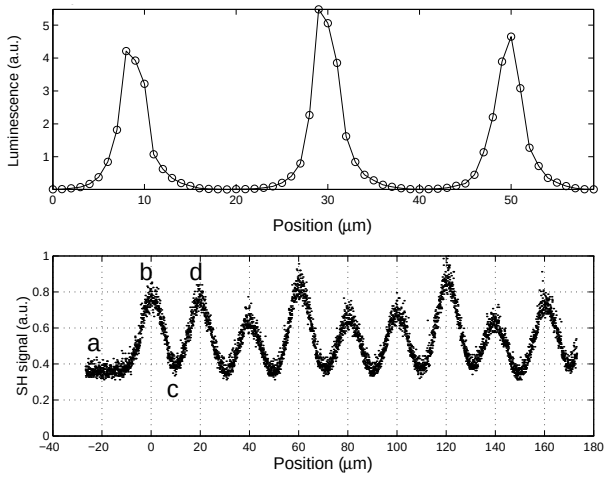

FIGURE 5.15: Upper graph: Photoluminescence (1.9 eV) intensity recorded before poling while scanning a He-Ne beam across the sample. The intensity peak occurs when the beam position is on a grating line. Lower graph: SH signal recorded after poling while scanning the Nd:YAG pump beam (1064 nm) across the sample. Labels indicate beam positions: outside the grating (a), on a grating line (b),(d), in between two lines (c).

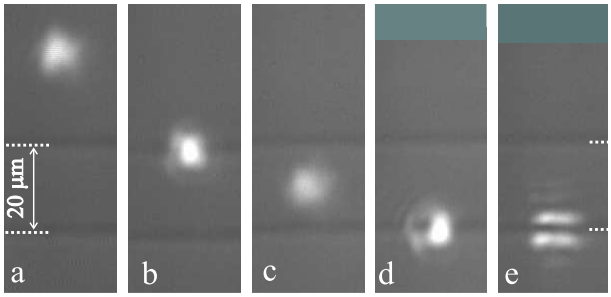

FIGURE 5.16: Images of the SH light spot recorded while probing the sample with the grating lines parallel to the plane of incidence, with p-polarized pump (a to d) and s-polarized pump (e). The incident angle is about 40 °. The position of the pump beam in images (a) to (d) corresponds to labels (a) to (d) in the lower graph of Fig. 5.15. The position of the pump in image (e) is the same as in (d). Two grating lines are visible (dashed line)

as observed (Fig. 5.16(e)). On the other hand, distortions of the field lines introduce a component of E_{dc} along the Y direction which contributes to SHG and accounts for the observed two-lobe pattern (Fig. 5.16(e)). The fact that the two lobes are π-out of phase, as indicated by the far-field distribution, reveals that E_{dc} field lines have opposite directions at the two sides of the grating line. Such a conclusion is reinforced by the measurement in the second geometry, i.e. with the plane of incidence perpendicular to the grating lines and p-polarized pump beam. In this geometry, while probing the grating at an angle, the field lines are more aligned with the direction of the pump polarization on one side of the grating line than on the opposite side. Therefore, a brighter SH spot is expected on the side where the field lines are more aligned. The opposite situation is expected when reversing the angle of incidence (Fig. 5.17).

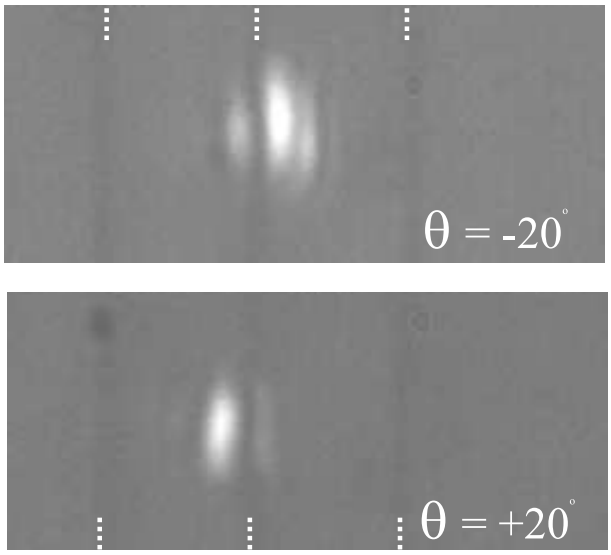

FIGURE 5.17: Images of the SH light spot recorded while probing the sample with the grating lines perpendicular to the plane of incidence and with p-polarized pump, at incident angles of $+20°$ and $-20°$. Three grating lines are visible (dashed lines).

5.5 Thermal stability of poled glasses

The second-order optical nonlinearity induced in silica by thermal poling possesses excellent long term stability in ambient conditions [7]. Charge recombination within the bulk and near the surface is responsible for the decay of $\chi^{(2)}$ which is observed when the poled glass is heated above room temperature. Since charge recombination processes are dependent on the type of mobile ionic species and the glass matrix, the decay behaviour is expected to vary with glass composition. To what extent $\chi^{(2)}$ is stable in poled glass is not only a fundamental aspect of glass poling physics but it should be taken into account in the design of devices. In this section a dramatic enhancement of the stability of $\chi^{(2)}$ for specific glass compositions is reported and its physical origin is discussed. Glass samples included Herasil 1 commercial silica from Heraeus Quarzglas GmbH., NA35 commercial glass (66.8 SiO_2, 10.1 B_2O_3, 9.7 Al_2O_3, 2.1 MgO, 5.8 CaO, 2.6 SrO, 2.6 BaO, 0.2 As_2O_3, 0.1 Sb_2O_3, in %mol) from NH Techno Glass Corp., and SA experimental glass (68.6 SiO_2, 15.6 Al_2O_3, 0.5 MgO, 15.2 ZnO, in %mol) from Nippon Sheet Glass Co. Ltd. (Table 5.2). All glasses contained alkali ions, among which sodium is known to possess high mobility in silica at elevated temperatures[178]. Herasil samples ($25 \times 25 \times 0.5$ mm) had sodium as impurity (10^{-4} %wt); NA35 samples ($20 \times 30 \times 0.7$ mm) had 0.07 %mol of Na_2O as impurity; SA2, SA3 and SA4 samples ($20 \times 30 \times 1.0$ mm) were doped with an alkali oxide (Na_2O, Li_2O and K_2O respectively) in 0.07 %mol concentration and SA1 did not contain dopant. All SA samples contained additional Na_2O (~ 0.08 %mol) which was unintentionally incorporated from SiO_2 raw material. Thermal poling was carried out in air inside an oven at an applied voltage of 4 kV using pressed-contact electrodes ($6 \times 9\,mm^2$) made of stainless steel. For each glass, preliminary poling experiments were first carried out in order to determine the

optimal values of temperature and time that maximize the second order nonlinearity in the poled samples (these values were then chosen for poling the samples of the present study. Table 5.2). These experiments revealed that the ionic conductivity was lower in

Sample	T_p (C)	t_p (min)	E_{a_1} (eV)	E_{a_2} (eV)	$\tau_{1,\mathrm{RT}}$ (day)	$\tau_{2,\mathrm{RT}}$ (day)
He1	280	10	0.62	0.79	2.1×10^1	1.3×10^4
NA35	420	30	1.22	2.04	9.2×10^6	2.9×10^{14}
SA1	350	30	0.85	1.40	9.4×10^3	1.0×10^9
SA2	350	30	0.60	1.15	6.9×10^1	1.2×10^7
SA3	350	30	1.09	1.38	2.7×10^5	6.8×10^8
SA4	350	30	1.21	1.53	2.0×10^6	7.6×10^9

TABLE 5.2: Samples under test: HE1 (flame-fused silica); NA35 (alumino-borosilicate), SA1-4 (alumino-silicates); poling temperature (T_p); poling time (t_p); activation energies of fast and slow relaxation processes associated with the decay of $\chi^{(2)}$ (E_{a1}, E_{a2}); room-temperature extrapolated decay time constants ($\tau_{1,\mathrm{RT}}$,$\tau_{2,\mathrm{RT}}$). Glass chemical compositions are given in the text.

SA (NA35) glasses than in silica, with the consequence that higher temperatures and longer times were required to pole them (Fig. 5.18). Thicknesses of nonlinear layers were determined for typical poled samples using the stack Maker's fringe technique [38] or etching technique [179]. Despite the significantly different poling conditions and chemical composition, the level of $\chi^{(2)}$ was found for all the glasses in the same range as silica. For isothermal annealing experiments, the poled samples were put on a large aluminum block inside the oven, with their cathodic surface in contact with the block, for a reason which will be explained later. This arrangement ensured that the samples rapidly reached thermal equilibrium at a temperature that was fixed by the block and, thanks to the high heat capacity of the latter, did not fluctuate during loading of samples. For silica, we calculated that the temperature of the sample, given its dimensions, reached steady-state with a time constant of the order of one second. The closed space of the oven ensured that the temperature did not fluctuate significantly during annealing. Second-harmonic generation was probed in the poled samples after each annealing period using p-polarized pump light from a mode-locked and Q-switched Nd-YAG laser ($\lambda_p = 1.064\,\mu$m), at a fixed incident angle ($\vartheta_{ext} = 60°$) and at nine locations across the poled area. Since the thickness of the nonlinear layer (L) was lower than the coherence length in all samples, the second-harmonic power ($P^{2\omega}$) was proportional to $(L \times \chi^{(2)}_{33,\mathrm{av}})^2$, where $\chi^2_{33,\mathrm{av}}$ is the spatially averaged nonlinear coefficient. Before annealing and after an annealing time t, we measured the SH power at a fixed angle and calculated $[(P^{2\omega}(t)/P^{2\omega}(0))^{1/2}]$, i.e. the quantity of interest, which is equal to $\chi^{(2)}_{33,\mathrm{av}}(t)/\chi^2_{33,\mathrm{av}}(0)$ if L does not change during annealing. The decay of the nonlinearity

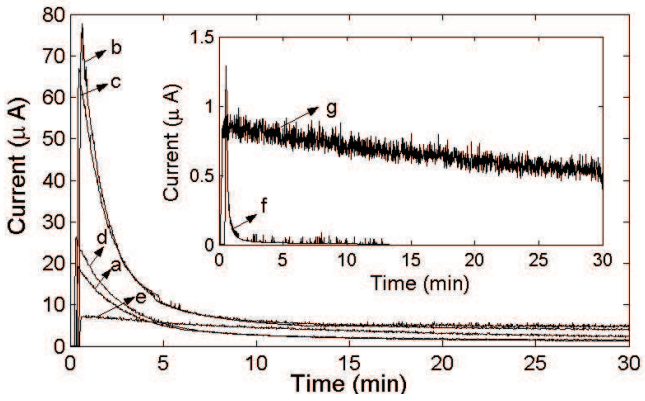

FIGURE 5.18: Current as a function of time during poling of SA1 (a) and (g), SA2 (b), SA3 (c), SA4 (d), NA35 (e) and HE1 (f). Poling temperatures: 350 °C (a-d), 420 °C (e), 280 °C (f, g).

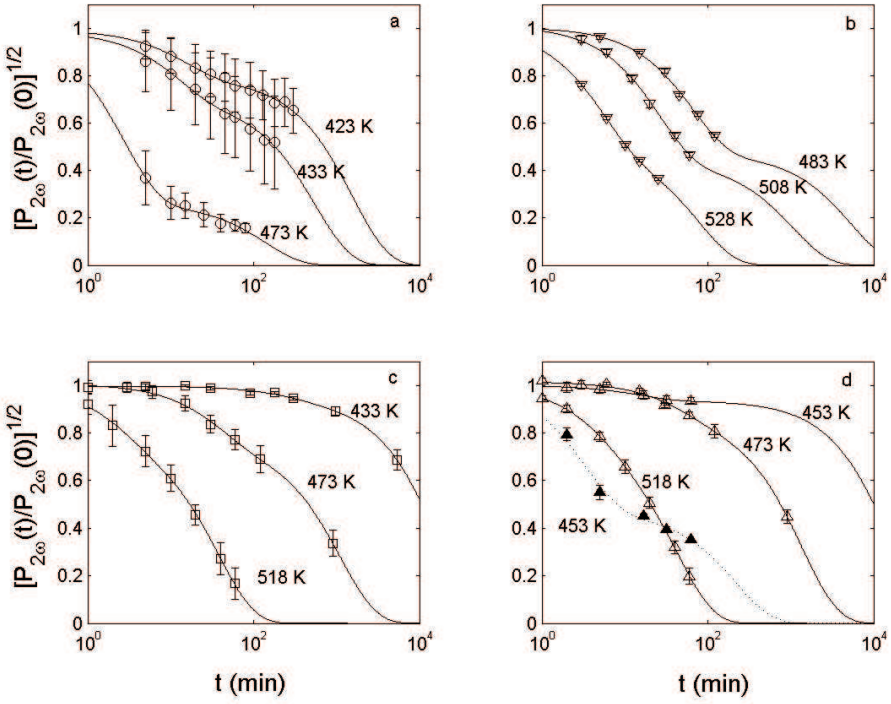

FIGURE 5.19: Decay of the second-order nonlinearity ($\chi^{(2)}$) as a function of annealing time in poled samples: HE1 (a), NA35 (b), SA3 (c) and SA1 (d). Lines are best fits to data using the sum of two exponential functions. Annealing temperatures are indicated next to decay curves. Error bars indicate standard deviations of the measured quantity. The cathodic surface of the sample was put on a metallic block in the oven [except for dashed curve in d: in this case the anodic surface was put on the block].

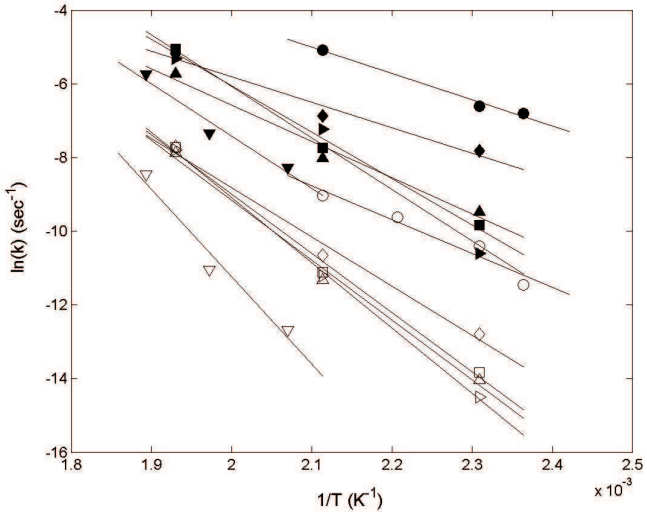

FIGURE 5.20: Decay rate (k = $1/\tau$) as a function of the reciprocal absolute temperature. Samples: HE1 (∘), NA35 (▽), SA1 (△), SA2 (◊), SA3 (□), SA4 (▷). Open (closed) symbols: decay rates associated with slow (fast) relaxation processes. Lines are best fits to Arrhenius law.

was recorded at different temperatures as a function of the annealing time (Figure 5.19). In SA and NA35 glasses, the nonlinearity started to decay at higher temperatures than in silica, so that enhanced stability could be anticipated for specific glass compositions. Although the decay curves could not be fitted successfully in the whole annealing time range using single exponential functions, data could be nicely fitted using the sum of two exponential functions with largely different time constants, i.e.

$$f(t) = a_1 \times e^{\frac{-t}{\tau_1}} + a_2 \times e^{\frac{-t}{\tau_2}} \quad . \tag{5.5}$$

From a phenomenological point of view, it means that two independent decay processes, a fast one (1) and a slow one (2), took place during annealing. Physically the two decay processes could be associated with migration of cations of different mobility which recombine with immobile negatively-charged sites, or with charge recombination (whatever the charge carrier is) in a near-surface layer, on one hand, and in a deeper layer within the bulk, on the other hand. Irrespective of which physical process is actually at play, it should be thermally activated. Indeed, the decay rates of both processes were found to follow the Arrhenius law:

$$k = A \times e^{\frac{-E_a}{k_B T}} \quad , \tag{5.6}$$

where E_a is the activation energy, A is the frequency factor, T the absolute temperature, and k_B the Boltzmann constant (Figure 5.20). The corresponding activation energies and frequency factors were determined, from which decay time constants at room temperature (RT), $\tau_{1,\mathrm{RT}}$ and $\tau_{2,\mathrm{RT}}$, were extrapolated (Table 5.2). By extrapolating the

dependencies of relative strengths a_1 and a_2 on temperature, we could infer which of the two decay processes is likely to be dominant at room temperature. The fast decay process was found to be negligible at room temperature in HE1 and SA1 samples, i.e. $a_1(T = 293\,^\circ K) \ll a_2(T = 293\,^\circ K)$. For these glasses,$\tau_{2,\mathrm{RT}}$ gives a good approximation of the nonlinearity lifetime. In Herasil silica (HE1), $\tau_{2,\mathrm{RT}}$ is one order of magnitude lower than previously reported lifetime values [180]. This is not a too large discrepancy, taking into account that extrapolation of values is very sensitive to uncertainties in E_a and A. In SA1 glass, $\tau_{2,\mathrm{RT}}$ is five orders of magnitude higher than in silica, which constitutes a dramatic enhancement of the stability. For the other glasses, values of a_1 and a_2 in the annealing temperature range did not allow us to infer which process is dominant at room temperature and, therefore, lifetime should have a value between $\tau_{1,\mathrm{RT}}$ and $\tau_{2,\mathrm{RT}}$. Even in the worst case, lifetime is several orders of magnitude higher in NA35 and SA glasses than in silica. The activation energies, E_a, of the $\chi^{(2)}$ decay, are higher in SA and NA35 glasses than in silica (Table 5.2).

The activation energies of ionic conductivity (E_σ) are higher, as well (Figure 5.18). We explain the enhancement of $\chi^{(2)}$ stability in SA and NA35 glasses with respect to silica by the strong decrease of the alkali ion mobility. Ion mobility in glasses is determined by several factors. According to the Anderson-Stuart model, E consists of two terms: the bonding energy (ΔE_b) and the elastic strain energy (ΔE_s), i.e. $E_\sigma = \Delta E_b + \Delta E_s$[181]. The first term arises from the direct Coulomb interaction between alkali ions (R^+) and charge-compensating (CC) sites. The second term arises from the distortion of the glass network as R^+ jumps from one site to the next. Substitution of Si by Al or B decreases ΔE_b because the negative charge is less localized on AlO_4^- or BO_4^- CC sites than on non-bridging oxygen (NBO) CC sites and, therefore, Coulomb interaction with R^+ is weaker [182]. On the other hand, substitution of Si by Al or B increases ΔE_s due to the increase of the network rigidity [182]. Substitution of Si by B increases further ΔE_s due to the increase of the network packing density [182]. In sodium trisilicate ($Na_2O{\cdot}3SiO_2$), the net result is a decrease of E_σ with increasing Al or B substitution [182]. SA and NA35 glasses, on the other hand, differ from sodium trisilicate by their very low alkali content and the presence of interstitial modifier cations (Zn_2^+, Mg_2^+, Ca_2^+, etc.). These larger cations encroach on the conduction pathways of alkali ions, leading to an additional increase of ΔE_s. The net result is an increase of E_σ in SA and NA35 glasses with respect to silica [178] because of (1) the presence of interstitial modifier cations, (2) the higher rigidity of the network (Al and B substitution), (3) the higher network packing density (B substitution only). This decrease of the alkali ion mobility is responsible for the higher values of E_a associated with enhanced stability of $\chi^{(2)}$. Other interesting effects were observed in annealing experiments. Before annealing, SHG was reasonably uniform in all the samples but, surprisingly, it became strongly non-uniform in HE1 samples after annealing [see error bars in Fig. 5.19(a)]. The existence of an hydrated near-surface layer, which poled differently than the bulk, could be responsible for the non-uniform decay and explain why the values of E_{a1} and E_{a2} for HE1 are lower than

the value of 1 eV reported for thermal dissociation of Na^+ in silica[178]. Which surface of the poled sample (cathodic or anodic) was put on the metallic block in the oven turned out to have a strong influence on the observed decay (Fig. 5.19(d), curves at 453 °K). This effect is attributed to the existence of near-surface charges in the poled sample (i.e. when the anodic surface is put on the metallic block, conductive paths are provided for charge escape/injection from/to the sample, which results in faster decay).

In conclusion, order of magnitude enhancement of the stability of $\chi^{(2)}$ was found in alumino-silicate and alumino- boro-silicate with respect to silica and explained in terms of drastic changes of the alkali ion mobility with glass composition.

5.6 Choice of the poling method and of the glass for frequency doubling in optical fibres

In this section each poling method is reviewed and critically discussed in view of the fabrication of a frequency doubler based on periodically poled optical fibres. To this extent, the most important criteria considered are the reproducibility of the results and the stability of the nonlinearity.

Even before the discovery of thermal poling, the creation of a self-organized QPM grating in optical fibres by photoinduced SHG showed that glass based frequency doublers were feasible. Nonetheless, even though the length of the self-organized grating can be as long as $\sim 1\,\mathrm{m}$, (but not longer, being limited by the chromatic dispersion and phase modulation [183]), optical poling is unfortunately not suitable for applications because of the low level of the induced nonlinearity ($\chi^{(2)} \sim 10^{-3}\,\mathrm{pm/V}$). Therefore this method was not pursued in this thesis as a viable solution for practical devices.

The value of nonlinear coefficient induced by UV-poling in fibres and glasses is claimed to be much higher than that obtainable by thermal poling and it is comparable with the nonlinear coefficient of second-order nonlinear crystals. With such figures, extremely competitive electro-optic modulators and wavelength converters based on periodically UV-poled fibres should have been realized. Such devices, though, have yet to come on the market, implying that there is a general lack of knowledge of the parameters critical for UV-poling. Besides the value of the nonlinearity, some issues are still open. The recent discovery of cristobalites of micron size in the UV poled samples seems to imply that poling induced losses are expected in the optical fibre. Also, it is known that the nonlinearity induced in glass by UV poling is subject to a decay with time. From all these results, we conclude that, at this stage, UV poling is not a reliable alternative method of poling for the purpose of making devices.

Electron beam poling is proved to induce nonlinearities in the glass as large as the nonlinearities induced by thermal poling. The major drawback of this method is prob-

ably the high cost. The UV-fs poling technique presented earlier in this chapter is still at the development stage and more experiments are required in order to assess whether $\chi^{(2)}$ values higher than the one produced by thermal poling are possible. A more established technique is corona poling which can produce nonlinearity values of approximately 1 pm/V [160]. Nonetheless these values are not stable and the nonlinearity decays. Therefore, in the literature a poling method as reliable as thermal poling and that can produce $\chi^{(2)}$ values larger than $\sim 1\,\mathrm{pm/V}$ does not exist. Hence, at this stage, thermal poling is the best poling method for the purpose of making devices.

Beside the value of the induced second-order nonlinearity, coupling loss, propagation loss and damage threshold are the most important parameters against which the choice of the glass or pre-treatment have to be made. From this point of view silica is an ideal host for a device. Consequently, the choice of a different material for poling would probably come from a trade-off between improved nonlinearity and poorer performance in terms of loss or maximum power sustainable. Glasses with $\chi^{(3)}$ higher than silica are promising because the induced $\chi^{(2)}$ is proportional to the third order nonlinearity. Though, these higher second-order nonlinearities have not materialized, yet and moreover, high $\chi^{(3)}$ glasses have also higher index of refraction n compared to silica, thus facing higher coupling loss. Furthermore, according to eq. (2.37) the conversion efficiency for SHG scales as d^2/n^3. Hence, what is gained in terms of improved nonlinearity has to compensate for this factor, too. Silica doped with nanocrystals or metal nanoclusters can be in principle attractive, as the $\chi^{(3)}$ of the glass host can be enhanced hundreds of times. Unfortunately this is often a resonant phenomenon and it is usually associated with a resonant absorption. Exposure of silica to γ-ray, among glass pre-treatments, did not produce enhancement of the nonlinearity in both fused and synthetic silica. We were unable to reproduce the results by Tanaka et al. [176]. Silica pre-treatment by exposure to femtosecond pulses was proved to enhance the ability of the glass to sustain the electrostatic field induced by thermal poling. This novel technique makes it possible to achieve structural modification in the glass with micro-scale resolution. The technique was used for the fabrication of a $\chi^{(2)}$ grating with a $20\,\mu$m period. Further experiments are necessary in order to prove this technology also in fibres. The loss induced by the structural modifications of the glass might be an issue.

Although many research efforts have been made in order to find new poling methods and better glass compositions, thermal poling of silica glass is at the moment the most reliable technique to induce permanent second-order nonlinearity in optical fibres. The value of the second-order nonlinearity typically induced in bulk fused silica is $\chi^{(2)} = 0.7\,\mathrm{pm/V}$ and in optical fibres is normally $3-4$ times smaller. It is the subject of the following chapters to show how the choice of the fibre design and the technology for the fabrication of long $\chi^{(2)}$ gratings could compensate for the relatively low value of the nonlinearity.

Chapter 6

Fibre Design

In the previous chapter, the choice of the poling methods and glass host for a poled device was discussed. Thermal poling as the poling method and silica as the ideal medium for a poled fibre device have been chosen. This chapter is devoted to the design of the silica fibre. The fibre's parameters, such as numerical aperture, dimensions, geometry (D-shape, twin-hole, silica core and depressed cladding or even holey fibre), and the grade of silica (high purity silica, fused silica) have to be chosen in order to maximize the performance of the device bearing in mind the specific application. Moreover, the fibre has to satisfy some practical issues: it has to be easy to manufacture, it should be mechanically stable and easy to handle and has to be compatible to standard telecom fibres. Throughout this chapter wavelength conversion as the target application will be considered, although most of the issues are common also for other applications such as for electro-optic modulation.

A figure of merit for a poled device, depending only on material properties, was previously introduced in order to compare the different types of glasses (eq. (2.38)). In order to assess the fibre design, the dependence upon the guiding properties is made explicit here through the A_{ovl} term, that was defined in chapter 2 as $1/I_{\mathrm{ovl}}$ (eq. 2.32):

$$\mathrm{FOM} = \frac{\left|d_{\mathrm{eff}}^{\mathrm{SH}}\right|^2 L^2 P^{\omega}}{\alpha n^3 A_{\mathrm{ovl}}} \tag{6.1}$$

At a first glance the parameters that have to be optimized by a proper fibre design, are identified. In the first place the nonlinearity, $d_{\mathrm{eff}}^{\mathrm{SH}}$, is affected by the core and cladding glass composition as on this depends the efficiency of the poling process. This aspect is discussed in section 6.1.

The second parameter that would benefit from a proper fibre design is A_{ovl} that is in general smaller the higher is the numerical aperture of the fibre. Though, the choice of the numerical aperture must be a trade-off among several aspects. The NA depends upon the germanium concentration in the core and upon the core size and therefore influences

both the poling process and the overlap between core and nonlinearity. Core size and NA determine the cut-off wavelength which is typically set by the specific application. Finally, the numerical aperture governs the confinement of the propagating modes and it affects the transmission losses when an interface is placed close to the core as is the case in twin-hole and D-shape fibres. All these issues are discussed in section 6.2.

In bulk glass, the type of glass and poling conditions determine the final value of the induced nonlinearity. Yet, when it comes to a waveguiding structure, the overlap between the core and the region where the nonlinearity is located, must be ensured by a proper fibre design (section 6.3).

Finally, the specific applications will pose constraints on the pump power P^{ω}, on the device length and on the acceptance bandwidth.

6.1 Core/Cladding Composition

Different grades of silica can be fabricated and pulled into fibres. They typically differ in the OH and impurities content. The glass used in standard telecom fibres is synthetic silica produced by MCVD (Modified Chemical Vapor Deposition). This process produces extremely high purity silica. This type of silica glass is highly desirable for optical telecommunications because, owing to the low impurities content and the low OH content, guarantees transmission losses as low as 0.2 dB/km at 1550 nm. On the other hand such a glass is not prone to poling. Nonlinearities are typically 10 times lower in high purity glass than in fused silica glass [7]. Fused silica glass, such as Herasil (from Heraeus) is made by flame or electric fusion of quartz. As a result of this process the amount of impurities is higher, around 1 ppm of sodium impurity compared to synthetic silica like for instance the Suprasil 300 that has a sodium content of 0.05 ppm [165]. Also slightly higher is the OH content which is around 150 ppm [165]. Both the higher amount of impurity and the higher OH content contribute to the higher poling efficiency of fused silica glass compared to high purity silica [80, 184]. The drawback of using fused silica glass for devices based on periodically poled fibre would be the enhanced transmission losses, but since the poled devices are relatively short ($\simeq 0.1 - 1$ m), such a poorer performance is well accounted for by the approximately 10 times higher induced nonlinearity. Silicate glasses such as Sodalime, with even higher Na content (20%), could be used. On the other hand, although such a glass can be efficiently poled, at the same time the induced nonlinearity is less stable and therefore not useful for a device [10]. It was found that poled fused silica is stable for more than 30 years (see section 5.5). If this lifetime is considered too short for the specific application, other glass systems should be considered. The choice should fall onto the alumino-silicate glasses and the commercially available alkali-free glass, NA35, that have been presented in Section 5.5. Such a glass systems have been shown to exhibit much longer stability than fused silica.

Furthermore, it has already been demonstrated that a ring of boron, a major component of the NA35 glass, surrounding the anode in a twin-hole fibre increases the stability of the nonlinearity [127].

Another factor is the germanium content in the core. It was found by Faccio et al. that the Na ions tend to accumulate around the core/cladding interface instead of passing through it [185]. This detrimental effect is expected to be higher for higher concentrations of germanium in the core and therefore for high NA fibres.

6.2 Numerical Aperture

From the above considerations a content of germanium as low as possible seems to be desirable. On the other hand, the amount of germanium affects the index of refraction of the core and ultimately the guiding properties of the waveguide. A first constraint is given by the specific application which sets the operating wavelength of the device. For instance, single mode operation at telecom wavelengths requires a cut-off wavelength around 1300 nm. NA and core radius have to be chosen accordingly. Since the nonlinearity induced by thermal poling extends typically about 10 μm below the surface in contact with the positive electrode, it is reasonable to assume an electrode-core distance of no more than 4 μm (edge to edge) and a core radius (a) not bigger than 2 μm. The constraint on the NA is then given by:

$$\mathrm{NA} = \frac{\lambda_{\mathrm{cut-off}} \times V_f}{2\pi \times a} > \frac{1.3\,(\mu m) \times 2.405}{2\pi \times 2\,(\mu m)} > 0.25 \tag{6.2}$$

where V_f is the V number.

Finally there is a further reason in support of the use of a relatively high NA fibre: the power density $I_{\mathrm{MAX}} = P^{\omega}/A_{\mathrm{ovl}}$ is higher for the same pump power compared to low NA fibre owing to the better confinement of the modes thus contributing to improve the figure of merit defined in eq. (6.1).

6.3 Fibre Geometry

As was mentioned in the previous sections, for a maximum interaction between the dc field recorded through poling and the optical field of the light travelling in the core, the distance between the anode and the core has to be only of a few microns. Standard fibres do not accomplish this requirement and special fibres have to be designed specifically for poling. Two alternatives have been considered so far: D-shape fibres and Twin-Hole fibres.

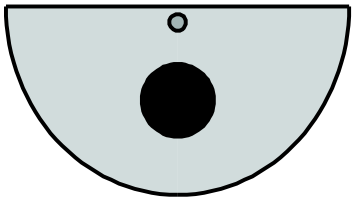

FIGURE 6.1: Schematic of D-Shape fibre

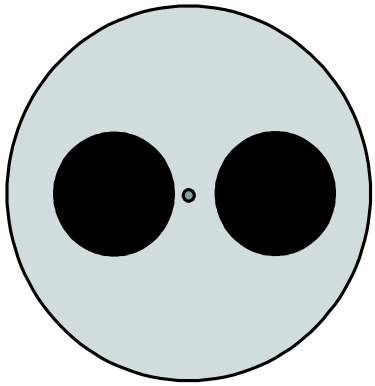

FIGURE 6.2: Schematic of Twin-hole fibre

6.3.1 D-shape Fibres

One can operate close to the core by making use of D-fibres. These have a half-circular shape, where the core is placed very close to the flat surface, Fig. 6.1. The anode electrode can then be fabricated on the flat surface using photolithography. From the reproducibility point-of-view, D-fibres can lead to useful devices [186]. In fact, high wavelength conversion efficiencies, larger than 20%, have been demonstrated at the ORC using periodically poled D-fibres [12]. However, because of the photolithographic process, periodically poled devices based on D-shape fibres are inherently limited to lengths of about 10 cm. Also, the presence of an open-air electrode leads to breakdown limitations when the high voltage for poling is applied. For this reason, poling has to be performed in vacuum although it is known that poling in air is about 3 times more efficient [82]. Furthermore, from a practical point of view, splicing can be extremely problematic. The lack of symmetry of the fibre makes it difficult to cleave straight and reproducibly. The potentialities of this type of fibre have all been exploited in the previous works and we do not see a way to achieve the necessary significant improvements in the conversion efficiency in periodically poled devices. Therefore, an alternative solution has to be found and this brings us to consider the Twin-Hole fibre design.

6.3.2 Twin-Hole Fibres

A Twin-Hole fibre is a fibre with two holes running parallel to the core (Fig. 6.2). Such a fibre geometry allows for two electrodes to be inserted in the holes. The use of twin-hole fibres with internal electrodes is very advantageous when it comes to applying high voltages during poling. The electrodes are surrounded by silica glass, which is an excellent insulator. This makes poling in vacuum no longer necessary, thus simplifying the whole process. Poling in air is in general more reliable than poling in vacuum. It is faster, as extreme vacuum ($\sim 10^{-8}$ atm) is not necessary. It is typically more uniform

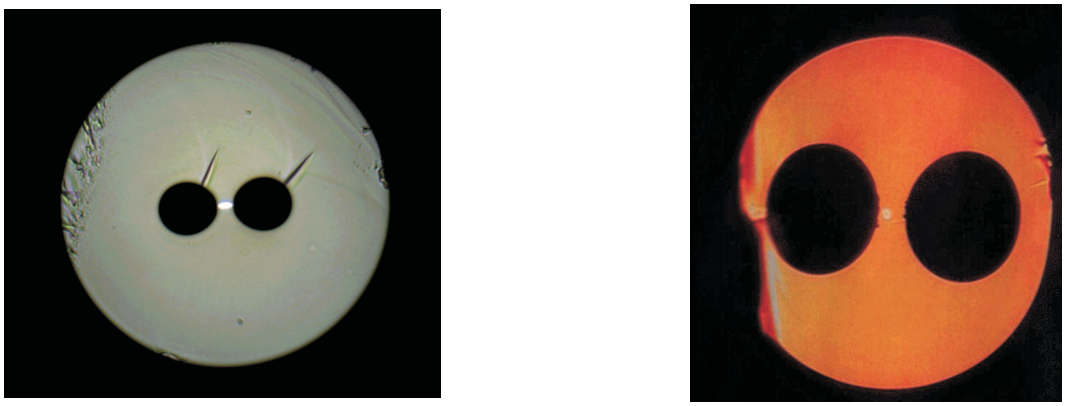

FIGURE 6.3: Images of twin-hole fibres fabricated in the in-house facilities of the ORC. *(Left)* ORC-1 fibre. *(Right)* ORC-2 fibre

across the poled area and it is more effective. The electrodes could be made by metallic wires inserted into the holes (In this case uniformity issue might arise due to the random position of the wire within the hole). Metal alloy electrodes have also been demonstrated and a length of 3 m with continuous electrodes has been obtained [130]. Since the poling is uniform along the length of the fibre and patterned comb electrodes cannot be easily fabricated (Myren et al. (2004) recently demonstrated that periodic comb electrodes in twin-hole fibres can be made by laser ablation of a metallic layer deposited on the inner surface of the holes), it is necessary to resort to techniques for periodic erasure of the nonlinearity. This topic will be discussed in the following chapter.

6.4 Fibre Fabrication

The fibres required for the fabrication of the frequency doubling fibre device were produced in the in-house facilities of the ORC[1] (Fig. 6.3). According to the previous discussion, the aim was towards a twin-hole fibre of 125 μm in diameter to be compatible with the standard telecom fibre (SMF28)and with 50 μm holes where the electrodes could be inserted. The edge to edge separation between holes was chosen to be 10 μm and the edge to edge separation between core and the closest hole was chosen to be 2 μm. The cladding was made in Heralux WG^{TM}, a fused silica glass nominally identical to Herasil 1^{TM} and produced by the same manufacturer. The desired NA was 0.32. These specifications proved to be extreme conditions for the fibre pulling. The presence of the holes breaks the circular symmetry of the fibre and if they are not accurately pressurized during pulling the core tends to be elliptical owing to the different speed of the glass flows in the direction of the holes and in its perpendicular. The first fibre fabricated (ORC-1) resulted with a very elliptical core (Fig. 6.3 left). This issue was almost

[1]The twin-hole fibres have been fabricated by Andrew Webb from the Silica Group at the Optoelectronics Research Centre

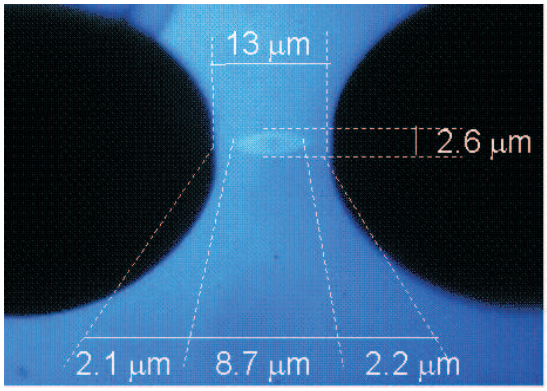

FIGURE 6.4: Close-up of the ORC-1 fibre. Note the ellipticity of the core due to the non optimized pressurization of the holes during pulling. The germanium dip is also visible in the centre of the core

	ORC-2
Composition	Ge-doped silica [GeO_2=16.8%] fused silica cladding [$\delta n = 0.023$]
Fibre diameter (μm)	125
Core Diameter (μm^2)	3×3.3
Hole to Hole Separation (μm)	10 ± 1
Hole to Core Separation (μm)	1.7
Cut-off (μm)	1.121/1.198
NA	0.28

TABLE 6.1: Characteristics of the ORC-2 Twin-Hole fibre fabricated at the Optoelectronics Research Centre.

completely solved in the second fibre (ORC-2, Fig. 6.3 right). Another issue is the dip in the germanium concentration in the centre of the core which is a typical feature of the MCVD process while working at high concentrations of germanium as in our case. Germanium tends to diffuse out of the core during pulling owing to the higher volatility of germanium oxides compared to silica. This phenomenon is particularly evident in the ORC-1 fibre (Fig. 6.4).

The parameters of the ORC-2 fibre which has been used for the development of the frequency doubler are shown in table 6.1.

Chapter 7

$\chi^{(2)}$-gratings for quasi-phase matching

In this chapter the design and the technology for the fabrication of the $\chi^{(2)}$-gratings in poled fibres are discussed. The twin-hole fibre geometry has been chosen, therefore, in order to fabricate the gratings for quasi-phase matching, periodic UV erasure will be used. In its simpler implementation, rather than fabricating a periodic electrode, a uniformly poled fibre is exposed to a UV beam through an amplitude mask.

The ability of UV light to erase the nonlinearity is well known in literature. This technique has been studied in connection with photoinduced SHG in fibres [135, 136] and more recently applied to thermally poled bulk glasses [80, 137, 138]. To our knowledge there has been only one implementation of this technique for periodic poling of fibres[22]. A generally accepted explanation of the phenomenon is that exposure to high energy photons leads to the release of electrons, which move through the E_{dc} field and screen it. Erasure of the nonlinearity has also been observed after exposure to high intensity pulsed visible light. In such a case the release of charges would have been triggered by multi-photon absorption [139, 140].

7.1 Physical model of UV erasure

One possible model to describe the dynamics of UV erasure was first proposed by Ouellette et al.[135] for photoinduced SHG. Thermal poling leads to the creation of a space charge separation in the glass, giving rise to a static electric field which is responsible for the $\chi^{(2)}$. According to the Ouellette model, the poled glass can be described as an RC circuit where the capacitance C is charged with charge q. On one plate of the capacitor are electrons trapped in defect states like for instance Non-Bridging Oxygen Hole Center (NBOHC, e.g. SiO^-). On the other are positive charges from the atmosphere

like for instance H^+. UV light photons possess enough energy to ionize the traps and to free the electrons which move through the electric field to restore a uniform neutral charge distribution. The current $i = dq/dt$ is proportional to the voltage in the capacitor which, in turn, is proportional to the number of remaining charges $q(t)$. In contrast to the behaviour of an RC circuit, the current will not follow an exponential decay. In this particular case, the charges are made mobile by the absorption of UV light. Therefore, the light alters the resistance of the circuit. The conductivity will be proportional to the number of ionized charges which is also proportional to the number of remaining charges. We have, then

$$i = \frac{dq}{dt} = \frac{V}{R(q)} = -\frac{q}{R(q)C} = -\frac{q^2}{C} \tag{7.1}$$

$$\tag{7.2}$$

It follows

$$\frac{dq}{dt} = -k\ q^2 \tag{7.3}$$

$$\tag{7.4}$$

and hence, using ($\chi^{(2)} \propto E_{dc} \propto q$)

$$\frac{d}{dt}\chi^{(2)} = -k\ \left(\chi^{(2)}\right)^2 \tag{7.5}$$

$$\tag{7.6}$$

The differential equation derived above describes the decay of the SON following exposure to UV light according to Ouellette's model. It can be solved imposing the initial condition $\chi^{(2)}(t=0) = \chi_0^{(2)}$ leading to

$$\chi^{(2)}(t) = \frac{\chi_0^{(2)}}{1 + k\chi_0^{(2)}\ t} \tag{7.7}$$

We performed a simple experiment to verify this model. The UV source used for this experiment was a Pen Ray Hg lamp emitting mainly at 254 nm and 185 nm. The power density on the sample (200 μm thick Herasil 1 disk poled at 280 °C, 4.1 kV, for 10 min.) was 10 mW/cm^2. The decay was followed in real time by monitoring the power $P^{2\omega}$ of the second-harmonic signal generated by shining the laser beam from a mode-locked and Q-switched Nd:YAG laser ($\lambda = 1064$ nm) on the poled disk while it was exposed to the UV light. The decay of the second order nonlinearity was then inferred according to $\chi^{(2)} \propto \sqrt{P^{2\omega}}$ (Fig 7.1). Data were normalized to the initial value of $\chi^{(2)}$ and fitted to eq. (7.7) (solid line). Fig 7.2 shows the same data plotted in log-log scale. The slope, equal to 1, and the linearity of the data suggest that the process closely follows the decay curve described by eq. (7.7).

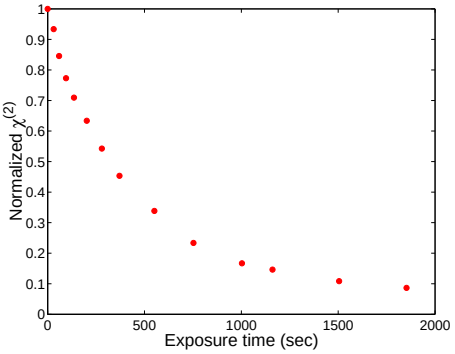

FIGURE 7.1: Decay of the normalized $\chi^{(2)}$ with exposure to UV light

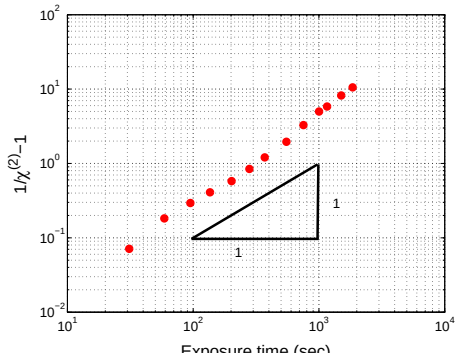

FIGURE 7.2: Decay of SH intensity with exposure to UV light in log-log scale

7.2 Assessment of periodic UV erasure in bulk glasses

Before attempting QPM in fibres we performed feasibility studies on bulk glasses. The aim was to identify the critical parameters in order to achieve high contrast, ideally 1/0 contrast, and a well defined spatial modulation.

One order of magnitude decay of the second-order nonlinearity is obtained after approximately 25 minutes exposure with the Hg-lamp. This figure could still be improved by increasing the power density of the UV light on the poled region. On the other hand, such a lamp produces light isotropically and therefore it is difficult to obtain sharp boundaries even if an amplitude mask is used to define the periodicity. For this reason we investigate erasure by exposure to the $\lambda = 244\,\text{nm}$ radiation from an intracavity doubled argon-ion laser. A silica plate (Herasil 1) 1 mm thick was poled at 280 °C, 4 kV, for 5 min using 'pressed in contact' silicon electrodes. Afterwards, the sample was exposed to the focused UV light beam from the frequency doubled Ar^+-laser mentioned above. The focused beam (spot size: $2w_0 = 130 \times 360\,\mu\text{m}^2$) was translated across the sample at constant speed to draw a line. On this line the initially uniform SON is expected to be erased. 12 parallel lines, separated by $500\,\mu$m, were erased at different speed, hence at different fluences (see Table 7.1) The sample was finally tested for SH generation by focusing the beam from a Nd:YAG laser on the poled area. The SH light was then collected with a photomultiplier and the signal visualized with an oscilloscope while the IR beam was scanning across the poled area (see Fig. 7.2). For a uniformly poled sample the SH signal would remain constant across the whole poled region. However, for this sample, the SH signal dropped whenever the IR beam was scanning across the lines that had previously been exposed to the UV light (Fig. 7.2). From left to right in the picture the lines were erased with increasing fluence. The edges of the erased lines are very sharp and, what is most important, for fluences above $\sim 10\,\text{J/cm}^2$ the erasure of the SON is total and optimum 1/0 contrast is achieved.

The effect of the close separation between erased regions, with a period very close to the one to be used in periodically poled fibres, was also studied by erasing, for each value

	Power (mW)	**Spot size $2w_0$ (μm^2)**	**Speed ($\mu m/s$)**	**Fluence (J/cm^2)**
1	5	130 × 360	2500	1.54
2	5	130 × 360	1250	3.08
3	5	130 × 360	833.3	4.62
4	5	130 × 360	625	6.15
5	5	130 × 360	416.6	9.23
6	5	130 × 360	312.5	12.31
7	5	130 × 360	250	15.38
8	5	130 × 360	187.5	20.51
9	5	130 × 360	125	30.77
10	5	130 × 360	75	51.28
11	5	130 × 360	37.5	102.56
12	5	130 × 360	18.7	205.68

TABLE 7.1: Parameters of UV erasure experiment on poled bulk silica glass

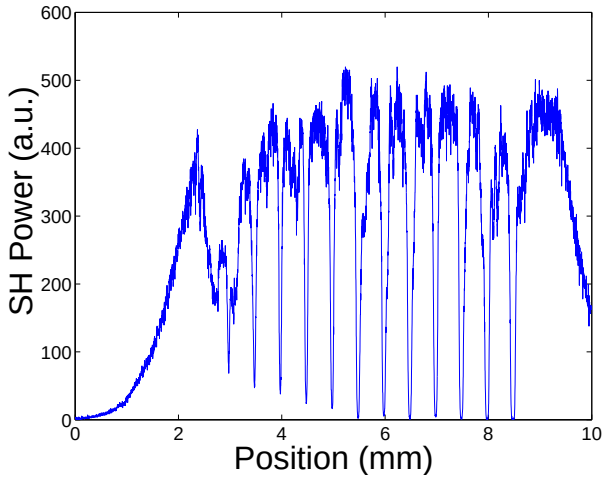

FIGURE 7.3: A uniformly poled sample (Herasil 1 silica plate, 1 mm thick, poled at 280 °C, 4 kV, for 5 min) is tested for SHG after 12 lines had been exposed to 244 nm UV radiation at increasing fluence. In this graph the SH power vs the position on the sample, while scanning orthogonally to the exposed lines, is presented. On the left the SH signal is initially zero and it increases when the pump beam approaches the poled region. Sharp drops in the SH power correspond to the exposed lines. From left to right the UV fluence is increasing. The parameters for the UV exposure are given in table 7.1

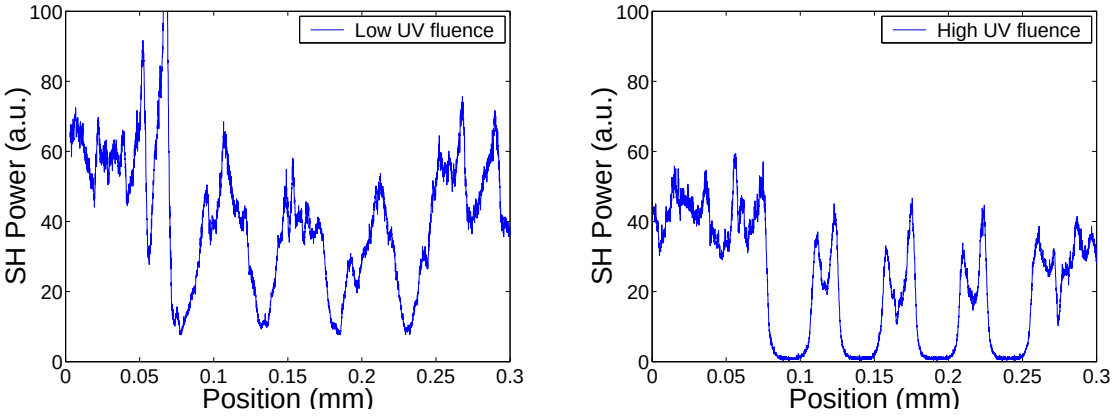

FIGURE 7.4: A uniformly poled sample (Herasil 1 silica plate, 1 mm thick, poled at 280 °C, 4 kV, for 5 min) is tested for SHG after 4 lines with 50 μm spacing between them had been exposed to 244 nm UV radiation. The SH power against the position on the sample, while scanning orthogonally to the exposed lines, is presented. (left) low fluence regime: 2.78 J/cm^2. (right) high fluence regime: 55.56 J/cm^2.

of the UV fluence, 4 lines separated by 50 μm ($2w_0 = 18 \times 360\,\mu\text{m}^2$). The results of the SH-scanning are shown for both low fluence regime, 2.78 J/cm^2, and high fluence regime, 55.56 J/cm^2 (Fig 7.2). Besides the 1/0 contrast obtained at large fluences, it is very interesting to note the change of shape of the erased region with increasing fluence. Such a feature, caused by saturation, occurs due to the complete erasure occurring earlier for the central part of the beam compared to the tail of the Gaussian intensity distribution. It suggests the possibility to have sharp boundaries at the edge of the erased region, which is highly desirable for QPM in fibre.

7.3 QPM period in optical fibres

In the first part of this chapter, periodic UV erasure was assessed and its potentiality for the fabrication of quasi-phase matching gratings was confirmed. In the following, the attention will be focused on the methods employed to determine the value of the $\chi^{(2)}$-grating period for quasi-phase matching at the desired wavelength.

For a first order QPM interaction the period, Λ_{QPM}, is given by (eq. 2.33):

$$\Delta K = \frac{4\pi}{\lambda} n_{\text{eff}}^{2\omega} + 2\frac{2\pi}{\lambda} n_{\text{eff}}^{\omega} - \frac{2\pi}{\Lambda_{\text{QPM}}} = 0 \tag{7.8}$$

from which:

$$\Lambda_{\text{QPM}} = \frac{\lambda}{2\left(n_{\text{eff}}^{2\omega} - n_{\text{eff}}^{\omega}\right)}. \tag{7.9}$$

where λ is the wavelength of the fundamental and $n_{\text{eff}} = n_{\text{eff}}(\lambda, \text{NA}, a)$ is the effective index of the propagating modes which is a function of the wavelength, the fibre numerical

aperture (NA) and the core radius a.

It has been shown that in a 10 cm long periodically poled fibre the wavelength acceptance bandwidth is approximately 2 nm (eq. 2.39). This means that the period of the $\chi^{(2)}$ gratings have to be determined and fabricated with enough accuracy so that the QPM wavelength is within 2 nm of the desired operating wavelength. A simple estimate can give us the idea of how challenging this task can be. Differentiation of equation (7.9) leads to:

$$\frac{\delta\lambda}{\lambda} = \frac{\delta\Lambda_{\mathrm{QPM}}}{\Lambda_{\mathrm{QPM}}} + \frac{\delta\Delta n_{\mathrm{eff}}}{\Delta n_{\mathrm{eff}}} \tag{7.10}$$

where $\Delta n_{\mathrm{eff}} = n_{\mathrm{eff}}^{2\omega} - n_{\mathrm{eff}}^{\omega}$. The left hand side of the equation represents the tolerances that can be accepted in the QPM wavelength, that is the bandwidth of the periodically poled fibre or the tuning range of the laser source ($\delta\lambda = |\lambda_{\mathrm{QPM}} - \lambda|$). For operation at $\lambda = 1550$ nm and for a 10 cm long device with ~ 2 nm bandwidth, this term is about 0.2%. The right hand side in eq. (7.10) represents the contribution to the errors in λ_{QPM} due to the errors in the period during the fabrication of the $\chi^{(2)}$-grating itself ($\frac{\delta\Lambda_{\mathrm{QPM}}}{\Lambda_{\mathrm{QPM}}}$) and due to the determination of the period from the fibre parameters ($\frac{\delta\Delta n_{\mathrm{eff}}}{\Delta n_{\mathrm{eff}}}$). For a simple estimate we can imagine that the two contributions are equal and must be both below 0.1%. Since Λ_{QPM} is in the range of 50 μm, the precision in the period that must be achieved in the fabrication of the $\chi^{(2)}$-grating is 25 nm. Such a precision is possible when either photolithographic methods are used to define the periodic electrode on the flat surface of a D-shape fibre or when an amplitude mask is used for periodic UV erasure. It is a very critical issue for any methods involving translation of the fibre relative to a laser beam, such as for CO_2 laser assisted periodic poling or for the continuous periodic UV erasure that will be described in the next chapter. Δn_{eff} is in the range of 0.01. It follows that the maximum error that can be tolerated in the measurement of the effective index is $\sim 10^{-5}$. However, the precision needed can be relaxed using a tuneable source: e.g. diode seeded EDFA gives about 40 nm tunability around 1550 nm. In such a case ($\delta\lambda/\lambda = 2.5\%$) the precision that we need in the measurement of $\delta\Delta n_{\mathrm{eff}}$ is 4×10^{-4}, which means $\delta n_{\mathrm{eff}}^{\omega} = \delta n_{\mathrm{eff}}^{2\omega} = 2 \times 10^{-4}$ (the error in Λ_{QPM} is negligible). It is still challenging, especially because of the sensitivity of n_{eff} on the fibre parameters. The sensitivity is even higher for the high NA fibres which are used in our experiments. So far, in the literature, a trial and error method has been employed in order to find the proper period for the specific fibre. A number of fibre samples are periodically poled with different periods in order to obtain at least one producing QPM at the operating wavelength of the laser source. This method is time consuming, and has to be repeated for each new fibre.

Here, two new and more practical methods for the determination of the desired QPM period are presented. One is based on numerical simulation and the second one on a direct measurement of the effective index of the fibre employing fibre Bragg gratings

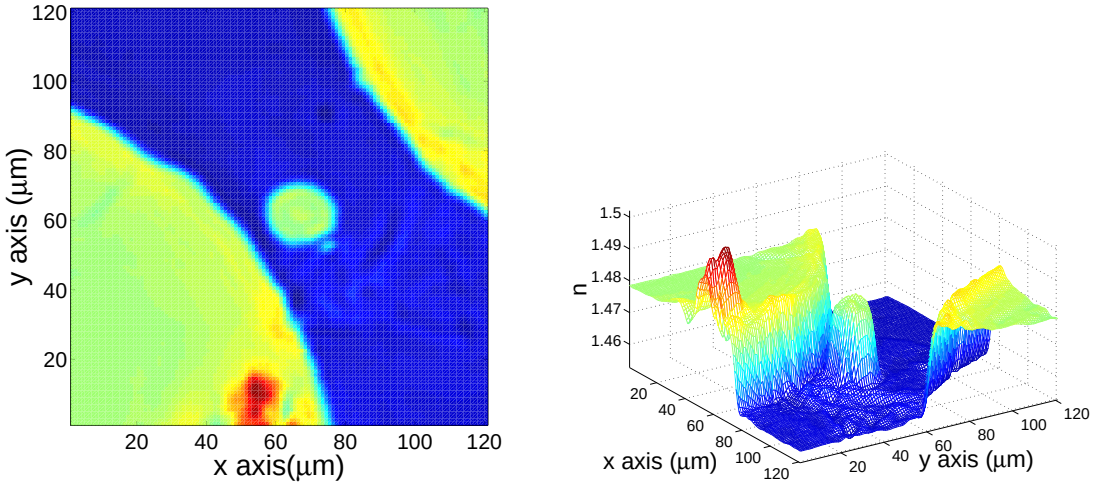

FIGURE 7.5: 2D and 3D refractive index profile of the ORC-2 twin-hole fibre fabricated at the ORC and used for this work. The apparent high refractive index in the holes is an artifact of the measurements which require the holes to be filled with an index matching fluid in order to reduce scattering from the interfaces.

(sections 7.3.1 and 7.3.2 respectively). The latter also constitutes an experimental validation of the method based on numerical simulations.

7.3.1 Numerical simulations

For the analysis we used a commercial software: Beamprop by RSOFT. The software is based on a finite difference propagation method used to solve the paraxial approximation of the Helmholtz equation. It requires, as input function, the refractive index profile at the fundamental and SH wavelength. The outline of the procedure we followed is the following: first, the refractive index profile was measured at 670 nm using an optical fibre analyzer. Then it is calculated at the fundamental and SH wavelengths, using Sellmeier's equation for Ge-doped silica. Through numerical simulations n_{eff}^{ω} and $n_{\text{eff}}^{2\omega}$ are obtained and the period necessary for QPM in our fibres is given by eq. 7.9. The refractive index distribution was measured at ACREO using the EXFO NR-9200/NR optical fibre analyzer. According to the specifications this instrument has a spatial resolution $< 0.5\,\mu$m and a refractive index resolution of 10^{-4}. The operating wavelength is 670 nm. In Fig. 7.5 the refractive index profiles of the ORC-2 fibre is given. The refractive index profiles, known at 670 nm, have to be scaled to the fundamental and SH wavelength. The dependence of the refractive index from the wavelength is typically approximated by a third-order Sellmeier's expansion:

$$n(\lambda) = 1 + \sum_{i=1}^{3} \frac{a_i \lambda^2}{\lambda^2 - b_i} \tag{7.11}$$

where a_i and b_i can be found in Table 7.2 for pure silica and Ge-doped silica.

$[GeO_2]$ (mol%)	a_1	a_2	a_3	b_1	b_2	b_3
Pure silica	0.6965325	0.4083099	0.8968766	0.004368309	0.01394999	97.93399
6.3%	0.7083925	0.4203993	0.8663412	0.007290464	0.01050294	97.93428
8.7%	0.7133103	0.4250904	0.863198	0.006910297	0.01165674	97.93434
11.2%	0.7186243	0.4301997	0.8543265	0.004026394	0.01632475	97.9344
15.0%	0.724918	0.438122	0.8221368	0.007596374	0.01162396	97.93472
19.3%	0.7347008	0.4461191	0.8081698	0.005847345	0.01552717	97.93484

TABLE 7.2: Sellmeier's equation coefficients for pure and GeO_2 doped silica glass.

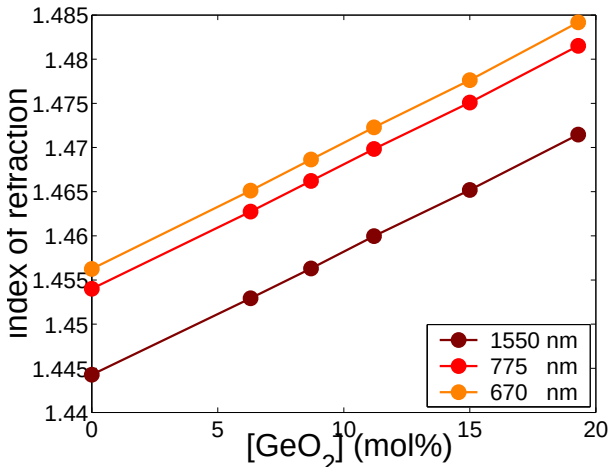

FIGURE 7.6: Index of refraction against GeO_2 concentration according to Sellmeier's equations.

A linear relationship holds between the refractive index and the GeO_2 concentration in the core. The index of refraction against the GeO_2 concentration is plotted in figure 7.6 for different wavelengths according to Sellmeier's equations. A linear fit of the data for 670 nm allows the conversion of the index profile at that wavelength into a more general $[GeO_2]$ concentration profile (the parameters of the best fitting function are found in table 7.3). Then, from the dopant concentration profile is possible to retrieve the index profile at any desired wavelength by using the Sellmeier's equations again. Besides the refractive index distribution, the physical propagation problem requires the input wave field as initial condition. In the simulation a Gaussian mode was assumed to be launched into the fibre. The calculated mode profiles and the corresponding mode effective index are given in Fig. 7.7. Λ_{QPM} is determined, according to eq. (7.9), for the ORC-2 fibre, to be 42.320 μm.

$\boldsymbol{n = n_0 + \frac{dn}{dc}[GeO_2]}$mol%	
$\lambda = 1550\,\text{nm}$	$n_0 = 1.44415 \pm 9.00 \times 10^{-5}$ $\frac{dn}{dc} = 0.001408 \pm 8.03 \times 10^{-6}$
$\lambda = 775\,\text{nm}$	$n_0 = 1.4539 \pm 1.10 \times 10^{-4}$ $\frac{dn}{dc} = 0.001424 \pm 8.98 \times 10^{-6}$
$\lambda = 670\,\text{nm}$	$n_0 = 1.4561 \pm 1.20 \times 10^{-4}$ $\frac{dn}{dc} = 0.00144 \pm 1.00 \times 10^{-5}$

TABLE 7.3: Index of refraction of Ge-doped silica at 1550 nm, 775 nm and 670 nm. Parameters of the linear fit.

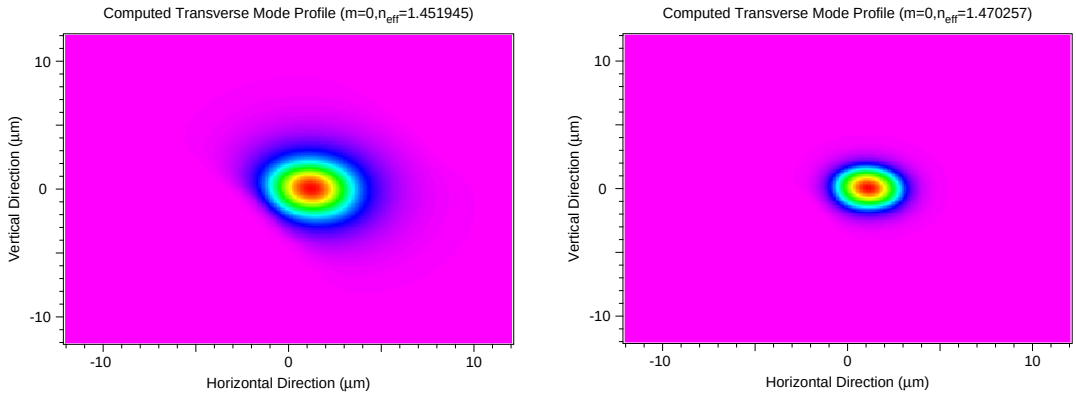

FIGURE 7.7: Mode profile of ORC-2 fibre at (left) $\lambda = 1550\,\text{nm}$ and (right) $\lambda = 775\,\text{nm}$

7.3.2 Validation of the numerical method: experimental determination of $\mathbf{n}_{\text{eff}}$

The method for estimating the effective index, presented in the previous section, relies on the accuracy of the measurements of the refractive index profile of the twin-hole fibre and on the accuracy of the numerical simulations themselves. The experimental validation of the numerical method is given in this section. The measurement of n_{eff} is obtained after writing fibre Bragg gratings (FBG) into the fibre under investigation and measuring the Bragg wavelength λ_{BG}. The Bragg wavelength is related to n_{eff} through,

$$\lambda_{\text{BG}} = 2n_{\text{eff}}\Lambda \tag{7.12}$$

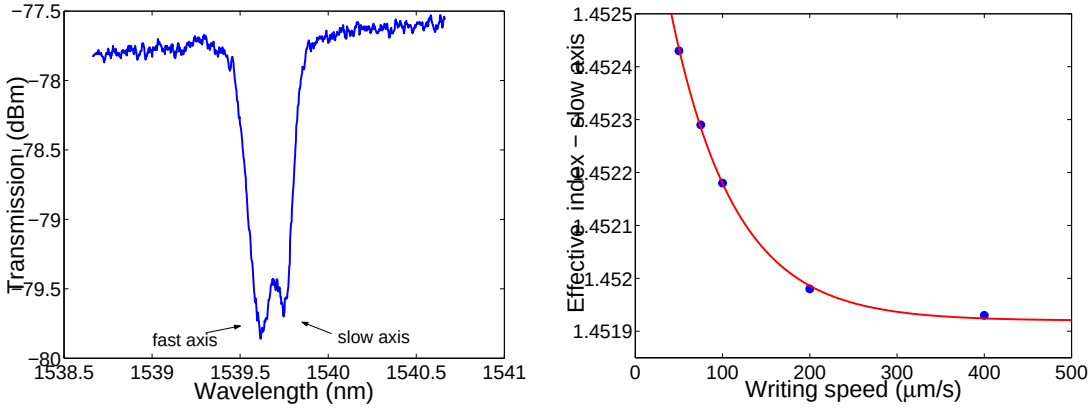

FIGURE 7.8: (left) typical transmission spectrum of a uniform fibre Bragg-grating written in the ORC-2 fibre. The two peaks correspond to the two orthogonal polarization states. The slow axis is parallel to the direction joining the holes, whereas the fast axis is perpendicular to it. (Right) Measurement of the effective index for Bragg-gratings written with decreasing fluence, that is increasing writing speed. The effective index of the fibre is the one obtained after extrapolation to zero fluence

where Λ is the period of the Bragg-grating which is half the period of the phase mask used for writing the grating. Error analysis shows that

$$\frac{\delta n_{\text{eff}}}{n_{\text{eff}}} = \frac{\delta \lambda_{\text{BG}}}{\lambda_{\text{BG}}} + \frac{\delta \Lambda}{\Lambda} \tag{7.13}$$

from which it is possible to estimate the error expected in n_{eff}. Phase masks producers are typically giving the accuracy in the pitch period in the range of 0.01 nm. The phase mask used for writing a FBG operating around 1550 nm in the twin-hole fibre had a 1060.5 nm period. The measurement of λ_{BG} was carried out using an ADVANTEST optical spectrum analyzer (OSA) which provides very good wavelength accuracy < 0.05 nm. Substituting these figures into eq. (7.13) one obtains

$$\delta n_{\text{eff}} \sim 4 \times 10^{-5} \tag{7.14}$$

which is one order of magnitude better than the minimum accuracy that is needed (see section 7.3). FBGs were written in the hydrogenated twin-hole fibre[1] and a typical transmission spectrum is given in Fig. 7.8(left). The presence of two Bragg-grating peaks when probing with unpolarized white light gives evidence of birefringence in the fibre which is a consequence of the slight ellipticity of the core (see Fig. 6.3 and table 6.1). The two modes, having orthogonal polarizations corresponding to the axis of the core, have a different refractive index (eq. 7.12). The peak at lower wavelength can be associated with the mode having lower effective index. In the case of the ORC-2 fibre this corresponds to light polarized in the direction perpendicular to the line joining the holes. This axis is also called fast axis as the light travels faster owing to the lower effective index. The mode with orthogonal polarization (slow axis) experiences a higher effective index

[1]The work was carried out by M. Ibsen from the Fibre Bragg Gratings Group at the ORC

and hence is associated with the Bragg-grating peak at higher wavelength. Since in a periodically poled fibre the efficiency is maximized when the light is polarized parallel to the poling field, that is parallel to the line joining the holes, n_{eff} has to be evaluated for the slow axis. The birefringence, measured as $n^s_{\text{eff}} - n^f_{\text{eff}}$ is equal to 1.41×10^{-4}

During the writing process a fibre placed behind a phase mask is exposed to the UV beam from a CW frequency doubled Ar^+-laser and an ideally sinusoidal index modulation is recorded into the photosensitive core. On top of the index modulation the average refractive index of the core is also raised during the process. The amount of it depends on the fluence of the UV light it was subjected to. Therefore for a precise measurement of the effective index in the unexposed fibre it was necessary to write 5 gratings at different fluences and then extrapolate the data to zero fluence. The fluence was decreased by increasing the speed of the UV beam scanning the phase mask. The effective index of the slow axis for increasing writing speed is plotted in Fig. 7.8(right). After fitting the data to an exponential decay, the n_{eff} of the unexposed fibre is found to be $1.45192 \pm 8.5 \times 10^{-6}$ at 1539.762 nm. The error for n_{eff} obtained by the fit is underestimated as the fitting routine does not take into account the (systematic) error introduced by the phase mask period that can be as large as $\sim 10^{-5}$. The figure of 4×10^{-5} derived previously (see eq. 7.14) is believed to be a more realistic estimate.

The comparison between the evaluation of n_{eff} through numerical simulation and the experimental value reported above is remarkable (Fig. 7.9(left)). From numerical simulations n_{eff} at 1540 nm is expected to be 1.45237. The discrepancy with the experimental value is only 4.5×10^{-4}, well within the error estimated for the numerical simulation method. Therefore, experimental measurements validated the method based on numerical simulations. Although the latter gives less accuracy than the FBG method, numerical predictions are sufficiently accurate to allow the determination of the QPM grating period for operation at the desired wavelength in, at most, few attempts. Moreover they are not time consuming and, once implemented, they can be used for designing purposes as shown in the next section.

The final comment is regarding the determination of the QPM grating period by the FBG method. Error analysis, reported earlier in this chapter has shown that this method is 10 times more accurate than the method based on numerical simulations. On one hand it is obvious to use the FBG method for the evaluation of Λ_{QPM} in the fibre chosen for the frequency doubler device. On the other hand, this requires a measurement of $n^{2\omega}_{\text{eff}}$. Such information could be obtained either by repeating the same procedure described for n^{ω}_{eff} but using a suitable phase mask, or more elegantly it could be retrieved from the reflection spectrum at the second-harmonic wavelength for strong FBG, i.e. written with high fluence. In the frequency domain the reflection spectrum is the Fourier transform of the grating index modulation. Ideal FBGs, with sinusoidal modulation of the index of refraction, reflect the light at the frequency corresponding to the first-order Fourier component, which is ω in our case. The optical power in the second-order Fourier

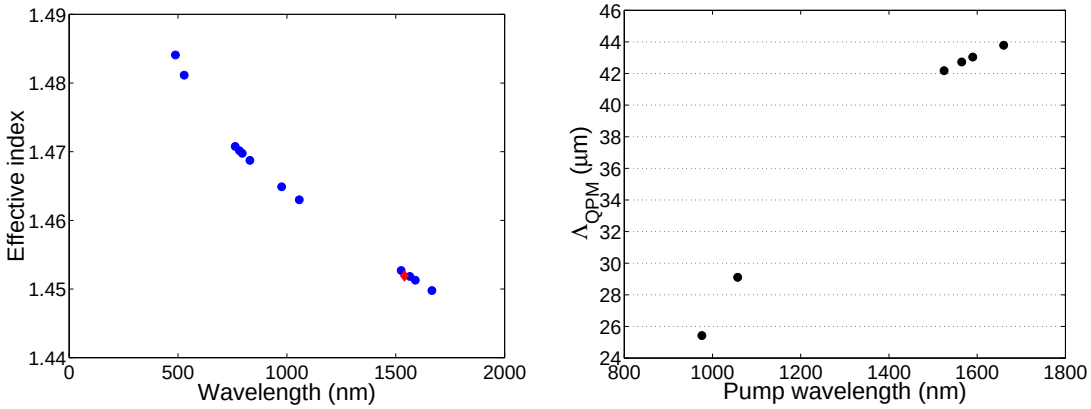

FIGURE 7.9: (Left) Simulations of the effective index against wavelength of the LP_{01} mode in the ORC-2 fibre. The red diamond point is the effective index evaluated from the FBG method. (Right) The QPM period against wavelength of the pump is calculated according to eq. (7.9)

component is zero and so no reflected light is expected at 2ω. On the other hand, when the grating is strong enough, the index modulation deviates from the ideal sinusoidal modulation, thus making it possible to have light reflected at 2ω.

We have looked for evidence of the second-order grating, but, as it is less efficient than the first-order and as the white light source was not bright enough around 2ω, we were unable to detect it. This issue could be solved, for instance, by using a tuneable Ti:sapphire laser, provided that the fundamental mode is launched into the fibre.

7.4 QPM grating period for the ORC-2 fibre

The effective index is calculated for the fundamental mode LP_{01} in the ORC-2 fibre at the wavelength of operation of a Nd-doped fibre laser (980 nm),a Yb-doped fibre laser (1060 nm) and of a tunable Er-doped fibre laser ($1525 - 1565$ nm) and at the wavelength of their second-harmonic (Fig. 7.9(left)). The period required for the $\chi^{(2)}$-grating is evaluated according to eq. (7.9) (Fig. 7.9(right)). A close-up view, centered on the C-telecom band, is shown in Fig. 7.10. The red line corresponds to the numerical simulations for the ORC-2 fibre and the two diamonds points refer to the measured experimental data from the periodically poled fibre devices fabricated during the work reported in this thesis and presented in chapter 8. Note the very good agreement between experimental data and numerical predictions.

Once in a periodically poled fibre, λ_{QPM} is associated with the corresponding grating period Λ, numerical simulations are no longer necessary for the fabrication of new devices aimed at frequency doubling of sources operating at wavelengths equal to $\lambda_{\mathrm{QPM}} + \mathrm{d}\lambda$. Provided that a linear dependence holds between λ_{QPM} and Λ, (Fig. 7.10(left)), the new

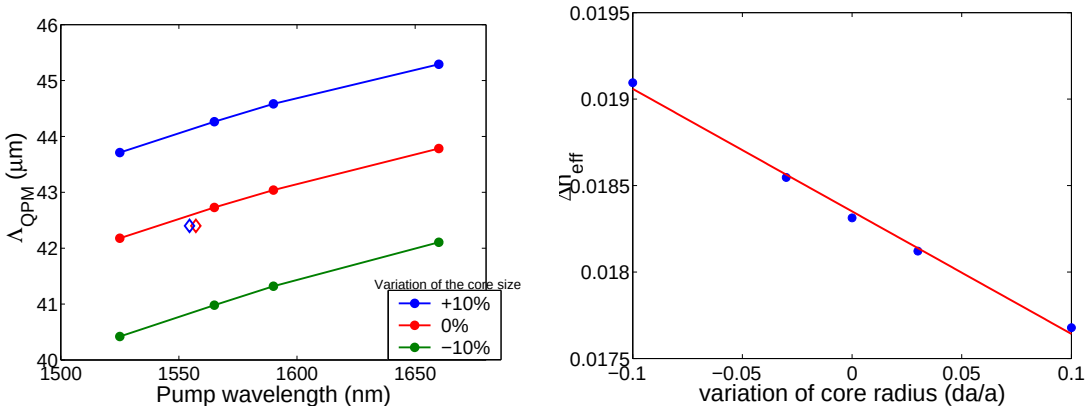

FIGURE 7.10: (Left) The QPM period is calculated for 10% increase and decrease of the core radius. The diamond symbols refer to experimental data. (Right) Δn_{eff} is calculated for different core radii at the wavelength of 1565 nm.

grating period is $\Lambda + \mathrm{d}\Lambda$ where $\mathrm{d}\Lambda$ is given by:

$$\mathrm{d}\Lambda = \frac{\partial \Lambda}{\partial \lambda}\,\mathrm{d}\lambda \tag{7.15}$$

7.5 Sensitivity of λ_{QPM} to fibre parameters

Variation on the core radius a modifies the effective index and consequently shifts the wavelength where quasi-phase matching occurs. To compensate for this effect and maintain QPM at the desired wavelength, the period of $\chi^{(2)}$-gratings have to be increased or decreased accordingly (Fig. 7.10(left)). The amount $\mathrm{d}\Lambda$ is obtained by differentiating the equation:

$$\Lambda = \frac{\lambda}{2\Delta n_{\text{eff}}\,(\lambda, a)} \tag{7.16}$$

which is the usual expression giving the QPM condition where the dependence of $\Delta n_{\text{eff}} = n_{\text{eff}}^{2\omega} - n_{\text{eff}}^{\omega}$ on the core radius a is made explicit. After differentiation one has:

$$\mathrm{d}\Lambda = -\frac{\lambda}{2}\frac{1}{\Delta n_{\text{eff}}^2}\left(\frac{\partial}{\partial a}\Delta n_{\text{eff}}\right)\mathrm{d}a, \tag{7.17}$$

where $\frac{\partial}{\partial a}\Delta n_{\text{eff}} = -0.0071 \pm 2.6 \times 10^{-4}$ is obtained from a linear fit of the data shown in Fig. 7.10(right). The increment of the core radius $\mathrm{d}a$ is expressed in normalized units. At the wavelength of 1565 nm, Δn_{eff} is computed to be 0.018313. Upon substitution of those values into eq. (7.17) one obtains that, in order to compensate for a 1% variation in the fibre size, the period for QPM must be adjusted by 165 nm. This figure highlights once more the sensitivity of the QPM conditions to the fibre parameters. In practice,

since fibre diameters in commercial fibres are given with a 1% tolerance, it means that periodically poled silica fibres fabricated in different sections of the same fibre are likely to require a slightly different period in order to operate at the same wavelength. A more important consequence is related to the fabrication of long devices. As fibre non-uniformities can cause a shift of the operation wavelength of a periodically poled fibre, the pump might lose its quasi-phase matching condition while travelling along a device. For a variation of 1% in the core size along the length of the device the λ_{QPM} is shifted by an amount equal to $\mathrm{d}\lambda = \frac{\mathrm{d}\Lambda}{13.3} = 12.4\,\mathrm{nm}$. This quantity is enough to shift the signal outside the acceptance bandwidth of a 3 cm long periodically poled device, which is 5.7 nm according to eq. (2.39).

Chapter 8

All-fibre frequency conversion in long periodically poled silica fibres

8.1 Poling

For poling, gold plated tungsten wires having 25 μm diameters were inserted in the two holes. The poled area, defined by the region where the electrodes overlapped, was, in most of the cases, 13 cm long (Fig. 8.1). The fibres were placed on top of a hot plate and poling was carried out in air by heating the fibres to 250 °C with 4 kV applied (Fig. 8.2). Cooling down to room temperature occurred in a few seconds as the heater was removed from under the fibre. After poling, the wires were extracted from the samples and the devices spliced to standard telecom fibre (SMF-28). Typical splice losses were in the range of 3 dB, for the ORC-2 fibre. The losses can be reduced by

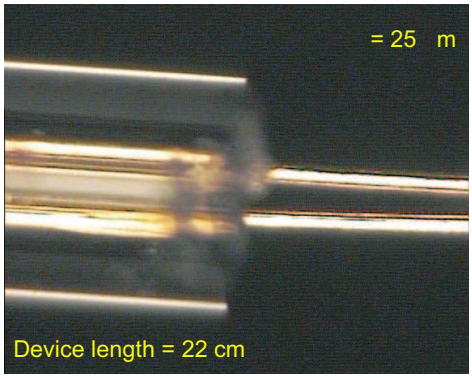

FIGURE 8.1: Gold-plated tungsten wire electrodes in a twin-hole fibre. The diameter of the wires is 25 μm

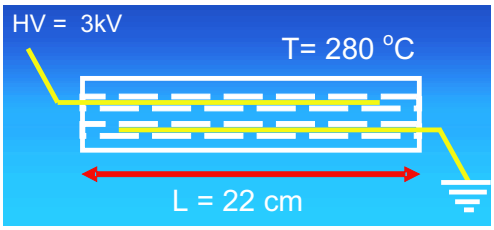

FIGURE 8.2: Schematic of the procedure for thermal poling of twin-hole fibres

improving the circularity of the core and of the fibre itself during fabrication and by using buffer fibres to compensate for the NA mismatch. The process of splicing was not optimized. The first batch of devices was aimed at the identification of the $\chi^{(2)}$-grating period for QPM in the wavelength tunability range of the fibre laser source used for characterization, i.e $1525 - 1565\,\text{nm}$. Therefore, they were poled in identical conditions and different periods were written by periodic UV erasure. The second batch of devices was aimed at periodic poling in long, up to 33 cm, devices. The third batch was aimed at optimizing the poling time for the highest nonlinearity. The fourth batch was aimed at the fabrication of periodically poled silica fibres for frequency doubling a more powerful laser source delivering up to 400 W peak power at 1537 nm. The poling conditions for all the samples that have been fabricated are summarized in table 8.1.

Reliable poling of the fibres proved to be a delicate task. The 4 kV applied proved to be close to the limit for the electrical breakdown in the fibre at 250°C. Poling at higher temperatures or higher voltage resulted, most of the times, in electrical breakdown as soon as the voltage was applied. The critical point is the edge of the overlapping between the two electrodes, owing to the higher intensity of the electric field. Reliable poling was obtained only when the overlapping region between the electrodes was made larger than the hot plate (L = 13 cm) so that the temperature at the edges was lower and the breakdown strength larger. Attempting of poling shorter devices has resulted, almost inevitably in breakdown or poor performances of the periodically poled fibres (see table 8.1 for the PPSF in batch ♯3).

8.2 Continuous Periodic UV Erasure

The $\chi^{(2)}$-gratings for quasi-phase matching were fabricated by local erasure of the nonlinearity through exposure to UV light. This technique, referred to as periodic UV erasure, was described in the previous chapter. For the first time, using the continuous Bragg grating writing system available at the ORC, no amplitude mask was used. Instead the periodic nonlinearity was created step by step, by focusing, on the core of the poled fibre, the 5 mW output from a frequency doubled Ar^+-laser ($\lambda = 244\,\text{nm}$, spot size $2w_0 = 15\,\mu\text{m} \times 350\,\mu\text{m}$) and translating the fibre relative to the focused spot with

Device	**T (C)**	**Voltage (kV)**	**time (min)**	**L (cm)**	**Comments**
		Batch ♯1			
d1-01	250	4	10	13	
d1-02	250	4	10	13	Breakdown
d1-03	250	4	10	13	
d1-04	250	4	10	13	
d1-05	250	4	10	13	
d1-06	250	4	10	13	
d1-07	250	4	10	13	
d1-08	250	4	10	13	
d1-09	250	4	10	13	
d1-10	250	4	10	13	
		Batch ♯2			
d2-01	250	4	10	28*	
d2-02	250	4	10	29*	
d2-03	250	4	10	30*	Fibre broken
d2-04	250	4	10	33*	
d2-05	250	4	10	20*	Tungsten wires
		Batch ♯3			
d3-01	250	4.1	5	5	
d3-02	250	4.1	10	8	Breakdown
d3-03	250	4.1	30	8	
d3-04	250	4.1	60	8	Breakdown
d3-05	250	4.1	5	7.5	
d3-06	250	4.1	5	8	Breakdown
d3-07	250	4.1	60	8	Temperature gradient along the fibre
d3-08	250	4.1	16	6	Temperature gradient along the fibre
d3-09	250	4.1	60	13	
d3-10	250	4.1	30	13	
d3-11	250	4.1	15	13	
d3-12	250	4.1	15	13	
		Batch ♯4			
d4-01	250	4.1	60	13	
d4-02	250	4.1	60	13	
d4-03	250	4.1	60	13	
d4-04	250	4.1	60	13	
d4-05	250	4.1	60	13	

TABLE 8.1: Thermal poling parameters. ∗: as the fibre was longer than the hot plate, three sections were poled consecutively

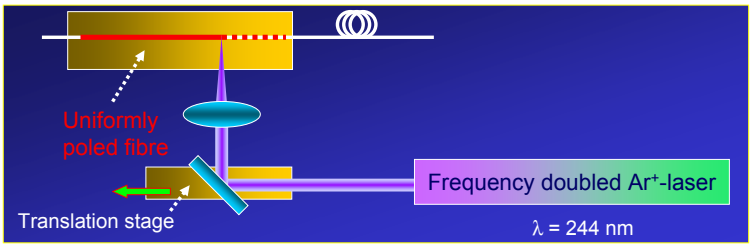

FIGURE 8.3: Set-up for the continuous periodic UV erasure

a stage. The UV light was flashed intermittently in synchronization with the movement (Fig. 8.3). QPM gratings were written in the uniformly poled fibres, aiming for frequency conversion between $LP_{01}^{\omega} \rightarrow LP_{01}^{2\omega}$ fundamental modes. The UV laser fluence experienced by the fibre core was $7.14\,J/cm^2$. The duty-cycle of the intermittent UV beam was chosen to be 20% in order to compensate for the erasure due to the tails of the Gaussian intensity distribution of the focused laser spot and to have about 50% duty-cycle on the actual nonlinear profile.

In the first batch of periodically poled fibres, all poled in the same conditions, a set of gratings with periods ranging from $41.650\,\mu m$ to $43.150\,\mu m$ was written (see Table 8.2). The range of periods was chosen according to the numerical simulations method described in the previous chapter for the measurement of n_{eff}^{ω} and $n_{\text{eff}}^{2\omega}$. After the characterization, which will be presented in the next section, the samples d1-01 and d1-06 were successfully exhibiting QPM in the range of tunability of our source and precisely at $\lambda_{\text{QPM}} = 1557\,nm$. As they were written with the $\chi^{(2)}$-grating period of $42.400\,\mu m$, the same period was chosen for all the devices fabricated afterwards. Only in batch ♯4 the grating period was modified in order to shift the wavelength of operation towards $\lambda = 1537\,nm$. Long periodically poled devices, up to 25 cm, were fabricated out of uniformly poled fibres of the second batch.

The step by step method we adopted for the $\chi^{(2)}$-grating fabrication possesses some key advantages over the use of periodic comb electrodes or an amplitude mask for UV erasure. First of all it ensures scalability to much longer length. Up to 1 m long periodically poled fibres are expected to be feasible, limited only by the uniformity of the fibre along its length. It was described in the previous chapter that even variations in the effective index as small as 1% along the fibre might severely limit the conversion efficiency because they introduce phase errors among the interacting SH waves generated in different regions along the fibre thus preventing their constructive interference. On the other hand the flexibility offered by a direct writing technique enables, in principle, to locally adapt the period of QPM grating to compensate for fibre non-uniformities. Furthermore, by dosing the fluence of the UV beam, it is possible to tailor the amount of nonlinearity to be erased enabling apodization of the QPM grating for complex wavelength tuning curves.

Device	Λ_{QPM} **(μm)**	**Duty-cycle (%)**	P^{UV} **(mW)**	**Spot size (μm^2)**	**Speed (μm/s)**	**Fluence (J/cm^2)**	**L (cm)**
			Batch ♯1				
d1-01	42.400	20%	5	15 × 350	200	7.14	8
d1-02							
d1-03	41.650	20%	5	15 × 350	200	7.14	10
d1-04	41.900	20%	5	15 × 350	200	7.14	10
d1-05	42.150	20%	5	15 × 350	200	7.14	10
d1-06	42.400	20%	5	15 × 350	200	7.14	10
d1-07	42.650	20%	5	15 × 350	200	7.14	10
d1-08	42.900	20%	5	15 × 350	200	7.14	10
d1-09	42.650	20%	5	15 × 350	200	7.14	3
d1-10	43.150	20%	5	15 × 350	200	7.14	10
			Batch ♯2				
d2-01*							
d2-02	42.400	20%	6	15 × 350	200	8.57	24
d2-03	42.400	20%	6	15 × 350	200	8.57	17
d2-04	42.400	20%	6	15 × 350	200	8.57	25
d2-05*	42.400	20%	6	15 × 350	200	8.57	24
			Batch ♯3				
d3-01	42.400	20%	5	15 × 350	200	7.14	5
d3-02							
d3-03	42.400	20%	5	15 × 350	200	7.14	8
d3-04							
d3-05	42.400	20%	5	15 × 350	200	7.14	7.5
d3-06							
d3-07	42.400	20%	6	15 × 350	200	7.14	8
d3-08							
d3-09	42.400	20%	6	15 × 350	200	7.14	6
d3-10	42.400	20%	6	15 × 350	200	7.14	11.5
d3-11	42.400	20%	6	15 × 350	200	7.14	10
d3-12	42.400	20%	6	15 × 350	200	7.14	12
			Batch ♯4				
d4-01	42.150	20%	6	15 × 350	200	8.57	13
d4-02	42.150	20%	6	15 × 350	200	8.57	13

TABLE 8.2: $\chi^{(2)}$-grating periods and parameters used for periodic UV erasure. Handling resulted sometimes in breaking the PPSF. These fibres are marked with $*$.

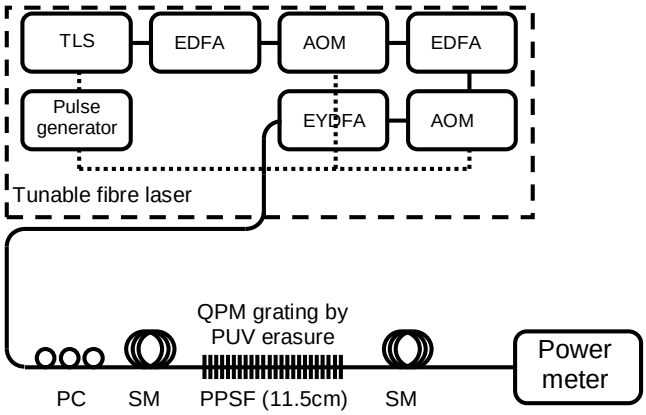

FIGURE 8.4: Schematic of the diode seeded tunable fibre laser and of the all-fibre frequency doubling system based on periodically poled silica fibre (PPSF): TLS-tunable laser seed, EDFA-Erbium doped fibre amplifier, AOM-acousto-optic modulator, EYDFA-Erbium Ytterbium doped fibre amplifier, PC-polarization controller, SM standard telecom single mode optical fibre. The grating for quasi phase matching (QPM) in the PPSF was 11.5 cm long and was fabricated by continuous writing periodic UV erasure (PUV).

8.3 Frequency Doubled Fibre Laser

A tunable (1535 nm-1562 nm), narrow linewidth (< 15 pm) single polarization fibre laser, with 10 ns pulses operating at 100 kHz (developed by C. Codemard from the High Power Fibre Laser group at ORC), was frequency doubled with a periodically poled device directly spliced to the output of the laser. The schematic of this all-fibre frequency doubling of a fibre laser is shown in the figure 8.4. A tunable continuous wave diode laser (TUNICS) was directly modulated through an external pulse generator to produce nanosecond pulses at the repetition rate of 100 kHz. The pulses were then seeded into a chain of erbium optical amplifiers (EDFA). The last stage was constituted by an erbium/ytterbium optical amplifier (EYDFA - GTWave amplifier-Southampton Photonics). An acousto-optic modulator before each of the last two amplifiers prevented amplification of the ASE (amplified stimulated emission) spectrum. The laser delivered a maximum peak power of ~ 200 W within the acceptance bandwidth ($\Delta\lambda_{\mathrm{FWHM}} \sim 1.5$ nm) of the periodically poled device. Further growth of the peak power is prevented by four-wave mixing in the last stage amplifier that spread the power to a broader range of wavelength outside the bandwidth of the poled devices.

8.4 Device Characterization

8.4.1 Uniformity

The devices are first characterized by examining the SH wavelength dependence. The set of graphs below refers to d1-06. Fig. 8.5(a) shows the wavelength tuning curve obtained for d1-06 as fabricated. The acceptance bandwidth, measured at FWHM, is 1.6 nm for a device length of 10.0 cm. The agreement with theoretical predictions (red curve) is remarkable and does show that the whole length of the device is used in the frequency conversion process. In order to highlight possible issues with uniformity during the process of writing the $\chi^{(2)}$-grating, the PPSF was cut-back to shorter lengths and the QPM curves measured for each piece. Figures 8.5(b)- (8.5(e) were obtained when the fibre was cut-back to length $L = 8$ cm, $L = 5$ cm,$L = 3$ cm and $L = 2$ cm, respectively. For each sample the bandwidth scales with its length according to predictions. This proves that the coherence between the SH wavelets and driving polarization is maintained along the length of the periodically poled fibres and ultimately confirms the good quality of the $\chi^{(2)}$-grating fabricated by our continuous writing method. The wavelength tuning curves for d1-01 and d3-10 are presented in the next section in Fig. 8.6 and Fig. 8.7, respectively. Note that for those devices an even better quality of the grating was achieved (See the side-lobes of the sinc^2 profile).

8.4.2 Efficiency

The frequency-doubler devices with the highest conversion efficiency are d1-01 and d3-10. In d3-10, 3.6 mW of red light in the fundamental mode was produced, by frequency doubling from 1554 nm to 777 nm. The maximum average pump power inside the PPSF was 148 mW corresponding to 108 W peak power. It follows that a maximum internal conversion efficiency of 2.4% was obtained. The quadratic dependence of the SH power against the pump power and the corresponding linear relationship between the conversion efficiency and the pump power, for d1-01 and d3-10, are shown in figure 8.6(left) and figure 8.7(left) respectively. The wavelength tuning curves are also presented.

Given the linear relationship holding between the pump peak power and conversion efficiency, we expect in d3-10 $\sim 50\%$ efficiency for frequency doubling of laser sources delivering 2 kW of peak power.

8.5 Open Issues

Periodically poled silica fibres d1-01 and d1-06, among the devices in batch ♯1, have shown a wavelength of operation within the tuneable range of the laser source. The

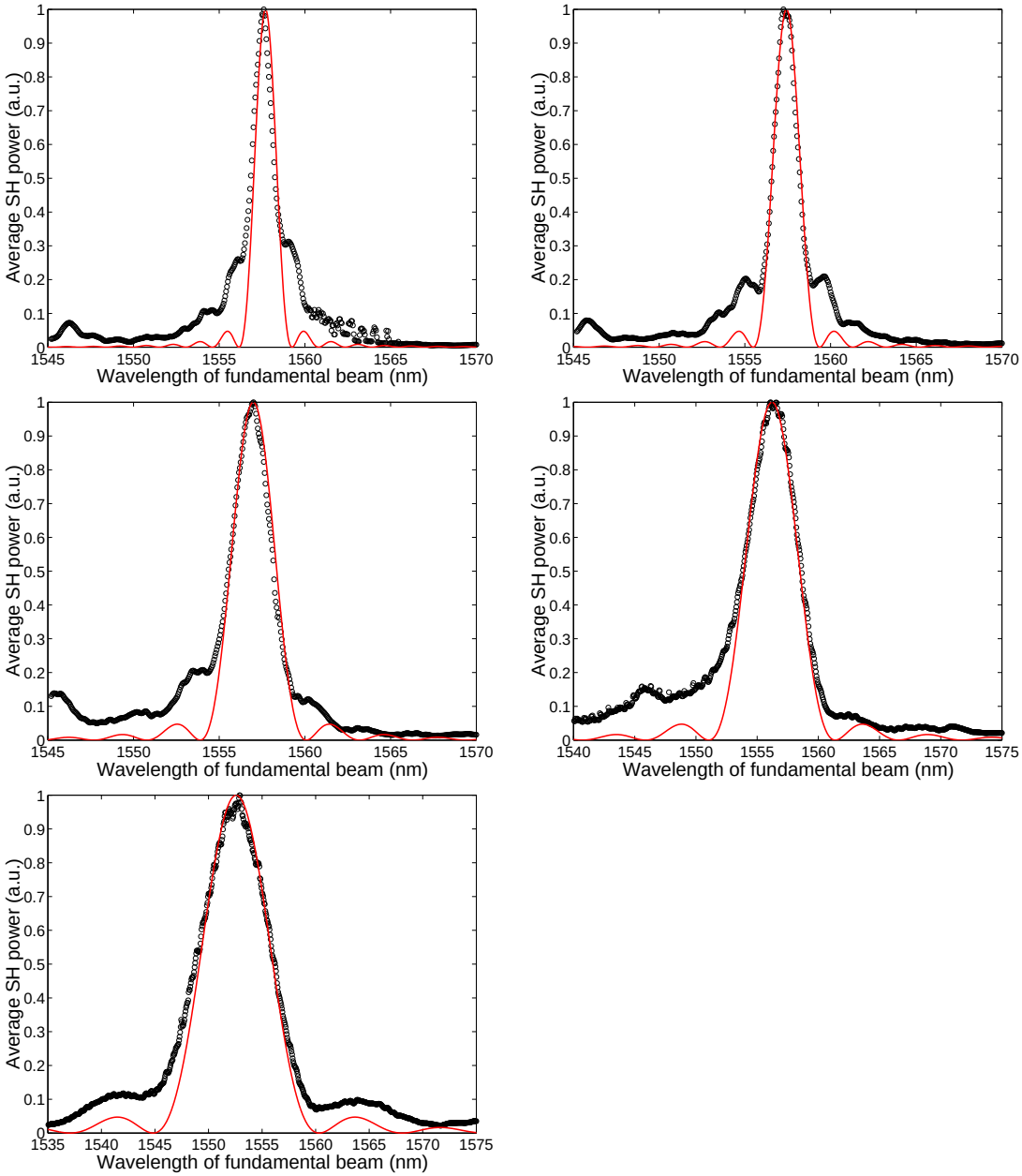

FIGURE 8.5: Cut-back measurements of the wavelength tuning profiles for d16 device. The red solid lines are the theoretical curves. No free parameter has been used to fit the experimental data. From left to right, top to bottom, $L = 10\,\text{cm}$, $L = 8\,\text{cm}$, $L = 5\,\text{cm}$, $L = 3\,\text{cm}$, $L = 2\,\text{cm}$.

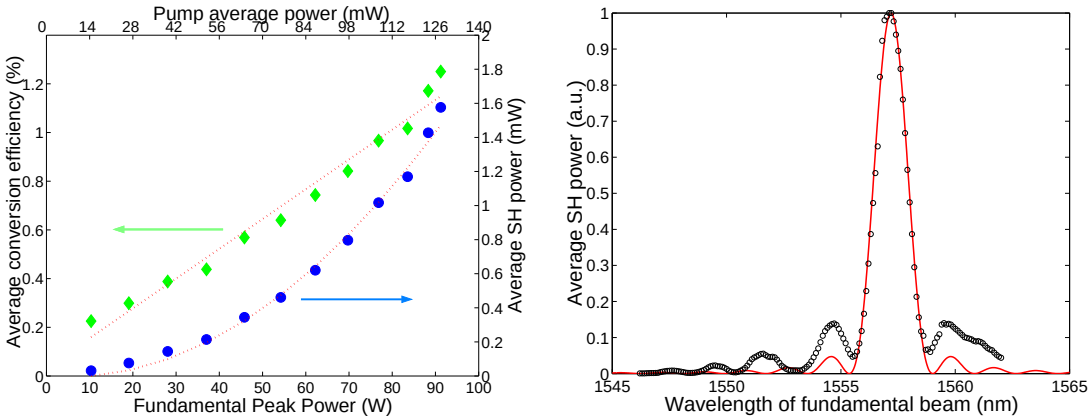

FIGURE 8.6: d1-01: Left. (blue circles) Quadratic dependence of the SH average power (right axis) versus the pump average power and (dotted line) fit to the experimental data. (green diamonds) correspondent average conversion efficiency (left axis) versus pump average power. (dotted line) linear fit to the experimental data. The wavelength of the fundamental is 1557 nm. Right: wavelength tuning profile of d1-01 ($L = 8$ cm) (circles) experimental data and (solid line) theoretical predictions. The acceptance bandwidth of the device is 2 nm at FWHM.

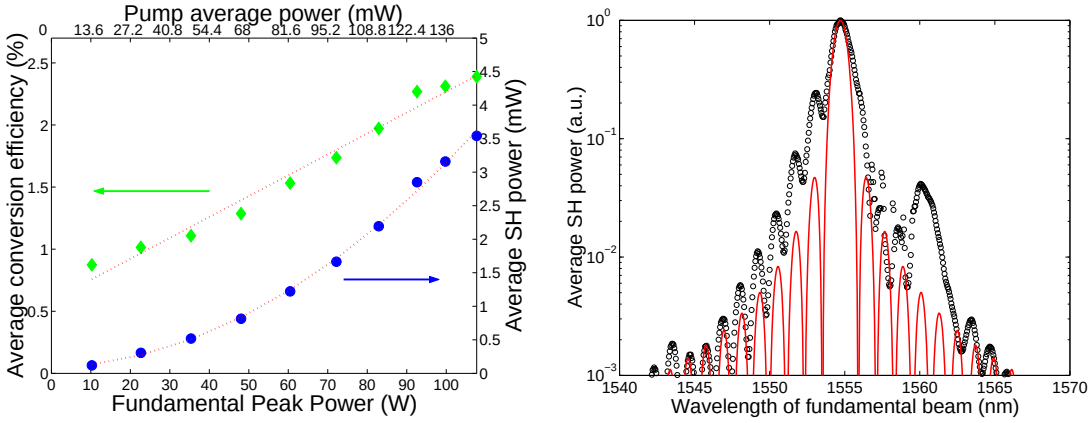

FIGURE 8.7: d3-10: Left. (blue circles) Quadratic dependence of the SH average power (right axis) versus the pump average power and (dotted line) fit to the experimental data. (green diamonds) correspondent average conversion efficiency (left axis) versus pump average power. (dotted line) linear fit to the experimental data. The wavelength of the fundamental is 1554 nm. Right: wavelength tuning profile of d3-10 ($L = 11.5$ cm) (circles) experimental data and (solid line) theoretical predictions. The acceptance bandwidth of the device is 1.4 nm at FWHM.

range of $\chi^{(2)}$-gratings periods for the devices in batch ♯1 was chosen in such a way that only one device would have been operating between 1535 nm and 1565 nm. The grating period of 42.400 nm was written in both d1-01 and d1-06 as it was the most likely to satisfy QPM in the tuning range of the laser according to simulations (Chapter 7). The experimental results were in good agreement with the simulations. The fact that both d1-01 and d1-06 exhibit a QPM wavelength centered at 1557 nm, and with similar conversion efficiency, highlights the quality and reproducibility of the continuous periodic UV erasure technology. Also the length of fibre used to fabricate devices in batch ♯1 is considerably uniform and consistent to enable comparison between two different devices.

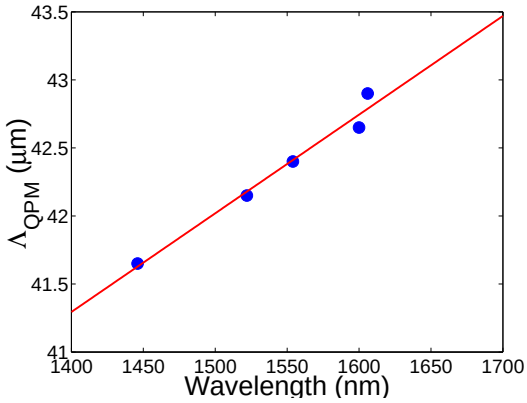

FIGURE 8.8: Period of the $\chi^{(2)}$-grating versus QPM for the devices in batch ♯1.

Although fabricated with the same period as d1-01 and d1-06, none of the long devices, made in batch ♯2, was working within the tuneable range of the laser source so that it was impossible to test their conversion efficiency. In batch ♯3, as it was discussed earlier, only devices from d3-09 to d3-12 have been poled in a reliable way. Device d3-10 is operating at 1554 nm, therefore not far from the devices previously fabricated in batch ♯1. On the other hand d3-09 exhibits phase matching at $\sim$ 1570 nm and the remaining devices do not show any QPM SHG at all in the tuning range of our laser source. Finally all the periodically poled fibres fabricated in batch ♯4 are not operating within the tunability range of the laser source. From the second batch, the device-to-device reproducibility has been a major issue which has prevented the final optimization of the fibre based frequency doubler. The fibre non-uniformities and consequently the determination of the QPM period to be used for the particular sample of fibre, among the various processes involved in the fabrication of the actual device, poling and periodic UV erasure, were identified as the critical steps. Very recently we introduced a new method for testing the devices which enabled us to come to this conclusion. By pumping the fibre laser source where the gain is higher and using low repetition rates (< 10 kHz), the spectrum of the laser pulse broadens widely due to non-linear effects induced by the high peak power. In such a broad spectrum a single wavelength will be phase-matched by the QPM grating in a periodically poled fibre. In these conditions a simple measurement of the spectrum at the output of a device would reveal the presence of the SH peak and the operation wavelength of the frequency doubler is twice the measured wavelength of the SH. Hence, it is possible to infer QPM even if the QPM condition occurs well outside the tunability range of the laser source. The devices in batch ♯1, being fabricated with different periods, are particularly suitable for the assessment of this method. The linear relationship holding between the QPM period and λ_{QPM} for device d1-01, d1-03, d1-05, d1-06, and d1-07 is outstanding, indicating the reliability of the continuous periodic UV erasure method (Fig. 8.8). On the other hand d1-08 is far from expected. We attribute this to the fact that we entered in a section of the fibre that was much less uniform than the beginning.

Chapter 9

Conclusions

Thermal poling is a reliable technique to induce a second-order nonlinearity in bulk glasses and optical fibres that can be exploited for frequency conversion [7]. Indeed, frequency doubling of lasers was demonstrated in the past and a maximum conversion efficiency of $5 \times 10^{-3}\%/\mathrm{W}$ in a 75 mm long periodically poled silica fibre, was obtained. This value is just about what is necessary for practical applications. The limitations are the relatively low value of the induced nonlinearity and the length of the poled fibre device which is limited by the photolithographic process to less than 10 cm.

The objective of this thesis was to increase the practicabilities of periodically poled fibres for wavelength conversion. In particular we have been targeting truly all-fibre frequency doubling of a fibre laser.

Two paths have been followed in order to meet the target: On one side fundamental research about poling techniques, glasses and characterization methods has been carried out in order to investigate possibilities for enhancing the second-order nonlinearity induced by poling. On the other side, we have been looking for an alternative technology for the fabrication of the $\chi^{(2)}$-gratings compatible with the fabrication of up to 1 m long devices. This led to the development of the continuous periodic UV erasure technique and to the demonstration of a truly all-fibre frequency doubling of a fibre laser.

9.1 Fundamental studies about poling

First demonstration of UV-fs poling technique

A new poling method has been discovered during this thesis work [28]: The UV-femtosecond poling, where two-photon absorption of femtosecond UV pulses in the presence of an applied electric field creates a permanent space-charge in silica glass. This work followed earlier works on UV-poling using ArF excimer laser [108] whereby the UV pulses were thought to break bonds in the germanosilcate matrix that could be

oriented by an applied electric field. Very high nonlinearity was reported, $\simeq 7\,\mathrm{pm/V}$, although independent groups have never succeeded in reproducing them.

In contrast to the traditional UV poling technique our method is not restricted to germano-silicate glasses, rather, it has been demonstrated in pure silica glass. The maximum value of the induced second-order nonlinearity was about $0.02\,\mathrm{pm/V}$ with the nonlinearity extending over the whole sample thickness. The value of the nonlinearity is in remarkable agreement with a rectification model [5, 7], $\chi^{(2)} = 3\chi^{(3)}E_{\mathrm{dc}}$ with E_{dc}, being the applied electric field, equal to $200\,\mathrm{kV/cm}$. The value of the induced nonlinearity was limited by the maximum field that could be applied before electrical breakdown in air took place. We therefore predict that a second-order nonlinearity exceeding $1\,\mathrm{pm/V}$ can be obtained if the experiment is performed in a twin-hole fibre, where the applied field can be much higher being only limited by the dielectric strength of silica at room temperature ($2 \times 10^9\,\mathrm{V/m}$ [30, 31]). This work has been carried out in collaboration with Prof. D. Nikogosyan from University College Cork and future works aiming at increasing the value of the induced $\chi^{(2)}$ in twin-hole fibres have already been scheduled.

Enhancement of $\chi^{(2)}$ in thermally poled silica by pre-exposing the glass to IR-fs irradiation

Exposure of synthetic silica to UV light pulses from a KrF excimer laser with subsequent creation of point defects, in particular non bridging oxygen hole centres (NBOHC), was known to induce, in a glass that could not otherwise be efficiently poled, second-order nonlinearities as high as $\simeq 1\,\mathrm{pm/V}$ [32]. Following the same concept we studied the effect of irradiation by a focused IR femtosecond laser on fused silica samples. It is known that femtosecond irradiation, by a multiphoton absorption process, breaks the Si-O covalent bonds. Defects, such as oxygen deficiency centers, E' centers and NBOHC, are created inside the silica matrix [33]. Silica pre-treatment by exposure to femtosecond pulses was proved in this thesis work to enhance the ability of the glass to freeze the electrostatic field induced by thermal poling, leading to higher nonlinearity [34]. This novel technique which makes it possible to achieve structural modification in the glass with micro-scale resolution may find applications for the fabrication of $\chi^{(2)}$-gratings. Though, a systematic study on the effect on the poling process due to different power levels of the femtosecond laser used for pre-treatment are necessary. There is likely to be a trade-off between damage caused by the high intensity irradiation, which are undesirable, and enhancement of the second-order nonlinearity.

Enhanced stability second-order nonlinearity in thermally poled glasses

Charge recombination within the bulk and near the surface is responsible for the decay of $\chi^{(2)}$ which is observed when the poled glass is heated above room temperature. Since charge recombination processes are dependent on the type of mobile ionic species and the glass matrix, the decay behaviour is expected to vary with glass composition. To which extent $\chi^{(2)}$ is stable in poled glass is not only a fundamental aspect of glass poling physics but it should be taken into account in the design of devices. In this thesis we re-

ported isothermal annealing measurements for the determination of the stability in poled glasses. Fused silica glass was found to be stable for over 30 years. A dramatic enhancement of the stability of $\chi^{(2)}$ was found in poled alkali free NA35 glass, a commercial glass produced by Nippon Sheet Glass [37]. These findings can be straightforwardly applied for enhancing the stability of periodically poled fibre devices. Although the stability of devices needs to be addressed independently it has been demonstrated by Xu et al. that a ring of boron surrounding the anode in a twin-hole fibre increases the stability of the nonlinearity [127]. Incidentally, boron is also one of the major components forming the NA35 glass, we have used.

Stack Maker's Fringe technique: a novel method for accurate determination of $\chi^{(2)}$ in poled glasses

In this thesis work a novel, all-optical, non destructive characterization technique which enables accurate determination of the $\chi^{(2)}$ in poled glasses was developed [38]. The technique is based on the interference between SH light beams which are generated by two identically poled glasses pressed together in a stack. Thicknesses, as small as $4\,\mu$m can be measured with a resolution better than $1\,\mu$m.

9.2 Long periodically poled silica fibre for all-fibre frequency doubling of fibre laser

Continuous Periodic UV erasure: A novel technology enabling fabrication of long ($> 10\,$cm) periodically poled silica fibres

The continuous periodic UV erasure is a major advance in the $\chi^{(2)}$-grating fabrication that has been demonstrated in this thesis for the first time. Previous technologies required the use of D-shape fibres so that on their flat surface, a periodic comb electrode could be patterned by photolithography [12]. The photolithographic process, though, limits the maximum length of the devices to about $10\,cm$. Periodic UV erasure, whereby exposure to UV light through an amplitude mask erases a uniform nonlinearity in the region under the open windows to create a $\chi^{(2)}$-grating for quasi-phase matching has also been demonstrated before [22]. In the continuous periodic UV erasure the QPM grating is created step by step by scanning a focused UV light beam along the core of the uniformly poled fibre on the regions that is necessary to erase. This technique not only is independent from any photolithographic process which prevented fabrication of long periodically poled fibres, but it also does not need amplitude masks which adds to the simplicity and flexibility of the method suggested by us. The continuous periodic UV erasure was used to demonstrate the fabrication of up to 25 cm long periodically poled fibres, limited only by the travel range of the translation stage. Efficient frequency conversion was demonstrated for a 11.5 cm long periodically poled fibre. In longer devices we were unable to meet the condition for quasi-pase matching. There were indications

of modifications of the core size along the length of the fibre. The step by step method for UV erasure could be associated in the near future with in-situ measurements of the conversion efficiency so that fibre non-uniformities might be compensated on-line by an appropriate variation of the grating period.

First demonstration of truly all-fibre frequency doubling of fibre laser
All-fibre frequency doubling of a fibre-laser has been demonstrated in this work for the first time. Milliwatts of red light in the fundamental mode were obtained by frequency doubling in quasi-phase matched periodically poled twin-hole silica fibre which was directly spliced to the fibre output of the pump laser. It is also the first demonstration of QPM in a twin-hole fibre, which was made possible by the use of an erasure technique for the $\chi^{(2)}$-grating fabrication. An average conversion efficiency of 2.4% was achieved in a 11.5 cm long device with pump peak power of only 108 W. The corresponding conversion efficiency, normalized for the pump power, is $\eta = 2.2 \times 10^{-2}$ %/W and is the highest ever reported for poled fibres.

9.3 Future work

Frequency doublers

One of the most concrete applications of a silica optical fibre that possesses second-order nonlinearities is frequency doubling of high power fibre laser sources. The laser market is pushing towards the development of sources that can offer, compactness, ruggedness, low maintenance, high wall-plug efficiency and low cost manufacture. Desirable options are also a good beam quality ($M^2 \simeq 1$) and the possibility of pulsed operation. The need for such a source has been emphasized, in recent years, by the rapid development of fibre lasers doped with rare-earths such as erbium, ytterbium or neodymium which can now be considered as a serious alternative to diode pumped solid state lasers (DPSSL) [17]. The impressive wall-plug efficiency (20%) allow them to be compact (approximately $20 \times 20 \times 10\,\mathrm{cm}^3$). Ruggedness and stability are ensured by the absence of bulk elements and cooling requirements are limited. Nd-doped fibre lasers are available today in the range of $890 - 940$ nm [187] whereas Yb-doped lasers cover the range of wavelength between $975 - 1150$ nm [188] and the window between $1525 - 1565$ nm is covered by Er-doped or Er/Yb-codoped fibre lasers [189]. Nowadays there is a growing interest in frequency doubling these sources to expand the range of available wavelengths into the visible [18]. The applications that would most benefit from it are e.g. in color display, life science, reprographic applications and optical data storage. The level of integrability that can be obtained through direct splicing with the fundamental source, makes periodically poled fibres ideal for frequency doubling of a fibre laser. It has been shown that the figure of merit for a frequency doubler based on periodically poled silica fibre is advantageous because of its low dispersion(large bandwidth for a given

interaction length), high optical damage threshold, not least because of the fact that the generated frequency doubled mode is a fundamental mode for the fibre i.e. with diffraction limited properties ($M^2 = 1$). Therefore, periodically poled fibres are expected to have an impact if used to frequency double high peak power, short pulsed, mode-locked, or Q-switched fibre lasers for applications requiring a high beam quality, in the green spectral range by doubling of Yb-doped fibre laser, or in the $700 - 800$ nm spectral range by doubling of tunable Er/Yb codoped fibre lasers or even at 488 nm, which is one of the emission lines of the Ar-ion laser, by frequency doubling of Nd-doped fibre lasers.

Tens of milliwatts average power are required to be competitive with already existing laser diode sources in the visible. Overall, diode lasers are not suitable for applications where medium powers, single mode and good beam quality are required simultaneously in particular in the green spectral region [17]. Furthermore, another limitation of pulsed diode lasers is their inability to operate with high peak powers ($> 20 - 40$ W). When this is necessary or whenever single mode operation, good beam quality and CW powers above tens of mW are required, frequency doubling of diode pumped solid state lasers in nonlinear crystals is typically chosen. For even higher power levels, hundreds of milliwatts up to some Watts, traditional cavities with intracavity frequency doubling crystals are utilized. These lasers are pumped by diode bars or flashlamps, they offer very good optical beam quality, but the cavity contains bulk elements and so ruggedness, compactness and long term stability are compromised.

An example of a practical application that could be achieved with the periodically poled fibre performances demonstrated in this thesis is for example the frequency doubling of the Fianium1060, a passively mode-locked Yb-doped fibre laser, operating at $\lambda = 1060$ nm produced by Fianium New Optics. According to the datasheet provided by the manufacturer the laser delivers up to 10 W and it can be operated in picosecond (6 ps) or femtosecond (> 200 fs) pulse regimes at a repetition rate of 100 MHz. The peak power is 16 kW for the picosecond regime and > 500 kW in the femtosecond one. The bandwidth is 12 nm for fs pulses and it is not specified for picosecond pulses. The expected performance of a frequency doubler based on a periodically poled silica fibre (PPSF) is shown in Fig. 9.1 where it is assumed that the pump laser is operating with 6 ps pulses, and a 11.5 cm long PPSF having nonlinear susceptibility $\chi^{(2)} = 0.06$ pm/V and overlapping area between the pump and SH modes of 17.45 μm^2. Although pump depletion is not considered, it is shown that average power levels at 520 nm exceeding hundreds of milliwatts should be easily achieved even in a relatively short periodically poled fibre (< 4 cm). This figure can be even further improved as there is room for at least a three fold improvement in the nonlinearity, meaning a 9 times increase in the conversion efficiency.

Other possible applications that can be envisaged are:

1. Single transversal mode seeding of optical amplifiers (e.g. chirped pulse amplifica-

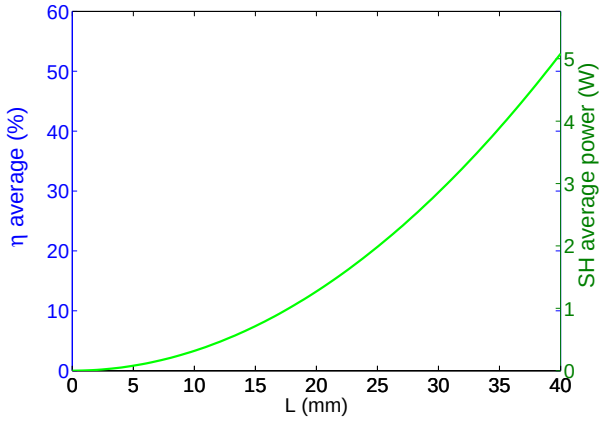

FIGURE 9.1: Estimates for the conversion efficiency against the length of the periodically poled fibre for frequency doubling of a passively mode-locked fibre laser produced by Fianium. According to the datasheet from the manufacturer, the Fianium1060 fibre laser operates at $\lambda = 1060\,\text{nm}$ and it delivers up to 10 W with 6 ps pulses at a repetition rate of 100 MHz. The peak power is 16 kW. The estimates have been carried out assuming the values of the nonlinear coefficient $d = 0.03\,\text{pm/V}$ and overlapping Area $A_{\text{OVL}} = 17.45\,\mu\text{m}^2$ obtained in the work presented in this thesis.

tion systems).

2. Single transversal mode pumping of Nd-doped fibre lasers.

3. Replacement of the Ti:sapphire laser by a system of smaller size, improved stability and lower cost, provided the frequency doubling source at 750 nm is also tuneable (e.g. by stretching/compressing the fibre). Indeed broadband tunability over 25 nm range of the periodically poled fibres has been demonstrated in our group. [144].

Quantum Cryptography The security of data and transactions relies upon encryption schemes which are not proven to be secure, but they are rather based on the assumption that the mathematical operations required to break the code are computationally highly inefficient. Therefore advances in mathematics, with the development of more efficient algorithms, would render these schemes insecure. Based on advances in the fundamentals of quantum mechanics, quantum cryptography (QC) has been introduced as a methodology for secure communication [190]. The field of QC is the one that would probably most benefit from the monolithic integration of a second-order nonlinear medium directly to the optical network without additional loss because amplifiers cannot be used. Up to date, practical implementation of QC relied on the preparation of pseudo-single photons state either by attenuation of standard semiconductor lasers or by producing photon-pairs by spontaneous parametric down-conversion in second-order nonlinear crystals. The latter implementation possesses some key advantages over the former, but the difficulty of always collecting both photons of a pair somewhat reduces this advantages. Production of photon-pairs in poled fibres has also been demonstrated. Optical quantum cryptography is based on the use of single photon states. Since quan-

tum mechanics tells us that it is impossible to read a quantum state without changing it and that is impossible to clone an unknown quantum state, the security of the communication is guaranteed. Attempts by an eavesdropper to read the quantum key, being distributed, affect the state of the photons in a readily detectable manner so that both the sender and the receiver are alerted. Unfortunately single-photon states are difficult to realize experimentally and practical implementations rely on highly attenuated laser pulses or entangled photon-pairs in which both the photons and the photon-pairs number distribution obey Poisson statistics. Hence, both suffer from a small possibility of generating more than one-photon or photon-pair at the same time and an eavesdropper can take advantage of these multiple photons pulses to extract information (so called beam-splitter attack). In practice, the probability that a non-empty pulse contains more than one photon can be made arbitrarily small by reducing the mean photon number μ. Ideally one would like really low photon numbers, $\mu < 0.01$, but the problem arises because of dark-pulses in the detector (i.e. a click without a photon arriving), which degrade the signal to noise ratio (detected photons over dark-counts ratio). The effect of dark-counts becomes more and more severe for extremely small mean photon-numbers, and consequently a high probability of an empty pulse and when QC is implemented at telecom wavelengths ($\lambda \simeq 1550\,\mathrm{nm}$) since photon detectors at these wavelengths, based on Indium Gallium Arsenide (InGaAs), are noisy and still at a development stage. Typical values used in experiments are $\mu = 0.1$ meaning that 5% of the non-empty pulses contain more than one photon and a typical figure is a bit-rate of $3\,\mathrm{Kb/s}$ over $10\,\mathrm{km}$. The problem of empty pulses and high dark-count probability can be circumvented by using photon-pairs as one photon of the pair can be used as a trigger to reveal the presence of the other. Because the second detector is open only when the first has received a photon, virtually it is $\mu = 1$. The difficulty of always collecting both photons of a pair greatly reduces this advantage. The photon-pairs are generated by spontaneous parametric down-conversion in a second-order nonlinear material such as typically LBO, having a wider bandwidth, or periodically poled lithium niobate. In this process one photon spontaneously splits into two daughter photons -traditionally called signal and idler- conserving total energy and momentum. Photon-pairs offer a further major advantage if they are not merely used as a pseudo-single-photon source, but if their entanglement is exploited. Entanglement leads to quantum correlation that can be used for key generation. In this case, if two photon-pairs are emitted within the same time window, but their measurement basis is chosen independently, they produce completely uncorrelated results. Hence, the eavesdropper cannot take advantage of such multi-photon pulses and the so called beam-splitter attack can be avoided. Highly attenuated lasers have been used in the vast majority of experiments because of their practicality but it is evident that an all-fibre source of entangled photons would be highly desirable. It is highlighted by the number of recent publications dealing with how to improve the coupling efficiency in parametric down conversion experiments in nonlinear crystals [191, 192, 193, 194].

List of Publications

Journal Papers

C. Corbari, P. G. Kazansky , S. A. Slattery, D. N. Nikogosyan
"Ultraviolet poling of pure fused silica by high-intensity femtosecond radiation",
Applied Physics Letters, Vol. 86, 071106, 2005

C. Corbari, P. G. Kazansky , S. A. Slattery, D. N. Nikogosyan
"Erratum: Ultraviolet poling of pure fused silica by high-intensity femtosecond radiation",
Applied Physics Letters, Vol. 86, 149902, 2005

Y. Menke a, M. Ferraris, C. Corbari, J. Fage-Pedersen
"New composite glass materials for non-linear optical applications",
Journal of non-Crystalline Solids, Vol. 345&346, pp. 366-371, 2004

O. Deparis, C. Corbari, P. G. Kazansky, K. Sakaguchi
Enhanced stability of the second-order optical nonlinearity in poled glasses,
Applied Physics Letters, Vol. 84, n. 24, pp.4857-4859, 2004

K. Tanaka, C. Corbari, P. G. Kazansky, J. Sasai, K. Hirao
"Second-harmonic generation in CuCl nano-crystal embedded short amorphous indium tin oxide thin film"
Japanese Journal of Applied Physics, Vol. 42, n. 11, pp. 6931-6932, 2003

C. Corbari, O. Deparis, B. G. Klappauf and P. G. Kazansky,
"Practical technique for measurement of second-order nonlinearity in poled glass",
Electronics Letters, Vol.39, n. 2, pp.197-8, 2003

C. Corbari, J.D. Mills, O. Deparis, B. G. Klappauf and P.G. Kazansky,
"Poling of glass modified by femtosecond irradiation",
Applied Physics Letters, Vol. 81 No. 9, pp.1585-1587, 2002

(This paper has been selected for the September 2002 issue of the
"Virtual Journal of Ultrafast Science".)

Conference Papers

S. A. Slattery, D. N. Nikogosyan, C. Corbari, P. G. Kazansky,
"UV poling of pure fused silica glass by high-intensity femtosecond radiation",
CLEO/Europe-EQUEC 2005 Munich 12-17 June 2005 (Postdeadline)

F. P. Mezzapesa, I. C. S. Carvalho, C. Corbari, P. G. Kazansky, J. S. Wilkinson, G. Chen,
"Voltage-assisted cooling: a new route to enhance $\chi^{(2)}$ during thermal poling",
CLEO/QUELS 2005 Baltimore 22-27 May 2005
C. Corbari, A. Canagasabey, M. Ibsen, F. Mezzapesa, C. Codemard, J. Nilsson, P. G. Kazansky
"All fibre frequency conversion in long periodically poled silica fibres",
OFC 2005 Anaheim 6-11 Mar 2005 OFB3

A. Canagasabey, C. Corbari, M. R. Mokhtar, P. G. Kazansky, M. Ibsen
"Tuneable second harmonic generation in long periodically poled optical fibres",
OFC 2005 Anaheim 6-11 Mar 2005 OThQ2

P. G. Kazansky, E. Bricchi, C. Corbari, B. G. Klappauf, O. Deparis, J. Qiu, Y. Shin, K. Hirao
"Femtosecond laser nano-structuring of transparent materials",
ILATA-III & LAM-X St. Petersburg 29 Jun - 3Jul 2003 (Invited)

O. Deparis, C. Corbari, F. Mezzapesa, P. G. Kazansky, K. Sakaguchi
"Second-order optical nonlinearity induced in high index bismuthate glass by thermal poling",
XX International Congress on Glass (ICG) 2004 Kyoto 26 Sep - 1 Oct 2004

F. P. Mezzapesa, C. Corbari, O. Deparis, P. G. Kazansky, J. S. Wilkinson
"Second-order nonlinearity profile in thermally poled twin-hole fibre",
CLEO/IQEC 2004 San Francisco 16-21 May 2004 CFI1

V. Pruneri, F. Lucchi, M. Belmonte, N. Myren, W. Margulis, C. Corbari, O. Deparis, P. G. Kazansky, J. Kristensen, M. Fage-Pederson, D. Ortega, B. Pastor, G. Capmany, Y. Quiquempois, A. Zeghlache, A. Kudlinsky, B. Poumellec, Q. Li, R. Blum, M. Ferraris

"The GLAMOROUS European Project (Glass-based modulators, routers and switches)",
BGPP 2003 Monterey 1-3 Sep 2003 (Invited)

O. Deparis, C. Corbari, P. G. Kazansky, K. Sakaguchi
"Stability of the second-order optical nonlinearity in poled glasses",
BGPP 2003 Monterey 1-3 Sep 2003

C. Corbari, O. Deparis, B. G. Klappauf and P. G. Kazansky,
"Practical technique for measurements of second-order nonlinearities in thermally poled glasses",
CLEO Europe/EQEC 2003 Munich 22-27 Jun 2003 CD2-2WED

O. Deparis, C. Corbari, P. G. Kazansky, B. Brichard, F. Berghmans, M. Decréton,
"Thermal poling of glass modified by gamma radiation",
Photonics Fab. Europe, Brugge 28 Oct.-1 Nov. 2002.

C. Corbari, G. Brambilla, N. Chiodini, A. Paleari, P. G. Kazansky, O. Deparis,
"Nonlinearity in poled Tin-doped samples fabricated by sol-gel technique",
SiO_2 and Advanced Dielectrics Trento 16-18 Sept. 2002"

J.D. Mills, C. Corbari, P.G. Kazansky, J.J. Baumberg,
"Femtosecond laser direct-writing and poling of embedded grating structures ",
paper QSuJ4, IQEC 2002 Moscow 22-28 Jun 2002.

C. Corbari, J.D. Mills, P.G. Kazansky, J.J. Baumberg,
"Poling of glass modified by femtosecond irradiation",
paper CTuN2, CLEO 2002 Long Beach 19-24 May 2002.

Bibliography

[1] R. J. Pressley, *Handbook of lasers with selected data on optical technology*, p. 246. CRC - Cleveland, Ohio, 1971.

[2] B. F. Levine, "A new contribution to the nonlinear optical susceptibility arising from unequal atomic radii," *Physical Review Letters*, vol. 25, no. 7, p. 440, 1970.

[3] W. Martienssen, G. Guelachvili, and K. Rao, *Landolt-Börnstein: Numerical data and functional relathionships in science and technology*, vol. 11, p. 671. Springer Verlag, New York, 1979.

[4] G. P. Agrawal, *Nonlinear Fiber Optics*. Optics and Photonics, Academic Press, 2nd ed., 1995.

[5] R. W. Boyd, *Nonlinear optics*. Academic Press, 1992.

[6] P. Butcher and D. Cotter, *The elements of nonlinear optics*. Cambridge University Press, 1990.

[7] R. A. Myers, N. Mukherjee, and S. R. J. Brueck, "Large second-order nonlinearity in poled fused silica," *Optics Letters*, vol. 16, no. 22, pp. 1732–1734, 1991.

[8] K. Tanaka, A. Narazaki, and K. Hirao, "Large optical second-order nonlinearity of poled WO_3-TeO_2 glass," *Optics Letters*, vol. 25, no. 4, pp. 251–253, 2000.

[9] A. Narazaki, K. Tanaka, K. Hirao, and N. Soga, "Effect of poling temperature on optical second-harmonic intensity of sodium zinc tellurite glass," *Journal of Applied Physics*, vol. 83, no. 8, pp. 3986–3990, 1998.

[10] F. C. Garcia, I. C. S. Carvalho, W. Margulis, and B. Lesche, "Inducing a large second-order optical nonlinearity in soft glasses by poling," *Applied Physics Letters*, vol. 72, no. 25, pp. 3252–3254, 1998.

[11] M. Guignard, V. Nazabal, J. Troles, F. Smektala, H. Zeghlache, Y. Quiquempois, A. Kudlinski, and G. Martinelli, "Second-harmonic generation of thermally poled chalcogenide glass," *Optics Express*, vol. 13, no. 3, p. 789, 2005.

[12] V. Pruneri, G. Bonfrate, P. G. Kazansky, D. J. Richardson, N. G. Broderick, J. P. deSandro, C. Sommineau, P. Vidakovic, and J. A. Levenson, "Greater than 20%

efficient frequency doubling of 1532 nm pulses in quasi-phase-matched germanosilicate fibres," *Optics Letters*, vol. 24, pp. 208–210, 1999.

[13] F. C. Garcia, L. Vogelaar, and R. Kashyap, "Poling of a channel waveguide," *Optics Express*, vol. 11, no. 23, pp. 3041–3047, 2003.

[14] N. Myren, H. Olsson, L. Norin, N. Sjodin, P. Helander, J. Svennebrink, and W. Margulis, "Wide wedge-shaped depletion region in thermally poled fiber with alloy electrodes," *Optics Express*, vol. 12, no. 25, pp. 6093–6099, 2004.

[15] X.-C. Long and S. R. J. Brueck, "Large-signal phase retardation with poled electroptic fiber," *IEEE Photonics Technology Letters*, vol. 9, no. 6, pp. 767–769, 1997.

[16] C. Corbari, A. Canagasabey, M. Ibsen, F. P. Mezzapesa, C. Codemard, J. Nilsson, and P. G. Kazansky, "All-fibre frequency conversion in long periodically poled silica fibres," in *OFC/NFOEC*, p. Paper OFB3, 2005.

[17] W. P. Risk, *Compact blue-green lasers*. Cambridge University Press, 2003.

[18] D. B. S. Soh, C. Codemard, S. Wang, J. Nilsson, J. K. Sahu, F. Laurell, V. Philippov, Y. Jeong, C. Alegria, and S. Baek, "A 980-nm Yb-doped fiber MOPA source and its frequency doubling," *IEEE Photonics Technology Letters*, vol. 16, no. 4, pp. 1032–1034, 2004.

[19] V. Pruneri and P. G. Kazansky, "Frequency doubling of picosecond pulses in periodically poled d-shape silica fibre," *Electronics Letters*, vol. 33, no. 4, pp. 318–319, 1997.

[20] V. Pruneri, G. Bonfrate, P. G. Kazansky, C. Simonneau, P. Vidakovic, and J. A. Levenson, "Efficient frequency doubling of 1.5 μm femtosecond laser pulses in quasi-phase-matched optical fibres ," *Applied Physics Letters*, vol. 72, no. 9, pp. 1007–1009, 1998.

[21] J. A. Armstrong, N. Bloembergen, J. Ducuing, and P. S. Pershan, "Interaction between light waves in a nonlinear dielectric," *Physical Review*, vol. 127, no. 6, pp. 1918–1939, 1962.

[22] G. Bonfrate, V. Pruneri, and P. G. Kazansky, "Periodic UV erasure of the nonlinearity for quasi-phase-matching in optical fibres." in CLEO 2000 paper CMO5, 2000.

[23] A. Okada, K. Ishii, K. Mito, and K. Sasaki, "Phase-matched second-harmonic generation in novel corona poled glass waveguides," *Applied Physics Letters*, vol. 60, no. 23, pp. 2853–2855, 1992.

[24] P. G. Kazansky, A. Kamal, and P. St. J. Russell, "High second-order nonlinearities induced in lead silicate glass by electron beam irradiation," *Optics Letters*, vol. 18, no. 9, pp. 693–695, 1993.

[25] P. Blazkiewicz, W. Xu, D. Wong, J. Canning, M. Asland, and G. Town, "Carbon dioxide laser-assisted poling of silicate-based optical fibers," *Optics Letters*, vol. 25, no. 4, pp. 200–202, 2000.

[26] T. Fujiwara, S. Matsumoto, M. Ohama, and A. J. Ikushima, "Origin and properties of second-order optical non-linearity in ultraviolet-poled GeO_2-SiO_2 glass," *Journal of Non-Crystalline Solids*, vol. 273, p. 203, 2000.

[27] J. Khaled, T. Fujiwara, and A. J. Ikushima, "Optimization of second-order nonlinearity in UV-poled silica glass," *Optical Materials*, vol. 17, pp. 275–278, 2001.

[28] C. Corbari, P. G. Kazansky, S. A. Slattery, and D. N. Nikogosyan, "Ultraviolet poling of pure fused silica by high-intensity femtosecond radiation," *Applied Physics Letters*, vol. 86, p. 071106, 2005.

[29] R. Adair, L. L. Chase, and S. A. Payne, "Nonlinear refractive index measurement of glasses using three-wave frequency mixing," *J. Opt. Soc. Am. B*, vol. 4, p. 875, 1987.

[30] T. G. Alley, S. R. J. Brueck, and R. A. Myers, "Space-charge dynamics in thermally poled fused silica," *Journal of Non-Crystalline Solids*, vol. 242, pp. 165–176, 1998.

[31] Y. Quiquempois, N. Godbout, and S. Lacroix, "Model of charge migration during thermal poling in silica glasses: Evidence of a voltage threshold for the onset of a second-order nonlinearity," *Physical Review A*, vol. 65, p. 043816, 2002.

[32] A. Kameyama, A. Yokotani, and K. Kurosawa, "Generation and erasure of second-order optical nonlinearities in thermally poled silica glasses by control of point defects," *Journal of the Optical Society of America B*, vol. 19, no. 10, pp. 2376–2382, 2002.

[33] H.-B. Sun, S. Juodkazis, M. Watanabe, S. Matsuo, H. Misawa, and J. Nishii, "Generation and recombination of defects in vitreous silica induced by irradiation with a near-infrared femtosecond laser," *J. Phys. Chem. B*, vol. 104, pp. 3450–3455, 2000.

[34] C. Corbari, J. D. Mills, O. Deparis, B. G. Klappauf, and P. G. Kazansky, "Thermal poling of glass modified by femtosecond irradiation," *Applied Physics Letters*, vol. 81, no. 9, pp. 1585–1587, 2002.

[35] Y. Menke, M. Ferraris, C. Corbari, and J.Fage-Pedersen, "New composite glass materials for non-linear optical applications," *Journal of non-Crystalline Solids*, vol. 345-346, pp. 366–371, 2004.

[36] J. Arentoft, M. Kristensen, K. Pedersen, S. Bozhevolnyi, and P. Shi, "Poling of silica with silver-containing electrodes," *Electronics Letters*, vol. 36, no. 19, pp. 1635–1636, 2000.

[37] O. Deparis, C. Corbari, P. G. kazansky, and K. Sakaguchi, "Enhanced stability of the second-order optical nonlinearity in poled glasses," *Applied Physics Letters*, vol. 84, no. 24, pp. 4857–4859, 2004.

[38] C. Corbari, O. Deparis, B. G. Klappauf, and P. G. Kazansky, "Practical technique for measurement of second-order nonlinearity in poled glass," *Electronics Letters*, vol. 39, p. 197, 2003.

[39] B. Lesche, F. C. Garcia, E. N. Hering, W. Margulis, I. C. S. Carvalho, and F. Laurell, "Etching of silica glass under electric fields," *Physical Review Letters*, vol. 78, no. 11, pp. 2172–2175, 1997.

[40] A. Ozcan, M. J. F. Digonnet, and G. S. Kino, "Erratum: Inverse Fourier transform technique to determine second-order optical nonlinearity spatial profiles (vol 82, pg 1362, 2003)," *Applied Physics Letters*, vol. 83, no. 8, p. 1679, 2003.

[41] V. Treanton, N. Godbout, and S. Lacroix, "Nondestructive interferometric determination of $\chi^{(2)}(z)$ spatial distribution induced in thermally poled silica glasses," *Journal of the Optical Society of America B*, vol. 21, no. 12, pp. 2213–220, 2004.

[42] A. L. C. Triques, I. C. S. Carvalho, M. F. Moreira, H. R. Carvalho, R. Fisher, B. Leshe, and W. Margulis, "Time evolution of depletion region in poled silica," *Applied Physics Letters*, vol. 82, no. 18, pp. 2948–2950, 2003.

[43] A. Kudlinski, Y. Quiquempois, M. Lelek, H. Zeghlache, and G. Martinelli, "Complete characterization of the nonlinear spatial distribution induced in poled silica glass with a submicron resolution," *Applied Physics Letters*, vol. 83, no. 17, pp. 3623–3625, 2003.

[44] A. Ozcan, M. Digonnet, G. S. Kino, F. Ay, and A. Aydinly, "Characterization of thermally poled germanosilicate thin-films," *Optics Express*, vol. 12, no. 20, pp. 4698–4708, 2004.

[45] M. Houe' and P. D. Townsend, "An introduction to methods of periodic poling for second-harmonic generation," *Journal of Physics D*, vol. 28, pp. 1747–1763, 1995.

[46] D. Gloge, "Weakly guiding fibers," *Applied Optics*, vol. 10, no. 10, pp. 2252–2258, 1971.

[47] A. Yariv, *Optical Electronics*. CBS college publishing, 3rd edition ed., 1985.

[48] M. M. Fejer, G. A. Magel, D. H. Jundt, and R. L. Byer, "Quasi-phase matched second-harmonic generation: tuning and tolerances," *IEEE Journal of Quantum Electronics*, vol. 28, no. 11, pp. 2631–2653, 1992.

[49] Y. Fujii, B. Kawasaky, K. O. Hill, and D. C. Johnson, "Sum frequency light generation in optical fibres," *Optics Letters*, vol. 5, p. 48, 1980.

[50] Y. Sasaki and Y. Ohmori, "Phase matched sum-frequency light in optical fibres," *Applied Physics Letters*, vol. 39, p. 466, 1982.

[51] U. Österberg and W. Margulis, "Dye laser pumped by Nd:YAG laser pulses frequency doubled in glass optical fibre," *Optics Letters*, vol. 11, p. 517, 1986.

[52] R. H. Stolen and H. W. K. Tom, "Self-organized generation in optical fibres," *Optics Letters*, vol. 13, p. 585, 1986.

[53] M. C. Farries, P. St. J. Russell, M. E. Fermann, and D. N. Payne, "Second-harmonic generation in an optical fibre by self-written $\chi^{(2)}$ grating," *Electronics Letters*, vol. 23, p. 322, 1987.

[54] E. M. Dianov, P. G. Kazansky, and D. Y. Stepanov, "Problem of the photoinduced second-harmonic generation," *Soviet Journal of Quantum Electronics*, vol. 19, p. 575, 1989.

[55] E. M. Dianov, P. G. Kazansky, and D. Y. Stepanov, "Photovoltaic model of photoinduced second-harmonic generation in optical fibres," *Soviet Lightwave Communications*, vol. 1, p. 247, 1991.

[56] E. M. Dianov, P. G. Kazansky, D. S. Starodubov, and D. Y. Stepanov, "Observation of phase mismatching during preparation of second-order susceptibility gratings in glass optical fibres," *Soviet Lightwave Communications*, vol. 2, p. 385, 1992.

[57] E. M. Dianov, P. G. Kazansky, and D. Y. Stepanov, "Photoinduced second-harmonic generation: observation of charge separation due to the photovoltaic effect," *Soviet Lightwave Communications*, vol. 3, p. 83, 1992.

[58] V. Dominic and J. Feinberg, "Light induced 2nd-harmonic generation in glass via multiphoton ionization," *Physical Review Letters*, vol. 73, p. 3446, 1993.

[59] R. W. Terhune and D. A. Weinberger, "Second-harmonic generation in fibres," *J. Opt. Soc. Am. B*, vol. 4, p. 661, 1987.

[60] V. Mizrahi and U. ´Osterberg and C. Krautchik and G. E. Stegeman and J. E. Sipe and T. P. Morse, "Direct test of a model of efficient second-harmonic generation in optical fibres," *Applied Physics Letters*, vol. 53, p. 557, 1988.

[61] M. V. Bergot, M. C. Farries, M. E. Fermann, L. Li, L. J. Poyntz-Wright, P. St. J. Russell, and A. Smithson, "Generation of permanent optically induced 2nd order nonlinearities in optical fibres by poling," *Optics Letters*, vol. 13, p. 592, 1988.

[62] V. Mizrahi, Y. HIbino, and G. Stegeman, "Polarization study of photoinduced second-harmonic generation in optical fibres," *Optics Communication*, vol. 78, p. 283, 1990.

[63] A. Kamal, D. A. Weinberger, and W. H. Weber, "Spatially resolved Raman study of self-organized $\chi^{(2)}$ gratings in optical fibres," *Optics Letters*, vol. 15, p. 613, 1990.

[64] D. Anderson, V. Mizrahi, and J. E. Sipe, "Model for second-harmonic generation in glass optical fibres based from asymmetric photoelectron emission from defect sites," *Optics Letters*, vol. 16, p. 796, 1991.

[65] D. M. Krol, D. J. DiGiovanni, W. Pleibel, and R. H. Stolen, "Observation of resonant enhancement of photoinduced second-harmonic generation in Tm-doped aluminosilicate glass fibres," *Optics Letters*, vol. 18, p. 1220, 1993.

[66] K. Hagimoto and A. Mito, "Determination of the second-order susceptibility of ammonium dihydrogen phosphate and α-quartz at 633 and 1064 nm," *Applied Optics*, vol. 34, no. 36, pp. 8276–8282, 1995.

[67] K. D. Singer, J. E. Sohn, and S. J. Lalama *Applied Physics Letters*, vol. 49, p. 248, 1986.

[68] J. Zyss, ed., *Molecular Nonlinear Optics. Material Physics and Devices*. Quantum Electronics - Principles and Applications, Academic Press Inc., 1994.

[69] D. E. Carlson, "Ion depletion of glass at a blocking anode: I, theory and experimental results for alkali silicate glasses," *Journal of the American Ceramic Society*, vol. 57, no. 7, p. 291, 1974.

[70] N. Mukherjee, R. A. Myers, and S. R. J. Brueck, "Dynamics of second-harmonic generation in fused silica," *J. Opt. Soc. Am. B*, vol. 11, no. 4, pp. 665–669, 1994.

[71] P. G. Kazansky and P. St. J. Russell, "Thermally poled glass: frozen-in electric field or oriented dipoles?," *Optics Communication*, vol. 110, pp. 611–614, 1994.

[72] R. Kashyap, G. J. Veldhuis, D. C. Rogers, and P. F. Mckee, "Phase-matched second-harmonic generation by periodic poling of fused silica," *Applied Physics Letters*, vol. 64, no. 11, pp. 1332–1334, 1994.

[73] T. G. Alley, S. R. J. Brueck, and M. Wiedenbeck, "Secondary ion mass spectrometry study of space charge formation in thermally poled fused silica," *Journal of Applied Physics*, vol. 86, no. 12, pp. 6634–6640, 1999.

[74] P. G. Kazansky, A. R. Smith, and P. St. J. Russell, "Thermally poled silica glass: Laser induced pressure pulse probe of charge distribution," *Applied Physics Letters*, vol. 68, no. 2, pp. 269–271, 1996.

[75] T. G. Alley and S. R. J. Brueck, "Visualization of the nonlinear optical space-charge region of bulk thermally poled fused-silica glass," *Optics Letters*, vol. 23, no. 15, pp. 1170–1172, 1998.

[76] A. L. C. Triques, C. M. B. Cordeiro, V. Balestrieri, B. Lesche, W. Margulis, and I. C. S. Carvalho, "Depletion region in thermally poled fused silica," *Applied Physics Letters*, vol. 76, no. 18, pp. 2496–2498, 2000.

[77] A. Le Calvez, E. Freysz, and A. Ducasse, "Experimental study of the origin of the second-order nonlinearities induced in thermally poled fused silica," *Optics Letters*, vol. 22, no. 20, pp. 1547–1549, 1997.

[78] A. Von Hippel, E. P. Gross, J. G. Jelatis, and M. Geller, "Photocurrent, space-charge buildup, and field emission in alkali halide crystals," *Physical Review*, vol. 91, no. 3, pp. 568–579, 1953.

[79] Y. Quiquempois, G. Martinelli, P. Duthérage, P. Bernage, P. Niay, and M. Douay, "Localisation of the induced second-order non-linearity within Infrasil and Suprasil thermally poled glasses," *Optics Communications*, vol. 176, pp. 479–487, 2000.

[80] A. Kameyama, A. Yokotani, and K. Kurosawa, "Identification of defects associated with second-order optical nonlinearity in thermally poled high-purity silica glasses," *Journal of Applied Physics*, vol. 89, no. 9, pp. 4707–4713, 2001.

[81] T. M. Proctor and P. M. Sutton, "Static space-charge distribution with a single mobile charge carrier," *Journal of Chemical Physics*, vol. 30, no. 1, pp. 212–220, 1959.

[82] V. Pruneri, F. Samoggia, G. Bonfrate, P. G. Kazansky, and G. M. Yang, "Thermal poling of silica in air and under vacuum: the influence of charge transport on second harmonic generation," *Applied Physics Letters*, vol. 74, no. 17, pp. 2423–2425, 1999.

[83] D. Faccio, V. Pruneri, and P. G. Kazansky, "Dynamics of the second-order nonlinearity in thermally poled silica glass," *Applied Physics Letters*, vol. 79, no. 17, pp. 2687–2689, 2001.

[84] N. Godbout and S. Lacroix, "Characterization of thermal poling in silica glassses by current measurements," *Journal of Non-Crystalline Solids*, vol. 316, pp. 338–348, 2003.

[85] X.-M. Liu, H.-Y. Zhang, Y.-L. Guo, X.-P. Zheng, and Y. Li, "Modeling of thermal/electric-field poling," *Japanese Journal of Applied Physics*, vol. 40, pp. L807–L809, 2001.

[86] X.-M. Liu and M.-D. Zhang, "Theoretical study for thermal/electric field poling of fused silica," *Japanese Journal of Applied Physics*, vol. 40, pp. 4069–4076, 2001.

[87] A. Kudlinski, Y. Quiquempois, H. Zeghlache, and G. Martinelli, "Evidence of second-order nonlinear susceptibility sign reversal in thermally poled samples," *Applied Physics Letters*, vol. 83, no. 16, pp. 3242–3244, 2003.

[88] D. Pureur, A. C. Liu, M. J. F. Digonnet, and G. S. Kino, "Absolute measurement of the second-order nonlinearity profile in poled silica," *Optics Letters*, vol. 23, no. 8, pp. 588–590, 1998.

[89] Y. Quiquempois, G. Martinelli, F. Valentin, P. Bernage, P. Niay, and M. Douay, "Improved method for measuring second-order non-linearity profile in poled silica," in *TOPS-Bragg Gratings, Photosensitivity and Poling in Glass Waveguides* (OSA, ed.), vol. 33, p. 404, 2000.

[90] A. Ozcan, M. J. F. Digonnet, and G. S. Kino, "Cylinder-assisted Maker-fringe technique," *Electronics Letters*, vol. 39, no. 25, 2003.

[91] D. Faccio, V. Pruneri, and P. G. Kazansky, "Noncollinear Makers fringe measurements of second-order of nonlinear optical layers," *Optics Letters*, vol. 25, no. 18, pp. 1376–1378, 2000.

[92] H. Guillet de Chatellus, S. Montant, and E. Freysz, "Nondestructive method for characterization of the second-order nonlinear profile and charge distribution in thermally poled fused silica," *Optics Letters*, vol. 25, no. 23, pp. 1723–1725, 2000.

[93] A. Ozcan, M. J. F. Digonnet, and G. S. Kino, "Inverse Fourier transform technique to determine second-order optical nonlinearity spatial profiles," *Applied Physics Letters*, vol. 82, no. 9, pp. 1362–1364, 2003.

[94] A. Ozcan, M. J. F. Digonnet, and G. S. Kino, "Improved technique to determine second-order optical nonlinearity profiles using two different samples," *Applied Physics Letters*, vol. 84, no. 5, pp. 681–683, 2004.

[95] A. Ozcan, M. J. F. Digonnet, and G. S. Kino, "Simplified inverse Fourier transform technique to measure optical nonlinearity profiles using reference sample," *Electronics Letters*, vol. 40, no. 9, pp. 551–552, 2004.

[96] A. Ozcan, M. J. F. Digonnet, and G. S. Kino, "Iterative processing of second-order optical nonlinearity depth profiles," *Optics Express*, vol. 12, no. 15, pp. 3367–3376, 2004.

[97] H. Nasu, T. Ito, H. Hase, J. Matsuoka, and K. Kamiya, "Third-order optical non-linearity of Bi_2O_3-based glasses," *Journal of Non-Crystalline Solids*, vol. 204, pp. 78–82, 1996.

[98] K. Tanaka, A. Narazaki, H. Hirao, and N. Soga, "Poling temperature dependence of optical second-harmonic intensity of MgO-ZnO-TeO_2 glasses," *Journal of Applied Physics*, vol. 79, no. 7, pp. 3798–3800, 1996.

[99] K. Tanaka, K. Kashima, K. Kajihara, K. Hirao, N. Soga, A. Mito, and H. Nasu, "Second-harmonic generation in electrically poled TeO_2-based glasses," *Proc. of SPIE*, vol. 2289, pp. 167–175, 1994.

[100] K. Tanaka, A. Narazaki, K. Hirao, and N. Soga, "Optical second harmonic generation in poled MgO-ZnO-TeO_2 and B_2O_3-TeO_2 glasses," *Journal of Non-Crystalline Solids*, vol. 203, pp. 49–54, 1996.

[101] H. G. Kim, T. Komatsu, K. Shioya, K. Matusita, K. Tanaka, and K. Hirao, "Transparent tellurite-based glass-ceramics with second harmonic generation," *Journal of non-Crystalline Solids*, vol. 208, pp. 303–307, 1996.

[102] A. Narazaki, K. Tanaka, and K. Hirao, "Poling-induced crystallization of tetragonal $BaTiO_3$ and enhancement of optical second-harmonic intensity in Ba-TiO_2-TeO_2 glass system," *Applied Physics Letters*, vol. 75, no. 21, pp. 3399–3401, 1999.

[103] H. Nasu, K. Kurachi, A. Mito, H. Okamoto, J. Matsuoka, and K. Kamiya, "Second harmonic generation from an electrically polarized TiO_2-containing silicate glass," *Journal of Non-Crystalline Solids*, vol. 181, pp. 83–86, 1995.

[104] T. Cardinal, E. Fargin, V. Nazabal, G. L. Flem, S. L. Boiteux, and L. Ducasse, "Glass local structure and optical nonlinearities of oxide glasses," *Journal of non-Crystalline Solids*, vol. 239, pp. 131–138, 1998.

[105] X.-C. Long and S. R. J. Brueck, "Large photosensitivity in lead-silicate glasses," *Applied Physics Letters*, vol. 74, no. 15, pp. 2110–2112, 1999.

[106] M. Qiu, F. Pi, and G. Orriols, "The role of lead component in second-harmonic generation in lead silica by electron-beam irradiation," *Applied Physics Letters*, vol. 73, no. 21, pp. 3040–3042, 1998.

[107] M. Qiu, T. Mizunami, Y. Takagaki, R. Vilaseca, and J. Martorell, "Study of the second-order susceptibility from the cathode-side face of poled glasses," *Journal of Non-Crystalline Solids*, vol. 255, pp. 250–253, 1999.

[108] T. Fujiwara, M. Takahashi, and A. J. Ikusuma, "Second-harmonic generation in germanosilicate glass poled with ArF laser irradiation," *Journal of Applied Physics*, vol. 71, no. 8, pp. 1032–1034, 1997.

[109] T. Fujiwara, M. Takahashi, and A. J. Ikusuma, "Decay behaviour of second-order nonlinearity in GeO_2-SiO_2 glass poled with UV-irradiation," *Electronics Letters*, vol. 33, p. 980, 1997.

[110] M. Ohama, T. Fujwara, and A. J. Ikushima, "Induced defects and increase of second-order nonlinearities in ultraviolet poled GeO_2-SiO_2 glass," *Japanese Journal of Applied Physics*, vol. 38, no. 11, pp. 6359–6361, 1999.

[111] W. Margulis, F. Garcia, E. Hering, L. G. Valente, B. Lesche, F. Laurell, and I. Carvalho, "Poled glasses," *MRS Bulletin*, vol. 23, p. 31, 1998.

[112] W. Xu, P. Blazkiewicz, and S. Fleming, "Silica fiber poling technology," *Advanced Materials*, vol. 13, p. 1014, 2001.

[113] Y. Quiquempois, G. Martinelli, P. Bernage, M. Douay, P. Niay, E. Delevaque, H. Poignant, B. Loisel, and J. F. Bayon, "Study of organised $\chi^{(2)}$ susceptibility in germanosilicate optical fibers," *Optical Materials*, vol. 9, p. 361, 1998.

[114] P. Blazkiewicz, W. Xu, and S. Fleming, "Optimum parameters for CO_2 laser-assisted poling of optical fibers," *Journal of Lightwave Technology*, vol. 20, p. 965, 2002.

[115] P. G. Kazansky, A. Kamal, and P. St. J. Russell, "Erasure of thermally poled second-order nonlinearity in fused silica by electron implantation," *Optics Letters*, vol. 18, p. 1141, 1993.

[116] L. Li and D. N. Payne, "Permantly induced linear electro-optic effect in silica optical fibre," in *IGWO*, 1989.

[117] P. G. Kazansky, L. Dong, and P. St. J. Russell, "High second-order nonlinearity in poled silicate fibres," *Optics Letters*, vol. 19, no. 10, pp. 701–703, 1994.

[118] P. G. Kazansky, L. Dong, and P. St. J. Russell, "Vacuum poling: an improved technique for effective thermal poling of silica glass and germanosilicate optical fibres," *Electronics Letters*, vol. 30, no. 16, pp. 1345–1346, 1994.

[119] X.-C. Long, R. A. Myers, and S. R. J. Brueck, "Mesurement of linear electro-optic effect in temperature/electric-field poled optical fibres," *Electronics Letters*, vol. 30, no. 25, pp. 2162–2163, 1994.

[120] M. Abe, T. Kitagawa, K. Hattori, A. Himeno, and Y. Ohmori, "Electro-optic switch constructed with a poled silica-based waveguide on a Si substrate," *Electronics Letters*, vol. 32, p. 893, 1996.

[121] D. Faccio, A. Busacca, V. Pruneri, P. G. Kazansky, T. M. Monro, W. Belardi, D. J. Richardson, B. Grappe, M. Cooper, and C. N. Pannell, "Experimental study of thermal poling in holey fibres," 2000.

[122] T. M. Monro, V. Pruneri, N. G. R. Broderick, D. Faccio, P. G. Kazansky, and D. J. Richardson, "Broad-band second-harmonic generation in holey optical fibers," *IEEE Photonics Technology Letters*, vol. 13, no. 9, 2001.

[123] D. Wong, W. Xu, M. Janos, J. Chow, R. Hall, and S. Fleming, "Time evolution of electro-optic effect in fibre during thermal poling," *Japanese Journal of Applied Physics, Part I*, vol. 37, pp. 68–70, 1998.

[124] W. Xu, D. Wong, and S. Fleming, "Evolution of linear electro-optic coefficients and third-order nonlinearity during prolonged negative thermal poling of silica fibre," *Electronics Letters*, vol. 35, no. 11, pp. 922–923, 1999.

[125] W. Xu, J. Arentoft, D. Wong, and S. Fleming, "Evidence of space-charge effects in thermal poling," *IEEE Photonics Technology Letters*, vol. 11, no. 10, pp. 1265–1267, 1999.

[126] A. De Francesco and G. E.Town, "Modeling the electrooptic evolution in thermally poled germanosilicate fibers," *IEEE Journal of Quantum Electronics*, vol. 37, no. 10, pp. 1312–1320, 2001.

[127] W. Xu, P. Blazkiewicz, D. Wong, S. Fleming, and T.Ryan, "Specialty optical fibre for stabilising and enhancing electro-optic effect induced by poling," *Electronics Letters*, vol. 36, no. 15, pp. 1265–1266, 2000.

[128] M. Janos, W. Xu, D. Wong, H. Inglis, and S. Fleming, "Growth and decay of the electroptic effect in thermally poled B/Ge codoped fiber," *Journal of Lightwave Technology*, vol. 17, no. 6, pp. 1037–1041, 1999.

[129] R. Kashyap, "-," in *Bragg Gratings Poling and Photosensitivity in Glass Waveguides*, OSA topical meeting, 2003.

[130] M. Fokine and L. E. Nilsson and Å. Claesson and D. Berlemont and L. Kjellberg and L. Krummenacher and W. Margulis, "Integrated fiber mach-zehnder interferometer for electro-optic switching," *Optics Letters*, vol. 27, pp. 1643–1645, 2002.

[131] R. Kashyap, "Phase-matched periodic electric-field-induced second harmonic generation in optical fibers," *J. Opt. Soc. Am. B*, vol. 6, no. 3, pp. 313–328, 1989.

[132] P. G. Kazansky, V. Pruneri, and P. St. J. Russell, "Blue light generation by quasi phase mached frequency doubling in thermally poled optical fibre," *Optics Letters*, vol. 20, no. 8, pp. 843–845, 1994.

[133] C. Simmoneau, J. A. Levenson, P. Vidakovic, G. Bonfrate, V. Pruneri, and P. G. Kazansky, "Influence of $\chi^{(2)}$ effects on second-harmonic generation of ultrashort pulses in quasi-phase matched silica fibres," in *Digest of Conference on Lasers and Electro Optics*, p. paper CTuD2, 1998.

[134] G. Bonfrate, V. Pruneri, P. G. Kazansky, P. Tapster, and J. G. Rarity, "Parametric fluorescence in periodically poled silica fibres," *Applied Physics Letters*, vol. 75, no. 16, pp. 2356–2358, 1999.

[135] F. Ouellette, K. O. Hill, and D. C. Johnson, "Light induced erasure of self-organized $\chi^{(2)}$ gratings in optical fibers," *Optics Letters*, vol. 13, no. 6, pp. 515–517, 1988.

[136] I. C. S. Carvalho, W. Margulis, and B. Leshe, "Erasure of frequency doubling gratings in optical fibres by ultraviolet light excitation," *Electronics Letters*, vol. 27, no. 17, pp. 1497–1498, 1991.

[137] H.-Y. Chen, J.-S. Sue, Y.-H. Lin, and S. Chao, "Quasi-phase-matched second-harmonic generation in ultraviolet-assisted periodically poled planar fused silica," *Optics Letters*, vol. 28, no. 11, pp. 917–919, 2003.

[138] H.-Y. Chen, J.-S. Sue, Y.-H. Lin, C.-S. Tsai, P.-T. Wu, and S. Chao, "Thermal poling and ultraviolet erasure characteristics of type-III ultraviolet grade fused silica and application to periodic poling on planar substrates," *Journal of Applied Physics*, vol. 94, no. 3, pp. 1531–1537, 2003.

[139] S. Montant, A. Le Calvez, E. Freysz, A. Ducasse, V. Nazabal, E. Fargin, and G. Le Flem, "Light-controlled erasure of induced χ^2 in thermally poled glasses," *Applied Physics Letters*, vol. 74, no. 18, pp. 2623–2625, 1999.

[140] S. Montant, H. Guillet de Chatellus, and E. Freysz, "Laser-induced quasi-phase matching in thermally poled glasses," *Optics Letters*, vol. 26, no. 11, pp. 837–839, 2001.

[141] H. Guillet de Chatellus, S. Montant, and E. Freysz, "Spatial control of second-order optical susceptibility induced in thermally poled glasses," *Applied Physics Letters*, vol. 78, no. 20, pp. 3018–3020, 2001.

[142] M. Ibsen and R. I. Laming, "Fibre non-uniformity caused Bragg gratings imperfections," in *OFC*, p. Paper FA1, 1999.

[143] M. Ibsen, M. Durkin, M. J. Cole, and R. I. Laming, "Sinc-sampled fibre bragg gratings for identical multiple wavelength operations," *IEEE Photonics Technology Letters*, vol. 10, pp. 842–844, 1998.

[144] A. Canagasabey, C. Corbari, M. R. Mokhtar, P. G. Kazansky, and M. Ibsen, "Tuneable second-harmonic generation in periodically poled optical fibres," in *OFC/NFOEFC*, p. Paper OThQ2, 2005.

[145] G. Martinelli, Y. Quiquempois, A. Kudlinski, and H. Zeghlache, "Method to improve thermal poling efficiency in silica glasses," *Electronics Letters*, vol. 38, pp. 570–571, 2002.

[146] A. C. Liu, M. J. F. Digonnet, and G. S. Kino, "Measurment of the dc Kerr and electrostrictive phase modulation in silica," *J. Opt. Soc. Am. B*, vol. 18, no. 2, pp. 187–194, 2001.

[147] P. D. Maker, R. W. Terhune, M. Nisenoff, and C. M. Savage, "Effects of dispersion and focusing on the production of optical harmonics," *Physical Review Letters*, vol. 8, no. 1, pp. 21–22, 1962.

[148] N. Bloenbergen and P. S. Pershan, "Light waves at the boundary of nonlinear media," *Physical Review*, vol. 128, no. 2, pp. 606–622, 1962.

[149] J. Jerphagnon and S. K. Kurtz, "Maker fringes: a detailed comparison of theory and experiment for isotropic and uniaxial crystals," *Journal of Applied Physics*, vol. 41, no. 4, pp. 1667–1681, 1969.

[150] E. Hecht, *Optics*. Addison-Wesley Longman Inc., 3rd edition ed., 1998.

[151] L. J. Henry, A. D. DeVibiss, and T. E. Tsai, "Effects of preannealing on the level of second-harmonic generation and defects sites achieved in poled low-water fused silica," *J. Opt. Soc. Am. B*, vol. 12, no. 11, pp. 2037–2045, 1995.

[152] A. Kameyama, E. Muroi, A. Yokotani, K. Kurosawa, and P. Hernan, "X-ray radiation effects on second-harmonic generation in thermally poled silica glasses," *J. Opt. Soc. Am. B*, vol. 14, no. 5, pp. 1088–1092, 1997.

[153] A. Narazaki, K. Tanaka, and K. Hirao, "Surface structure and second-order nonlinear optical properties of thermally poled WO_3-TeO_2 glasses doped with Na^+," *J. Opt. Soc. Am. B*, vol. 19, no. 1, pp. 54–62, 2002.

[154] A. Narazaki, K. Tanaka, K. Hirao, and N. Soga, "Induction and relaxation of optical second-order nonlinearity in tellurite glasses," *Journal of Applied Physics*, vol. 85, no. 4, pp. 2046–2051, 1999.

[155] H. Hayashi, H. Nakayama, O. Sugihara, and N. Okamoto, "Thermally stable and large second-order nonlinearity in poled silica films doped with disperse Red 1 in high concentration," *Optics Letters*, vol. 20, no. 22, pp. 2264–2266, 1995.

[156] S. Matsumotu, T. Fujiwara, and A. J. Ikushima, "Large second-order nonlinearity in Ge-doped silica glass," *Optical Materials*, vol. 18, pp. 19–22, 2001.

[157] A. Okada, K. Ishii, K. Mito, and K. Sasaki, "Second-order optical nonlinear properties in corona-poled glass films," *Journal of Applied Physics*, vol. 74, no. 1, pp. 531–535, 1993.

[158] J. Khaled, T. Fujiwara, M. Ohama, and A. J. Ikushima, "Generation of second harmonic in Ge-doped SiO_2 thin fils by ultraviolet irradiation under poling electric field," *Journal of Applied Physics*, vol. 87, no. 5, pp. 2137–2141, 2000.

[159] K. Tanaka, K. Kashima, K. Hirao, N. Soga, A. Mito, and H. Nasu, "Second harmonic generation in electrically poled Li_2O-Nb_2O_5-TeO_2 glasses," *Journal of Non-Crystalline Solids*, vol. 185, pp. 123–126, 1995.

[160] H. Imai, S. Horinouchi, Y. Uchida, H. Yamasaki, K. Fukao, G. Zhang, T. Kinoshita, K. Mito, H. Hirashima, and K. Sasaki, "Time-dependent decay of quadratic nonlinearity in corona poled silicate glass films," *Journal of Non-Crystalline Solids*, vol. 196, pp. 63–66, 1996.

[161] Q. Liu, F. Gan, X. Zhao, K. Tanaka, A. Narazaki, and K. Hirao, "Second-harmonic generation in $Ge_{20}As_{25}S_{55}$ glass irradiated by an electron beam," *Optics Letters*, vol. 26, no. 17, pp. 1347–1349, 2001.

[162] E. Lopez-Lago, V. Couderc, L. Griscom, F. Smektala, and A. Barthélémy, "All optical poling of a chalcohalogenide glass," *Optical Materials*, vol. 16, pp. 413–416, 2001.

[163] J. G. M. A. Dragomir and D. N. Nikogosyan, "Femtosecond measurements of two-photon absorption coefficients at $\lambda = 264\,\text{nm}$ in glasses, crystals, and liquids," *Applied Optics*, vol. 41, no. 21, p. 4365, 2002.

[164] A. Dragomir, J. G. McInerney, D. N. Nikogosyan, and P. G. Kazansky, "Two-photon absorption properties of commercial fused silica and germanosilicate glass at 264 nm," *Applied Physics Letters*, vol. 80, p. 1114, 2002.

[165] Heraeus Quarzglas GmbH, "Quartz glass for optics, data and properties." datasheet, 1994.

[166] V. N. Bagratashvili, S. I. Tsypina, P. V. Chernov, A. O. Rybaltovskii, Y. S. Zavorotny, S. S. Alimpiev, Y. O. Simanovskii, L. Dong, and J. P. S. Russell *Applied Physics Letters*, vol. 68, p. 1616, 1996.

[167] N. M. Lawandy and R. L. MacDonald *J. Opt. Soc. Am. B*, vol. 8, p. 1307, 1991.

[168] M. Jacobsohn and U. Banin, "Size dependence of second harmonic generation in CdSe nanocrystal quantum dots," *Physical Chemistry B*, vol. 104, no. 1, pp. 1–5, 2000.

[169] J. Sasai, K. Tanaka, and K. Hirao, "Preparation and second-order nonlinear properties of CuCl nanocrystal-doped glass films," *Scripta Materialia*, vol. 44, pp. 1225–1228, 2001.

[170] H. Chen, H. Xia, C. Zhu, and F. Gan, "Second harmonic generation from electrically polarized CuCl-microcrystallite-doped glass," *Materials Letters*, vol. 50, pp. 333–336, 2001.

[171] J. Sasai, K. Tanaka, and K. Hirao, "Structure and second-order nonlinear optical properties of CuCl nanocrystal-doped thin films prepared by rf sputtering," vol. 193, p. 4280, 2001.

[172] W. Wang, J. Xu, X. Liu, Y. Jiang, G. Wang, and X. Lu, "Second harmonic investigation of indium tin oxide thin films," *Thin Solid Films*, vol. 365, pp. 116–118, 2000.

[173] F. Ghebremichael, C. Poga, and M. G. Kuzyk, "Optical second harmonic characterization of spontaneous symmetry-breaking at polymer/transparent conductor interfaces," *Applied Physics Letters*, vol. 66, no. 2, pp. 139–141, 1995.

[174] H. Nasu, H. Okamoto, K. Kurachi, J. Matsuoka, K. Kamiya, A. Mito, and H. Hosono, "Second-harmonic generation from electrically poled SiO_2 glasses: effect of OH concentration, defects, and poling conditions," *Journal of the Optical Society of America B*, vol. 12, no. 4, pp. 644–649, 1995.

[175] N. Chiodini, F. Meinardi, F. Morazzoni, J. Padovani, A. Paleari, R. Scotti, and G. Spinolo, "Thermally induced segregation of SnO_2 nanoclusters in Sn-doped silica glasses from oversaturated Sn-doped silica xerogels," *Journal of Material Chemestry*, vol. 11, no. 3, p. 926, 2001.

[176] K. Tanaka, K. Kashima, K. Hirao, N. Soga, S. Yamagata, A. Mito, and H. Nasu, "Effect of gamma-irradiation on optical second harmonic intensity of electrically poled silica glass," *Japanese Journal of Apllied Physics*, vol. 34, pp. 173–174, 1995.

[177] O. Deparis, D. L. Griscom, P. M. andM. Decréton, and M. Blondel, " Influence of the cladding thickness on the evolution of the NBOHC band in optical fibers exposed to gamma radiations," *Journal of non-Crystalline Solids*, vol. 216, p. 124, 1997.

[178] N. P. Bansal and R. H. Doremus, *Handbook of Glass Properties.* Orlando, Florida, 32887: Academic Press Inc., 1986.

[179] W. Margulis and F. Laurell *Optics Letters*, vol. 21, p. 1786, 1996.

[180] O. Sugihara, M. Nakanishi, H. Fujimura, C. Egami, and N. Okamoto *J. Opt. Soc. Am. B*, vol. 15, p. 421, 1998.

[181] O. L. Anderson and D. A. Stuart *Journal of the American Ceramic Society*, vol. 37, p. 573, 1954.

[182] C. H. Hsieh and H. Jain, "Influence of network-forming cations on ionic conduction in sodium silicate glasses," *Journal of Non-Crystalline Solids*, vol. 183, p. 1, 1995.

[183] H. W. K. Tom, R. H. Stolen, G. D. Aumiller, and W. Pleibel, "Preparation of long-coherence-length second-harmonic-generating optical fibers by using mode-locked pulses," vol. 13, p. 512, 1988.

[184] L. J. Henry, "Correlation of Ge E' defects sites with second-harmonic generation in poled high-water fused silica," *Optics Letters*, vol. 20, no. 15, pp. 1592–1594, 1995.

[185] D. Faccio, A. Busacca, D. W. J. Harwood, G. Bonfrate, V. Pruneri, and P. G. Kazansky, "Effect of core-cladding interface on thermal poling of germano-silicate optical waveguides," *Optics Communications*, vol. 196, pp. 187–190, 2001.

[186] G. Bonfrate, "Optical parametric processes in periodically poled silica fibres," PhD thesis, Optoelectronics Research Centre, University of Southampton, July 2000.

[187] M. J. Weber, *Handbook of lasers*. Laser and optical science and technology series, CRC press LLC, 2001.

[188] H. M. Pask, R. J. Carman, D. C. Hanna, A. C. Tropper, C. J. Mackechnie, P. R. Barber, and J. M. Dawes, "Ytterbium-doped silica fiber lasers: versatile sources for the 1-1.2 μm region," *IEEE Journal of Selected Topics in Quantum Electronics*, vol. 1, no. 1, pp. 2–13, 1995.

[189] W. L. Barnes, S. B. Poole, J. E. Townsend, L. Reekie, D. J. Taylor, and D. N. Payne, "Er^{3+}-Yb^{3+} and Er^{3+} doped fiber lasers," *Journal of Lightwave Technology*, vol. 7, no. 10, pp. 1461–1465, 1989.

[190] C. H. Bennett and G. Brassard, "Quantum Cryptography: public key distribution and coin tossing," in *Proceeding of IEEE International Conference on Computers, Systems and Signal Processing*, (Bangalore, India), pp. 175–179, IEEE, 1984.

[191] S. Castelletto, I. P. Degiovanni, A. Migdall, and M. Ware, "On the measurement of two-photon single-mode," *New Journal of Physics*, vol. 6, p. 87, 2004.

[192] F. A. Bovino, P. V., A. Colla, G. Castagnoli, G. D. Giuseppe, and A. V. Sergienko, "Effective fiber-coupling of entangled photons for quantum communication," *Optical Communications*, vol. 227, pp. 343–348, 2003.

[193] M. A. Albota and E. Dauler, "Single photon detection of degenerate photon pairs at 1.55 μm from a periodically poled lithium niobate parametric downconverter," *Journal of Modern Optics*, vol. 51, no. 9-10, pp. 1417–1432, 2004.

[194] P. Trojek, C. Schmid, M. Bourennane, and H. Weinfurter, "Compact source of polarization-entangled photon pairs," *Optics Express*, vol. 12, no. 2, p. 276, 2004.